Ground electromagnetic experiments to investigate the possibility of using an airborne electromagnetic system to detect nuclear magnetic resonance associated with unbound water in the subsurface

By

Nikolas Gazo

A thesis submitted in partial fulfillment
of the requirements for the degree of
Master of Science (MSc) in Geology

The Faculty of Graduate Studies
Laurentian University
Sudbury, Ontario, Canada

THESIS DEFENCE COMMITTEE/COMITÉ DE SOUTENANCE DE THÈSE
Laurentian Université/Université Laurentienne
Faculty of Graduate Studies/Faculté des études supérieures

Title of Thesis Titre de la thèse	Ground electromagnetic experiments to investigate the possibility of using an airborne electromagnetic system to detect nuclear magnetic resonance associated with unbound water in the subsurface
Name of Candidate Nom du candidat	Gazo, Nikolas
Degree Diplôme	Master of Science
Department/Program Département/Programme	Geology
Date of Defence Date de la soutenance	May 31, 2017

APPROVED/APPROUVÉ

Thesis Examiners/Examinateurs de thèse:

Dr. Richard Smith
(Supervisor/Directeur(trice) de thèse)

Mr. Ben Polzer
(Committee member/Membre du comité)

Dr. Michael Schindler
(Committee member/Membre du comité)

Dr. Kristina Keating
(External Examiner/Examinateur externe)

Approved for the Faculty of Graduate Studies
Approuvé pour la Faculté des études supérieures
Dr. David Lesbarrères
Monsieur David Lesbarrères
Dean, Faculty of Graduate Studies
Doyen, Faculté des études supérieures

ACCESSIBILITY CLAUSE AND PERMISSION TO USE

I, **Nikolas Gazo**, hereby grant to Laurentian University and/or its agents the non-exclusive license to archive and make accessible my thesis, dissertation, or project report in whole or in part in all forms of media, now or for the duration of my copyright ownership. I retain all other ownership rights to the copyright of the thesis, dissertation or project report. I also reserve the right to use in future works (such as articles or books) all or part of this thesis, dissertation, or project report. I further agree that permission for copying of this thesis in any manner, in whole or in part, for scholarly purposes may be granted by the professor or professors who supervised my thesis work or, in their absence, by the Head of the Department in which my thesis work was done. It is understood that any copying or publication or use of this thesis or parts thereof for financial gain shall not be allowed without my written permission. It is also understood that this copy is being made available in this form by the authority of the copyright owner solely for the purpose of private study and research and may not be copied or reproduced except as permitted by the copyright laws without written authority from the copyright owner.

Abstract

Ground-based geophysical experiments were undertaken to test the possibility of detecting groundwater using nuclear magnetic resonance from an airborne electromagnetic prospecting system. Two experimental surveys were conducted: One over an ice-covered lake, containing a large volume of freshwater, and the other over an equal volume of land, with little to no freshwater in the subsurface. If exposed to a radio-frequency pulse at the Larmor frequency, protons in water molecules create a magnetic field oscillating at the Larmor frequency. Both surveys used a 120-second long frequency sweep from 2300 to 2400 Hz. It was initially hypothesized that as the frequency passed over the Larmor frequency, 2348 Hz, there would be phase shift between the transmitter and receiver signals. Phase measurements, using the heterodyne method, between the lake and land data proved to be inconclusive, although the lake data showed an oscillatory decay in the off-time, not equal to the Larmor frequency.

Keywords:

Geophysics, nuclear magnetic resonance, frequency sweep, freshwater exploration

Acknowledgements

Firstly, I would like to express my gratitude for my supervisor, Dr. Richard Smith. He provided me with a unique project that incorporated two of my main interests, electromagnetics and water exploration. He was extremely knowledgeable on many topics pertinent to my project and was always quick and caring when answering my questions. The environment he created for me and my fellow geophysicists-in-training was exceptional and I am happy I was able to be a part of it.

Secondly, I would like to thank Ben Polzer for giving me the opportunity to use the necessary equipment to conduct my field surveys. He also gave very insightful comments when I was designing my surveys. The advice and guidance he provided towards my project was invaluable. I would also like to thank Matt Charron for working with me in the field when conducting my surveys.

Thirdly, I am grateful my other committee member and external examiner, Dr. Michael Schindler and Dr. Kristina Keating for various comments and input during my defence. I would like to thank my office-mates, Yongxing Li, Omid Mahmoodi, Frédéric Gaucher, Francisca Maepa, and Jacqueline Huggins for their support and positive attitude towards geophysics and myself. In particular, I would like to thank Frédéric for many geophysics-related discussions and for accompanying me on car rides to the PDAC and KEGS events in Toronto. I was able to see geophysics from a different perspective, which I am grateful for.

Lastly, I would like to acknowledge the Natural Sciences and Engineering Research Council of Canada (NSERC) for funding of this project.

Table of Contents

List of Figures

List of Tables

Chapter 1

1 Introduction and Background

The need for fresh groundwater is intensifying with climate change and increasing global population. An important necessity for human beings is water, whether it be for drinking, hygiene, or agriculture. Some countries, like Canada, have an abundance of freshwater due to the vast number of lakes. However, many countries, specifically ones residing in geographically arid regions, are less fortunate and are in need of efficient inexpensive ways to locate freshwater reserves (WWAP, 2015)

The most viable source of freshwater exists as groundwater located within aquifers, which are bodies of permeable rock that contain or transmit groundwater (Freeze and Cherry, 1979). The difficulty with locating aquifers is that they are not visible from the surface; thus, requiring a non-invasive method to image the subsurface. A popular way to search for aquifers is using geophysical techniques (Kirsch, 2006), with the most economic approach for large scale surveys being airborne electromagnetics (AEM).

Electromagnetic (EM) systems exploit the phenomenon of electromagnetic induction (West and Macnae, 1991) and are governed by Maxwell's equations (Griffiths, 2013). Although AEM systems are able to cover large areas (up to hundreds of square kilometres (Palacky and West, 1991)), they are not able to measure groundwater directly, but allow geophysicists to infer regions of groundwater based on contrasting conductive zones. In some cases, fresh water is more resistive than its surroundings, and in other cases it can be more conductive than its surroundings; thus, interpreting AEM data requires having knowledge of the conductivities of the layers that are important in the local hydrogeology (e.g., Smith

et al., 2004).

In the last few decades, a new non-invasive ground-based geophysical technique known as magnetic resonance sounding (MRS) has emerged, first introduced by Varian (1962). The MRS technique is based on the theory of nuclear magnetic resonance, which exploits specific properties of subatomic particles and their interactions with electromagnetic fields (Abragam, 1983; Keeler, 2005; Slichter, 1990; Becker, 2000; Levitt, 2008; Farrar and Becker, 1971). MRS is unique due to its ability to directly measure a signal from the hydrogen protons in water molecules. The signal received in MRS surveys is from the relaxation of the protons. Typically, this relaxation is oscillating at a characteristic frequency and has an amplitude that decays with time (Yaramanci, 2000). Subtle variations in the amplitude and the decay rate allow geophysicists to give an accurate representation of the subsurface water content.

The amplitude at the beginning of the decay is proportional to the presence and amount of groundwater in the subsurface (Goldman and Neubauer, 1994). To resolve the amount of groundwater at greater depths, the energising field needed to excite the protons is increased (Kirsch, 2006). With respect to groundwater exploration, the decay of the NMR signal from water can produce information related to the pore size, permeability, hydraulic conductivity, and magnetic susceptibility of the subsurface (Legchenko et al., 2002; Hertrich, 2008; Grunewald and Knight, 2011).

The MRS technique is unique because it has the ability to directly influence the protons in the water molecules and receive a response from them. A limitation in a standard MRS survey is the low production rates (Behroozmand et al., 2014); a single site, which can take several hours to acquire, can only provide one-dimensional water content information for an area proximal to the loop used. If a large area is to be covered, many days will be required.

A possible solution to the areal coverage problem would be to undertake MRS measurements from an airborne platform. The advantage of an airborne system would be the large area covered in a day long survey, but the trade-off would be loss of ability to interpret the hydraulic parameters such as depth, porosity, permeability, etc. However, the airborne survey may give information on the quantity of water in certain regions, allowing for a more focused ground survey. A recent study has shown the ability to record NMR measurements 4 metres above the ground using a torus-shaped helium-filled balloon towed between two vehicles (Costabel et al., 2016). The set-up is not the same as an AEM system nor does it move as fast, but it is able to survey a larger area than a traditional MRS survey. This helium balloon system compromised vertical resolution for survey speed increases. An airborne system would likely compromise an ability to determine parameters such as the decay rate in order to gain further increases in survey speed.

The first step towards developing an airborne MRS system (comparable to an AEM system) would be to determine whether an NMR signal from freshwater can be located with a traditional ground-based electromagnetic prospecting system. If successful, the hope would be to then scale up the ground survey design to an aircraft. The following thesis will begin to assess this question by first examining the results from a ground survey.

Chapter 2

2 Theory

2.1 Spin

All matter in the known universe is composed of a combination of fundamental particles: protons, neutrons, and electrons. Each of these subatomic particles have inherent characteristics attributed to them, which are mass, charge, and spin (Levitt, 2008) shown in Table 1. The first two characteristics are commonly well understood in the macroscopic world, whereas the final characteristic, *spin*, is entirely quantum mechanical in nature and is the basis for nuclear magnetic resonance (NMR) and electron spin resonance (ESR).

Table 1: The intrinsic physical properties of subatomic particles (Harris, 2008).

Particle	Spin (**I**)	Mass (kg)	Charge (Coulombs)
Neutron	1/2	1.6749273×10^{-27}	0
Proton	1/2	1.6726217×10^{-27}	1.60217662×10^{-19}
Electron	1/2	9.1093822×10^{-31}	$-1.60217662\times10^{-19}$

Spin is an intrinsic form of angular momentum meaning it is *inherent* to the particle and not *created* from rotational motion (Griffiths, 2005). By possessing spin, particles react to magnetic fields, which led to its discovery.

Experimentally, spin was first discovered in the 1920's by Gerlach and Stern (1922). In the experiment, silver atoms were accelerated through a non-uniform magnetic field and onto a detector screen. The experiment showed discrete regions of atom accumulation on the detector screen. The results were profound in that it showed that particles with spin acted as magnetic dipoles in a magnetic field and that the values of spin were quantized (i.e.,

taking only discrete values). The quantization was realized due to the well-defined discrete regions on the detector screen. If the detector screen had shown a continuous distribution, then spin would take on a continuity of values.

The Stern-Gerlach experiment displayed the spin property of particles by utilizing silver atoms, which are a combination of many subatomic particles. Each subatomic particle possesses spin, but for a molecule, atom, or a nucleus, a set of rules have been formulated that govern whether or not it will possess a *net* spin. Specifically, the spin rules for a nucleus are (Levitt, 2008):

#1. If the number of neutrons **and** the number of protons are both even, then the nucleus has no net spin,

#2. If the number of neutrons **plus** the number of protons is odd, then the nucleus has a half-integer spin (e.g., 1/2, 3/2, 5/2),

#3. If the number of neutrons **and** the number of protons are both odd, then the nucleus has integer spin (e.g., 1,2,3).

The Stern-Gerlach experiment used either ^{107}Ag or ^{109}Ag, which both result in a nucleus net spin of 1/2 since they both satisfy nucleus spin rule #2. The silver atoms used had a neutral charge (47 protons and 47 electrons), giving rise to one unpaired electron. Although both the electron and nucleus each had a net spin of $\mathbf{I}$=1/2, it was the electron magnetic dipole moment that was most influential in the experiment due to the fact that the electron dipole moment strength is greater than the nucleus dipole moment strength (Slichter, 1990).

The difference in magnetic dipole moment strengths between nuclei and electrons is the key distinction between NMR and ESR, which will be covered shortly. To prove that the Stern-Gerlach experiment was not just showing peculiar properties of silver atoms, an experiment was later conducted in 1927 by Phipps and Taylor (1927), using a hydrogen atom

in its ground state (utilizing the electron spin). Receiving the same results (i.e., discrete populations on the detector screen), they concluded that atoms with non-zero spin do in fact act as magnetic dipoles in the presence of a magnetic field.

2.2 Spin in a magnetic field

For a particle possessing spin, there are many consequences. The first being that spin is a form of angular momentum and should be treated as such. The second being that a particle with spin acts as a magnetic dipole in the presence of a magnetic field and lastly that spin is quantized.

Firstly, a particle (or molecule) that has a net non-zero spin ($\mathbf{I}$) will have a spin angular momentum given by,

$$\mathbf{S} = \hbar\mathbf{I}, \tag{1}$$

with units of $\hbar = h/2\pi$, where h is Plank's constant (Feynman et al., 1963). Since $\mathbf{I}$ is quantized and only takes on discrete values (as shown in the Stern-Gerlach experiment), Equation 1 will also take on discrete values.

The relationship between the spin angular momentum of a particle and its magnetic moment is given as,

$$\boldsymbol{\mu} = \gamma\mathbf{S}, \tag{2}$$

where γ is known as the gyromagnetic ratio (Hz/T) and is specific to each particle or nucleus (Griffiths, 2005). The gyromagnetic ratios for the proton and the electron are $\gamma_p = 2.675222005 \times 10^8$ Hz/T and $\gamma_e = 1.760859644 \times 10^{11}$ Hz/T, respectively. The ratio between the two gyromagnetic ratios (γ_e/γ_p) is approximately 658, which results in the electron magnetic dipole moment being 658 times greater than the proton magnetic dipole

moment (from Equation 2). The large difference in magnitudes of the magnetic dipoles is one of the key distinctions between NMR and ESR. The other main distinction is related to the energy required to go from the ground state to an (or the) excited state, which will be addressed below. A detailed mathematical treatment outlining the steps needed to go from Equation 1 to Equation 2 is shown in Griffiths (2005).

The significance of the quantization of spin angular momentum arises when a magnetic field ($\mathbf{B}$) is applied to a particle with spin. In a magnetic field, a particle with spin, $\mathbf{I}$, will occupy one of $2(\mathbf{I}+1)$ possible energy states. Following quantum mechanics, the Hamiltonian operator is used to solve the particles wave-function, giving rise to the magnetic quantum number, m (Griffiths, 2005). The magnetic quantum number will take on the values of $m = -I, -I+1, -I+2, ..., I-1, I$. In the case of $\mathbf{I}$=1/2, the magnetic quantum number will have the values, $m = -1/2$ and $1/2$. Inserting the magnetic quantum number into Equations 1 and 2, the magnetic dipole moment becomes,

$$\boldsymbol{\mu} = \gamma \hbar m_z, \tag{3}$$

where the z subscript represents quantization of $\boldsymbol{\mu}$ along a magnetic field, $\mathbf{B} = B_o \hat{z}$.

Generally, when a magnetic dipole ($\boldsymbol{\mu}$) is placed in a magnetic field ($\mathbf{B}$), it will experience a torque (Feynman et al., 1963),

$$\boldsymbol{\tau} = \boldsymbol{\mu} \times \mathbf{B}, \tag{4}$$

which causes a precession about $\mathbf{B}$. The precession of the dipole is due to its intrinsic spin angular momentum and the relation, $\boldsymbol{\tau} = d\mathbf{S}/dt$, which states that a torque is equal to the rate of change of the angular momentum (Taylor, 2005). The magnetic dipole will also have a magnetic potential energy (Feynman et al., 1963),

$$U_{\text{mag}} = -\boldsymbol{\mu} \cdot \mathbf{B}, \tag{5}$$

where the minus sign denotes that the lowest energy state is when the magnetic dipole is parallel with the applied field. In the case of a particle with spin, the magnetic dipole moment is quantized (Equation 3) and will only take on discrete values when in a magnetic field. In the case of spin-1/2, the particle will be in either two states, aligned with (parallel) or against (anti-parallel) the magnetic field. The magnetic energy of a spin-1/2 magnetic dipole is,

$$\begin{aligned} U_{\text{mag}} &= -\mu B, \\ &= -\gamma \hbar m_z B_o, \qquad m_z = -1/2 \text{ and } 1/2. \end{aligned} \tag{6}$$

A depiction of the energy levels that a spin-1/2 particle occupies before and after a magnetic field is applied is displayed in Figure 1. When there is no field applied, the magnetic dipoles all have the same magnetic potential energy, hence the "degenerate" in Figure 1. Once the magnetic field is applied, the magnetic dipole will be in one of two possible energy states ($m_z = -1/2$ or $m_z = 1/2$). The energy difference between the two states is denoted by $\mathbf{\Delta E}$ in Figure 1.

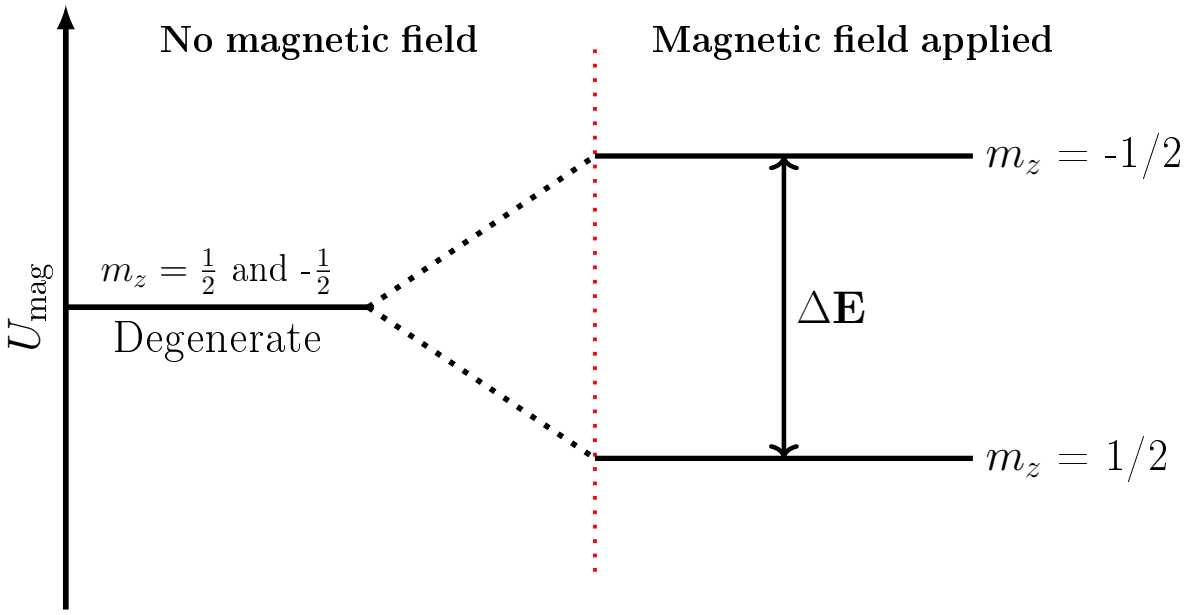

Figure 1: The two possible energy levels for a spin-1/2 system. When no magnetic field is present, the magnetic dipoles are degenerate and possess the same magnetic energy. Once a magnetic field is applied, the magnetic dipole will be in one of the two possible energy states. The energy gap between the two possible states is given as $\Delta\mathbf{E}$.

The energy gap between possible states is a crucial part to both NMR and ESR. The main idea behind both phenomena is the ability to excite the dipole with the appropriate energy to cause a transition from a lower level to a higher level and then analyzing the relaxation back to the lower level.

The transition from the lower level (ground state) to a higher energy level (excited state) can be obtained by irradiating the dipole with an oscillating magnetic field. Typically, the transition is caused by a photon of the of correct frequency. The frequency needed can be solved for by setting the energy of a photon (Feynman et al., 1963) to the energy gap in Figure 1. The energy gap is equal to,

$$\begin{aligned} \Delta E &= -\gamma\hbar B_o m_{1/2} + \gamma\hbar B_o m_{-1/2}, \\ &= -\gamma\hbar B_o. \end{aligned} \tag{7}$$

Setting the energy gap to the energy of a photon,

$$\begin{aligned} \Delta E &= E_{\text{photon}}, \\ -\gamma\hbar B_o &= \hbar\omega, \end{aligned} \tag{8}$$

and then rearranging to find the needed frequency,

$$f = -\frac{\gamma}{2\pi} B_o. \tag{9}$$

The sign of the frequency is not important in this context, since it represents the amount of cycles per second, we can use,

$$f = \frac{\gamma}{2\pi} |B_o|, \tag{10}$$

which is known as the Larmor frequency (Levitt, 2008; Keeler, 2005; Becker, 2000). Since each molecule, particle, or nucleus has its own unique gyromagnetic ratio, it will then have its own unique Larmor frequency. The result of Equation 10 is quite profound; it allows us to easily solve for the required excitation frequency with knowing only the magnetic field strength.

The process of causing a transition from one energy state to another is known, but the likelihood of which energy state is favoured depends on Boltzmann statistics (Feynman et al., 1963; Levitt, 2008; Slichter, 1990). For a particle with spin-1/2, it will occupy one of two possible energy states, parallel to the field or anti-parallel to the field, which we will call spin-up and spin-down states, respectively. The probability that a particle is in a specific state is proportional to the energy of the state,

$$\begin{aligned} P(\text{state}) &\propto e^{(-\text{Energy of state}/kT)}, \\ &= e^{(-U_{mag}/kT)}, \end{aligned} \tag{11}$$

where k is the Boltzmann constant and T is the temperature of the system. For a spin-1/2 particle, the spin-up state is slightly favoured. In a macroscopic sample containing N ($>10^{28}$) spin-1/2 molecules, the distribution of spins between the two possible states will be proportional to the ratio, P_1/P_2. The total number of molecules, N, is composed of up-spins N_{up} and down-spins N_{down}. Using Equations 6 and 11, the number of spins per unit volume with spin-up is,

$$N_{up} = Ae^{(-\mu B/kT)}, \tag{12}$$

and the number with spin-down is,

$$N_{down} = Ae^{(+\mu B/kT)}. \tag{13}$$

The constant A is fixed and can be determined using,

$$N = N_{up} + N_{down}, \tag{14}$$

where N is the total number of spins per volume. The constant is easily solved,

$$A = \frac{N}{e^{+\mu B/kT} + e^{-\mu B/kT}}. \tag{15}$$

When it comes to experimentally measuring NMR or ESR, the *average* magnetic moment ($\langle\mu\rangle$) of a sample is needed to assist in explaining the dynamics of the phenomenon. The average magnetic moment is computed for an ensemble of spins by adding dipole contributions from spin-up (-μ) and the contributions from spin-down (μ) and then dividing by the

total number of spins in the sample (Feynman et al., 1963),

$$\begin{aligned}\langle\mu\rangle &= \frac{(-\mu)N_{up} + (\mu)N_{down}}{N}, \\ &= \mu\left[\frac{N_{up} - N_{down}}{N}\right], \\ &= \mu\left[\frac{e^{(\mu B/kT)} - e^{(-\mu B/kT)}}{e^{(\mu B/kT)} + e^{(-\mu B/kT)}}\right], \\ &= \mu\tanh(\mu B/kT).\end{aligned} \tag{16}$$

2.3 Magnetization vector

In NMR and ESR, the *average* magnetic moment (Equation 16) of an sample is then used to solve for the magnetic moment per unit volume, which is known as the *magnetization* vector ($\boldsymbol{M}$). The magnetization vector is then used to help illustrate the dynamics of a sample with a net non-zero spin under the influence of a magnetic field. The magnetization vector is,

$$\begin{aligned}\boldsymbol{M} &= N\langle\mu\rangle_{avg}, \\ &= N\mu\tanh(\mu B/kT).\end{aligned} \tag{17}$$

For normal (Earth-like) temperatures, we can replace $\tanh(x)$ with x, which results in,

$$\boldsymbol{M} = \frac{N\mu^2 B}{kT}. \tag{18}$$

The magnetization vector represents an *ensemble* of spins. The units for the magnetization vector are A/m, so in order to have the units of a magnetic dipole, we must multiply Equation 18 by a volume to get units of A·m^2.

The following points summarize the previous information, which allow us to then understand nuclear magnetic resonance.

- Begin with a volume of molecules that have spin-1/2. In the absence of a magnetic field, all molecules are degenerate (Figure 2).

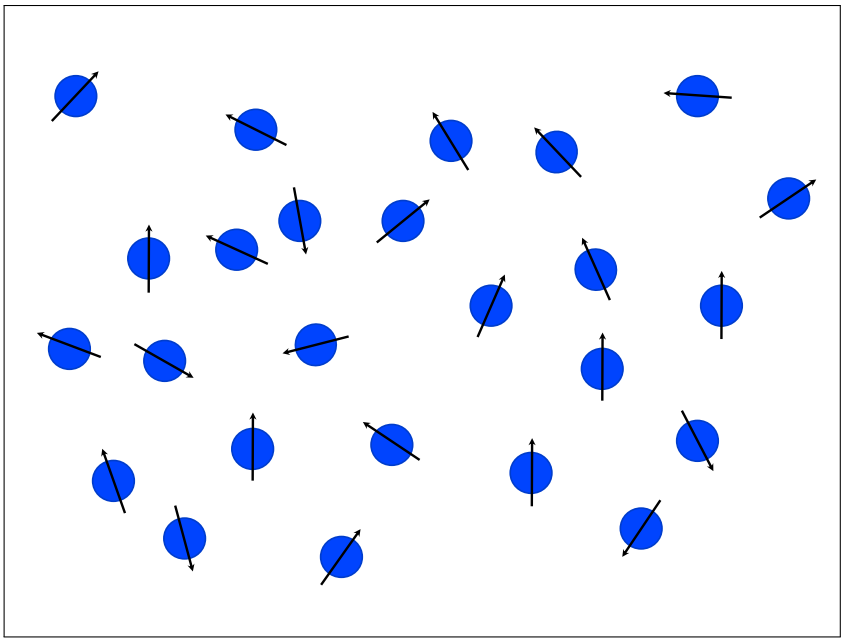

Figure 2: An ensemble of spins in the absence of a magnetic field. Each spin has the same magnetic energy (i.e., degenerate).

- Once a magnetic field is applied to the sample, the spins will be influenced since they are acting as magnetic dipoles (Equation 2). The molecules will experience a torque from the magnetic field (Equation 4) which will cause them to precess around the magnetic field lines at the Larmor frequency. The spins will be in one of two possible energy states (Figure 3).

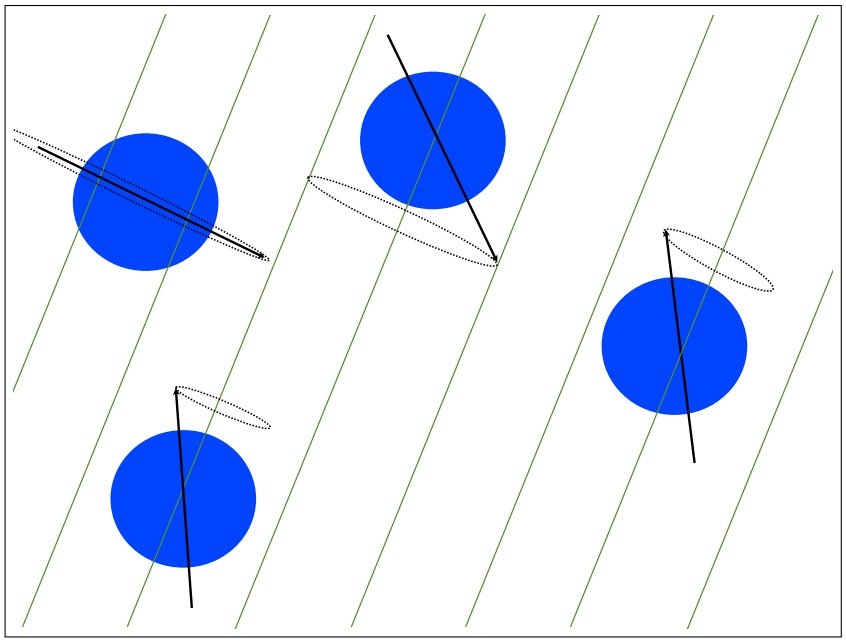

Figure 3: Once a magnetic field is applied, the spins will experience a torque which causes them to precess about the magnetic field lines at the Larmor frequency. The spins will be in one of two possible energy states and are no longer degenerate.

- Due to Boltzmann statistics (Equation 11), there will be more spins aligned with the field, which results in a net magnetic moment along the field (Equation 16). Multiplying the number of spins (N) by the average magnetic moment allows us the calculate the magnetization vector (Figure 4).

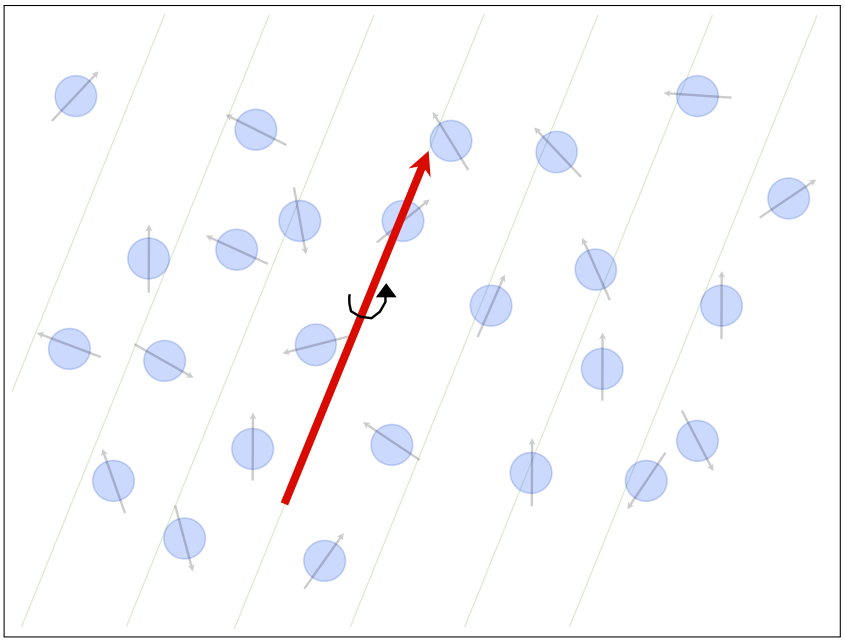

Figure 4: On average, the spins will have a greater population aligned with the field. A vector sum of these spins creates a magnetization vector, which is representative of the whole sample.

2.4 Nuclear magnetic resonance

Nuclear magnetic resonance is possible for molecules, atoms, or nuclei that have a zero net spin for their electrons and a non-zero net spin of the nucleus. The non-zero spin of the nucleus allows the nucleus to act as a magnetic dipole, $\boldsymbol{\mu}$ (Equation 3), occupying one of the 2(I+1) possible energy levels. The resonance condition is met when the magnetic dipole is supplied with an energy quanta at the Larmor frequency (Equation 10) which causes an energy state transition. The nucleus then returns to equilibrium by losing energy to thermal movements and to spin-spin interactions with other nuclei of the system (Levitt, 2008). The relaxation of the nuclei are the object of observation in NMR spectrometry. The excitation and relaxation mechanisms of NMR can be modeled using classical mechanics and the magnetization vector.

2.4.1 The Bloch equations

The Bloch equations, developed by Bloch (1946) while at Stanford University, are a set of differential equations that describe the orientation of the magnetization vector (Equation 18) as a function of time, when in the presence of interacting time-dependent magnetic fields (ambient and applied). The equations do not describe the motion of each individual spin magnetic moment, but of an ensemble of magnetic moments. Bloch began the description of the magnetization vector dynamics with the classical equation of motion of a magnetic moment in a magnetic field (Becker, 2000),

$$\boldsymbol{\tau} = \boldsymbol{\mu} \times \boldsymbol{B}.$$

It is well known in Newtonian physics that a torque will cause a change in angular momentum with respect to time (Griffiths, 2013). Since the magnetic moment possesses spin, it will also have an intrinsic angular momentum ($\boldsymbol{S}$), which allows us to relate the intrinsic angular momentum to the torque exerted on it in the magnetic field,

$$\frac{d\boldsymbol{S}}{dt} = \boldsymbol{\mu} \times \boldsymbol{B}. \tag{19}$$

After multiplying Equation 19 by γ, Equation 2 can then be used to find the rate of change of the magnetic moment,

$$\frac{d\boldsymbol{\mu}}{dt} = \gamma \boldsymbol{\mu} \times \boldsymbol{B}. \tag{20}$$

The summation of all magnetic moments in a sample is the magnetization, so,

$$\frac{d\boldsymbol{M}}{dt} = \gamma \boldsymbol{M} \times \boldsymbol{B}. \tag{21}$$

Equation 21 represents a set of coupled differential equations that describe the motion of how an ensemble of spins reacts to interacting magnetic fields.

Depending on the experiment, the solution is determined using different techniques in

order to accommodate for various system conditions. A solution that incorporates two experimental techniques, known as pulse-methods and adiabatic passage (Levitt, 2008), will be shown below. A description of the two techniques will be explained in the next chapter.

The magnetization vector and the interacting magnetic fields are all 3-dimensional vectors, meaning they can be represented in component form,

$$\boldsymbol{M} = (M_x, M_y, M_z),$$

$$\boldsymbol{B} = (B_x, B_y, B_z).$$

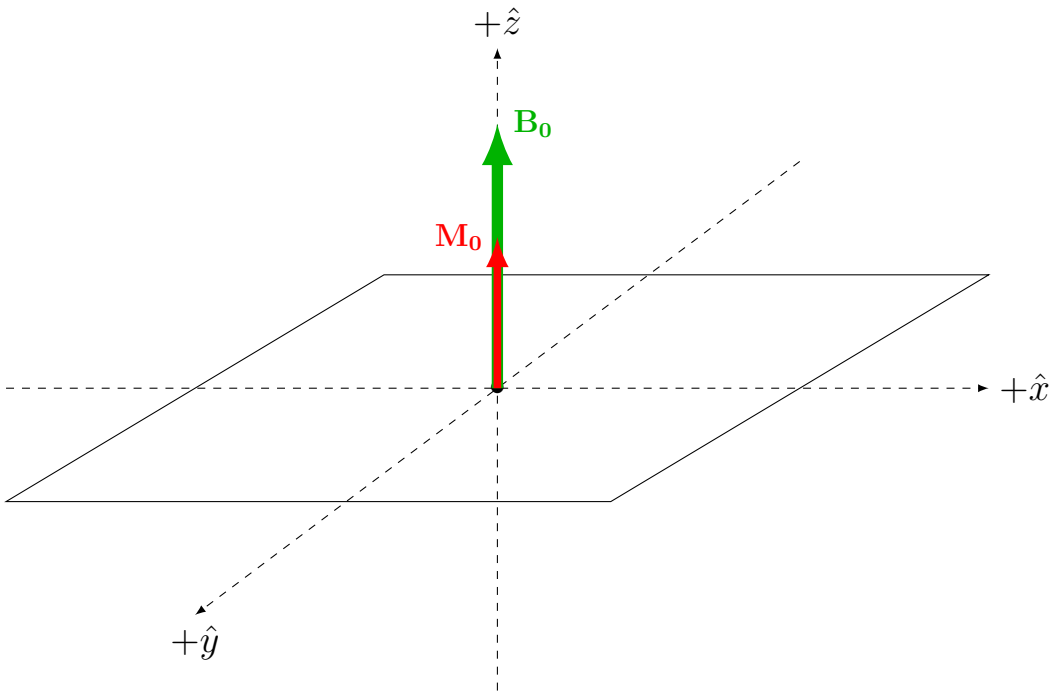

Figure 5: The ambient magnetic field vector ($\mathbf{B_0}$) along with the equilibrium position of the magnetization vector ($\mathbf{M_0}$).

For the initial conditions of the system (Figure 5), the ambient magnetic field will be in the positive $\hat{z}$-direction ($\boldsymbol{B} = B_o\hat{z}$). After a long period of time ($\sim$15 seconds), which depends on the thermal state of the system, the magnetization vector will be aligned with the ambient magnetic field; its equilibrium position, $\mathbf{M}^0 = (M_x^0, M_y^0, M_z^0)$. While the magnetization vector is in equilibrium, it is acting as a static dipole several orders of magnitude

less than the ambient field and therefore unmeasurable. In order to measure a signal from the magnetization vector, it must first be perturbed from its equilibrium position.

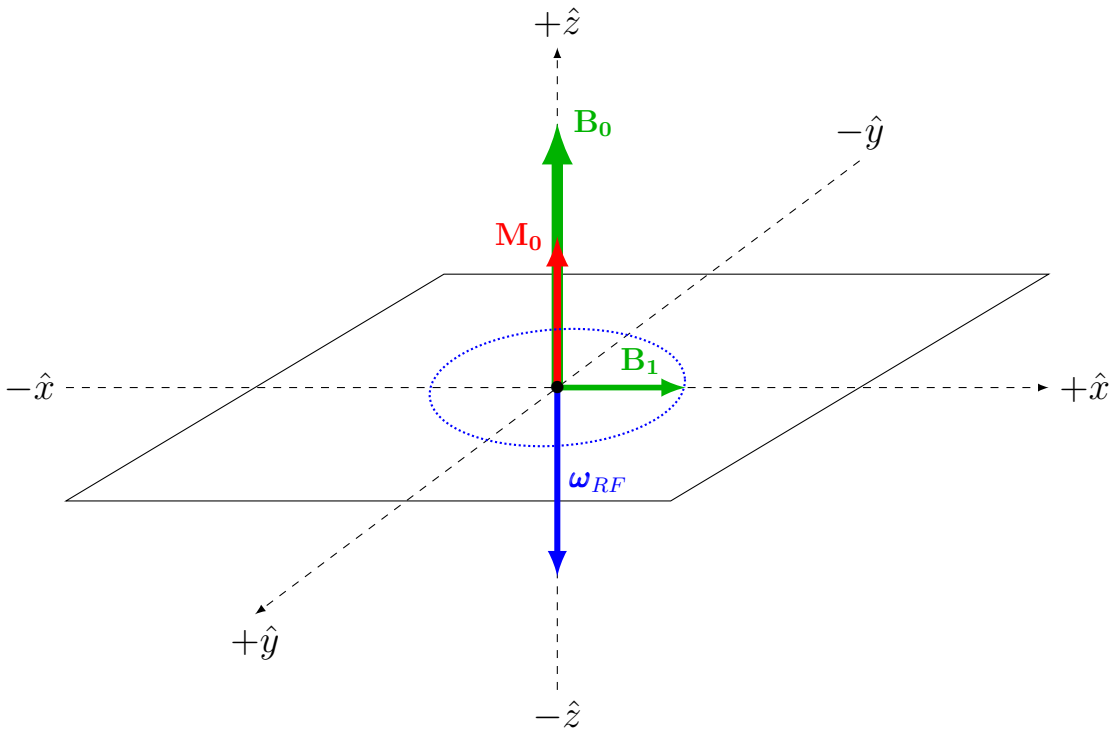

Figure 6: Magnetization vector ($\mathbf{M_0}$), the ambient magnetic field vector ($\mathbf{B_0}$), the applied field ($\mathbf{B_1}$), and the angular frequency vector ($\boldsymbol{\omega}_{RF}$) from the applied field.

The perturbation is caused by a form of radiation that induces a transition from the ground state (equilibrium) to an excited state, similar to Figure 1. In most NMR experiments, the radiation used is an oscillating magnetic field created by an alternating current through a wire loop. The component of the applied field normal to $\boldsymbol{B}_0$ (Figure 6), is instrumental to the NMR phenomenon. The inducing magnetic field is oscillating at or near the Larmor frequency (Equation 10). Once the inducing magnetic field is terminated, the magnetization vector relaxes back to its equilibrium state, precessing at the Larmor frequency. Since the magnetization vector is a magnetic dipole, it will induce an oscillating magnetic field, which is then recorded by receiver coils.

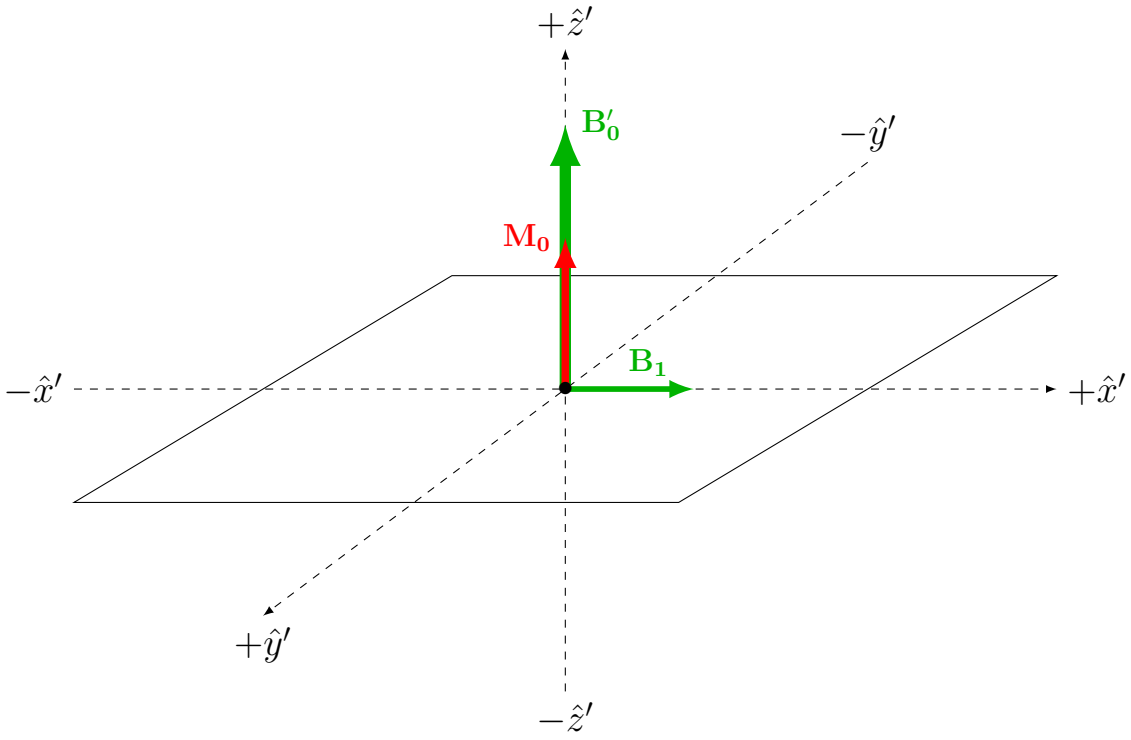

Figure 7: In the rotating frame, the magnetization vector ($\mathbf{M_0}$) is influenced by the applied field ($\mathbf{B}_1$) with angular frequency vector ($\boldsymbol{\omega}_{RF}$) and the reduced ambient magnetic field vector ($\mathbf{B_0'}$). The reduction of ambient field leads to an effective field, $\mathbf{B}_{\text{eff}}$ (mentioned shortly).

In order to solve the set of coupled differential equations, two reference frames will be incorporated, the lab frame and the rotating frame. The rotating frame $(\hat{x}', \hat{y}', \hat{z}')$ shown in Figure 7, is the lab frame (Figure 6) rotating at an angular frequency, ω_{RF}, around the $\hat{z}$-axis. To transform from our lab frame to our rotating frame, we must perform the following matrix multiplication (Anton and Rorres, 2005),

$$R_z(\theta) = \begin{bmatrix} \cos\theta & -\sin\theta & 0 \\ \sin\theta & \cos\theta & 0 \\ 0 & 0 & 1 \end{bmatrix}, \tag{22}$$

where $\theta = \omega_{RF} t$ is the angle (in radians) the frame has rotated around $\hat{z}$ in a time, t.

By introducing a rotating frame, the solution to Equation 21 is simpler to evaluate. The

system being evaluated will have the magnetization vector ($\boldsymbol{M}$), the ambient magnetic field ($\boldsymbol{B} = B_o\hat{z}$), and a secondary oscillating inducing field ($\boldsymbol{B_1}$). For the following solution, the inducing field will be along the $+\hat{x}$-axis and oscillating at an angular frequency, $\vec{\boldsymbol{\omega}}_{RF} = -\omega_{RF}\hat{z}$, where $\omega_{RF} = 2\pi f_1\hat{z}$, with f_1 being the frequency of the inducing field. The relation between the lab frame ($\mathbf{M}_{\text{lab}}$) and the rotating frame ($\mathbf{M}_{\text{rot}}$) is (Taylor, 2005),

$$\frac{d\mathbf{M}_{\text{lab}}}{dt} = \frac{d\mathbf{M}_{\text{rot}}}{dt} + \vec{\boldsymbol{\omega}}_{RF} \times \mathbf{M}_{\text{lab}}. \tag{23}$$

We can simplify Equation 23 by isolating the rotating frame, then using the anticommutative and distributive properties of the cross product,

$$\begin{aligned}\frac{d\mathbf{M}_{\text{rot}}}{dt} &= \frac{d\mathbf{M}_{\text{lab}}}{dt} - \vec{\boldsymbol{\omega}}_{RF} \times \mathbf{M}_{\text{lab}} \\ &= \gamma\mathbf{M}_{\text{lab}} \times \mathbf{B} - \vec{\boldsymbol{\omega}}_{RF} \times \mathbf{M}_{\text{lab}}, \\ &= \gamma\mathbf{M}_{\text{lab}} \times \left(\mathbf{B} + \frac{\vec{\boldsymbol{\omega}}_{RF}}{\gamma}\right).\end{aligned} \tag{24}$$

The term in brackets in Equation 24 is known as the effective field (Farrar and Becker, 1971),

$$\mathbf{B}_{\text{eff}} = \mathbf{B} + \frac{\vec{\boldsymbol{\omega}}_{RF}}{\gamma},$$

where $\mathbf{B}$ includes the ambient field and the applied (inducing) field. The ambient field ($\boldsymbol{B} = B_o\hat{z}$) is chosen to be in the $+\hat{z}$-direction, and the applied field ($\boldsymbol{B_1} = B_1\hat{x}$) in the $+\hat{x}$-direction (Figure 8). The rotational nature (ω_{RF}) of the inducing field adds a fictitious magnetic field in the -$\hat{z}$-direction. In the frame rotating at $\vec{\boldsymbol{\omega}}_{RF}$, the effective field is,

$$\mathbf{B}_{\text{eff}} = B_1\hat{x} + \left(B_o - \frac{\omega_{RF}}{\gamma}\right)\hat{z}. \tag{25}$$

Inserting $\mathbf{B}_{\text{eff}}$ into Equation 24, and expanding the determinant,

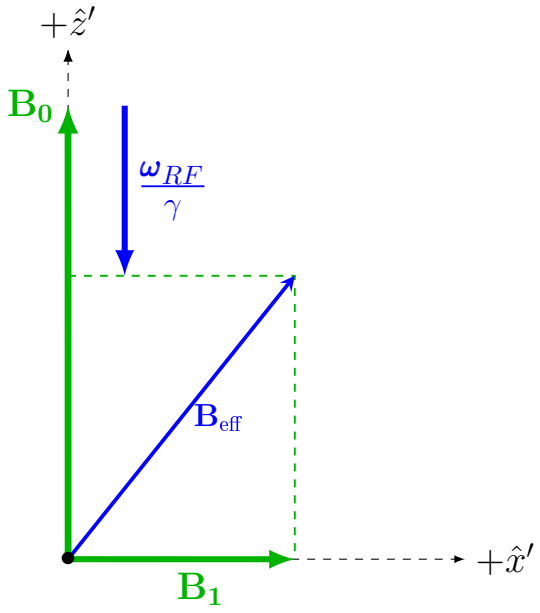

Figure 8: The development of the effective field ($\mathbf{B}_{\text{eff}}$) in the rotating frame created by the vector sum of the ambient magnetic field vector ($\mathbf{B_0}$), the applied field ($\mathbf{B}_1$), and the fictitious field ($\boldsymbol{\omega}_{RF}/\gamma$) caused by the angular frequency vector from the applied field.

$$\left(\frac{d\mathbf{M}}{dt}\right)_{\text{Rot}} = \gamma \begin{vmatrix} \hat{\mathbf{x}} & \hat{\mathbf{y}} & \hat{\mathbf{z}} \\ M_x & M_y & M_z \\ B_x & 0 & B_0 - \frac{\omega_{RF}}{\gamma} \end{vmatrix},$$

$$= \hat{x}\left[\gamma\left(M_y\left(B_0 - \frac{\omega_{RF}}{\gamma}\right) - 0\right)\right] - \hat{y}\left[\gamma\left(M_x\left(B_0 - \frac{\omega_{RF}}{\gamma}\right) - M_z B_x\right)\right] + \hat{z}\left[\gamma\left(0 - M_y B_x\right)\right]. \quad (26)$$

The components of the equations of motion (Equation 24) in the rotating frame are,

$$\frac{dM_x}{dt} = M_y(\gamma B_0 - \omega_{RF}), \quad (27)$$

$$\frac{dM_y}{dt} = \gamma M_z B_x - M_x(\gamma B_0 - \omega_{RF}), \quad (28)$$

$$\frac{dM_z}{dt} = -\gamma M_y B_x. \quad (29)$$

With the introduction of the variables,

$$\begin{aligned} \omega_L &= \gamma B_0, \\ \Delta\omega &= (\omega_L - \omega_{RF}), \\ \omega_x &= \gamma B_x, \end{aligned} \tag{30}$$

Equations 27-29 are simplified to,

$$\frac{dM_x}{dt} = M_x' = M_y \Delta\omega, \tag{31}$$

$$\frac{dM_y}{dt} = M_y' = \omega_x M_z - M_x \Delta\omega, \tag{32}$$

$$\frac{dM_z}{dt} = M_z' = -\omega_x M_y. \tag{33}$$

Since Equations 31-33 are coupled, the first step in generating a single differential equation will be to differentiate M_y',

$$M_y'' = \omega_x M_z' - M_x' \Delta\omega, \tag{34}$$

and then sub M_x' and M_z' into its result,

$$\begin{aligned} M_y'' &= \omega_x(-\omega_x M_y) - (M_y \Delta\omega)\Delta\omega, \\ M_y'' &= -\omega_x^2 M_y - \Delta\omega^2 M_y. \end{aligned} \tag{35}$$

Equation 35 is a second-order linear homogeneous differential equation, meaning it has the form, $aM_y'' + bM_y' + cM_y = 0$. In order to solve Equation 35, the solution is assumed to have the form, $M_y(t) = e^{rt}$ where r is a root to the *characteristic equation*, $ar^2 + br + c = 0$ (Boyce and DiPrima, 2000; Bronson and Costa, 2006). In our case, the characteristic equation is easily solved,

$$\begin{aligned} 0 &= r^2 + (\omega_x^2 + \Delta\omega^2), \\ r^2 &= -(\omega_x^2 + \Delta\omega^2), \\ r_{1,2} &= \pm i\sqrt{\omega_x^2 + \Delta\omega^2}. \end{aligned}$$

Using Euler's formula, $e^{i\theta} = \cos\theta + i\sin\theta$, and setting $\alpha = \sqrt{\omega_x^2 + \Delta\omega^2}$, our solution, $M_y(t) = e^{r_1 t} + e^{r_2 t}$, becomes (without initial conditions),

$$M_y(t) = C_1 \exp(0)\cos(\alpha t) + C_2 \exp(0)\sin(\alpha t),$$
$$M_y(t) = C_1 \cos(\alpha t) + C_2 \sin(\alpha t).$$

The constants, C_1 and C_2, will be solved for using initial conditions after solving $M_x(t)$ and $M_z(t)$. Solving for M_x,

$$\begin{aligned}
\frac{dM_x}{dt} &= \Delta\omega\big(C_1\cos(\alpha t) + C_2\sin(\alpha t)\big) \\
M_x &= \Delta\omega\left[\int \big(C_1\cos(\alpha t) + C_2\sin(\alpha t)\big)dt\right] + C_x \\
M_x &= \Delta\omega\left[C_1\left(\frac{1}{\alpha}\sin(\alpha t)\right) + C_2\left(\frac{-1}{\alpha}\cos(\alpha t)\right)\right] + C_x, \\
M_x &= \frac{\Delta\omega}{\alpha}\left[C_1\sin(\alpha t) - C_2\cos(\alpha t)\right] + C_x.
\end{aligned}$$

Solving for M_z,

$$\begin{aligned}
\frac{dM_z}{dt} &= -\omega_x\big(C_1\cos(\alpha t) + C_2\sin(\alpha t)\big), \\
M_z &= -\omega_x\left[\int (C_1\cos(\alpha t) + C_2\sin(\alpha t))dt\right] + C_z \\
M_z &= \frac{-\omega_x}{\alpha}\left[C_1\sin(\alpha t) - C_2\cos(\alpha t)\right] + C_z.
\end{aligned}$$

In order to find the constants of integration, $C_1,\ C_2,\ C_x$, and C_z, we must incorporate the initial conditions (when t=0),

$$\begin{aligned}
M_x(0) &= M_x^0, \\
M_y(0) &= M_y^0, \\
M_z(0) &= M_z^0.
\end{aligned} \tag{36}$$

The initial conditions represent when the magnetization vector is at equilibrium. At $t = 0$, the equilibrium position is when the magnetization vector is influenced only by the ambient

magnetic field and is aligned with that field.

For the first constant, C_1,

$$\begin{aligned} M_y(0) = C_1\cos(0) + C_2\sin(0) &= M_y^0, \\ C_1 &= M_y^0, \end{aligned}$$

and for C_2,

$$\begin{aligned} M_y'(0) = \alpha\Big[C_2\cos(0) - C_1\sin(0)\Big] &= \omega_x M_z(0) - M_x(0)\Delta\omega, \\ \alpha C_2 &= \omega_x M_z(0) - M_x(0)\Delta\omega, \\ C_2 &= \frac{\omega_x M_z^0 - M_x^0\Delta\omega}{\alpha}. \end{aligned}$$

The other two constants, C_x and C_z, can now be solved,

$$\begin{aligned} M_x(0) =& \frac{\Delta\omega}{\alpha}\left[M_y^0\sin(0) - \frac{\omega_x M_z^0 - M_x^0\Delta\omega}{\alpha}\cos(0)\right] + C_x = M_x^0, \\ M_x^0 =& \frac{\Delta\omega}{\alpha}\left[\frac{M_x^0\Delta\omega - \omega_x M_z^0}{\alpha}\right] + C_x, \\ C_x =& M_x^0 - \frac{\left[M_x^0\Delta\omega^2 - \omega_x\Delta\omega M_z^0\right]}{\alpha^2}, \end{aligned}$$

and,

$$\begin{aligned} M_z(0) =& \frac{-\omega_x}{\alpha}\left[M_y^0\sin(0) - \frac{\omega_x M_z^0 - M_x^0\Delta\omega}{\alpha}\cos(0)\right] + C_z = M_z^0, \\ M_z^0 =& \frac{-\omega_x}{\alpha}\left[\frac{M_x^0\Delta\omega - \omega_x M_z^0}{\alpha}\right] + C_z, \\ C_z =& M_z^0 - \frac{\left[\omega_x^2 M_z^0 - \omega_x M_x^0\Delta\omega\right]}{\alpha^2}. \end{aligned}$$

The final solutions, without relaxation,

$$M_x(t) = \frac{\Delta\omega}{\alpha}\left[M_y^0 \sin(\alpha t) - \frac{\omega_x M_z^0 - M_x^0 \Delta\omega}{\alpha}\cos(\alpha t)\right] + M_x^0 - \frac{\left[M_x^0 \Delta\omega^2 - \omega_x \Delta\omega M_z^0\right]}{\alpha^2}, \quad (37)$$

$$M_y(t) = M_y^0 \cos(\alpha t) + \frac{\omega_x M_z^0 - M_x^0 \Delta\omega}{\alpha}\sin(\alpha t), \quad (38)$$

$$M_z(t) = \frac{-\omega_x}{\alpha}\left[M_y^0 \sin(\alpha t) - \frac{\omega_x M_z^0 - M_x^0 \Delta\omega}{\alpha}\cos(\alpha t)\right] + M_z^0 - \frac{\left[\omega_x^2 M_z^0 - M_x^0 \omega_x \Delta\omega\right]}{\alpha^2}. \quad (39)$$

To complete the Bloch equations, relaxation must be incorporated. Bloch assumed that spin-lattice and spin-spin relaxation could be treated as first-order processes with characteristic times T_1 and T_2, respectively. The concept of spin-lattice and spin-spin relaxation will be addressed shortly, although for the solution to the Bloch equations, one only needs to know that the decay is a first-order process. The longitudinal magnetization (M_z) has the decay constant, T_1, and the transverse magnetization (M_x and M_y) has the decay constant, T_2. These constants represent the time it takes for each of the magnetization components to decay to 37% of their initial condition value.

When introducing the linear decay to each of the components we get,

$$M_x' = -(M_x(t) - M_x^0)/T_2, \quad (40)$$

$$M_y' = -(M_y(t) - M_y^0)/T_2, \quad (41)$$

$$M_z' = -(M_z(t) - M_z^0)/T_1, \quad (42)$$

where the equilibrium of the magnetization vector is now aligned with the effective field (Equation 25). In most cases, $\mathbf{B}_{\text{eff}}$ will only include the ambient field (B_o). However, in some cases, $\mathbf{B}_{\text{eff}}$ will be constantly changing and the magnetization vector will always try to relax to a state of lowest energy, which is $\mathbf{B}_{\text{eff}}$.

Since Equations 40-42 are the same style of differential equation, only a solution to

Equation 40 will be outlined explicitly. The first step in solving the differential equation is to group *like* terms on either side of the equality sign, and then the next step is to integrate (Bronson and Costa, 2006),

$$\begin{aligned}
\frac{dM_x}{dt} &= -(M_x - M_x^0)/T_2, \\
\int \frac{dM_x}{M_x - M_x^0} &= \int -dt/T_2, \\
\ln(M_x - M_x^0) &= -t/T_2 + C, \\
M_x - M_x^0 &= e^{-t/T_2} + e^C = Ce^{-t/T_2}.
\end{aligned}$$

Solving for C, using initial conditions,

$$\begin{aligned}
M_x(0) - M_x^0 &= Ce^0, \\
M_x(0) - M_x^0 &= C.
\end{aligned}$$

Now, solving for M_x,

$$\begin{aligned}
M_x(t) - M_x^0 &= \big(M_x(0) - M_x^0\big)e^{-t/T_2}, \\
M_x(t) &= M_x(0)e^{-t/T_2} - M_x^0 e^{-t/T_2} + M_x^0, \\
M_x(t) &= M_x(0)e^{-t/T2} + M_x^0\big(1 - e^{-t/T2}\big). \qquad (43)
\end{aligned}$$

The above technique can then be applied to the M_y and M_z components. It is important to note that $M_x(t)$ is the evolution of the x-component of the magnetization vector over time. $M_x(0)$ is the initial condition value at the point that the decay begins; this is usually once the applied field has been turned off. In some cases, the initial conditions will be changing continually, so the differential equations will have to be re-evaluated.

Analytically, these solutions are laborious and not feasible, but numerically they work excellently. When modeling the magnetization vector numerically, one begins by solving Equations 37-39 at an instant of time (t_1), then the values of $M_x(t_1)$, $M_y(t_1)$, and $M_z(t_1)$

become the $M_x(0)$, $M_y(0)$, and $M_z(0)$ in the relaxation equations (Equation 43). Every iteration will use the previous $M_{x,y,z}$ results as the new initial conditions (Equation 36).

A numerical model of the magnetization vector and its interaction with an on-resonance radio-frequency pulse ($\omega_{RF} = \omega_L$) is illustrated in Figure 9. By being on-resonance, the analytical solution to the Bloch equations (Equations 27-29) becomes simpler to solve because $\Delta\omega = 0$ in Equation 30.

The model in Figure 9 begins with the magnetization vector, $\mathbf{M}$, being exposed to only the the ambient magnetic field, $\mathbf{B_0}$, and by consequence, aligned with $\mathbf{B_0}$ (Figure 9a). When $\mathbf{B_0}$ is the only magnetic field present, the effective field, $\mathbf{B}_{\text{eff}}$, is the same as $\mathbf{B_0}$.

The magnetization vector is then exposed to an on-resonance energising pulse, $\mathbf{B_1}$. Since the energising pulse is on-resonance, it creates an effective field ($\mathbf{B}_{\text{eff}}$) in the direction of the energising field ($+\hat{x}$-axis, in Figure 9b). The magnetization vector then rotates directly towards -$\hat{y}$ without any precession, due to the torque imposed on it by $\mathbf{B_1}$ (Figure 9c). After $\mathbf{M}$ hits -$\hat{y}$, $\mathbf{B_1}$ is terminated and $\mathbf{B}_{\text{eff}}$ is again equal to $\mathbf{B_0}$, which causes $\mathbf{M}$ to begin to precess and decay toward $\mathbf{B}_{\text{eff}}$ (Figure 9d).

Figures 9e and 9f show the state of the relaxation at an early time and later time, respectively. The relaxation involves the magnetization vector precessing about $\mathbf{B}_{\text{eff}}$ at the Larmor frequency until it eventually becomes aligned with $\mathbf{B}_{\text{eff}}$. The time it takes to be exactly aligned with $\mathbf{B}_{\text{eff}}$ is dependent on T_1 and T_2 (Equations 40-42). The $\hat{x}$-component of the magnetization through excitation and relaxation is displayed in Figure 10.

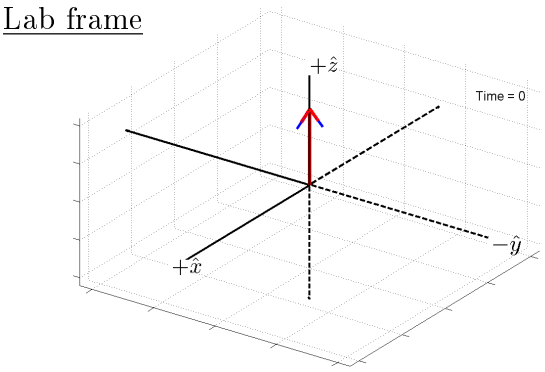

(a) Before excitation, **M** is aligned with $\mathbf{B_0}$, which is also $\mathbf{B}_{\text{eff}}$.

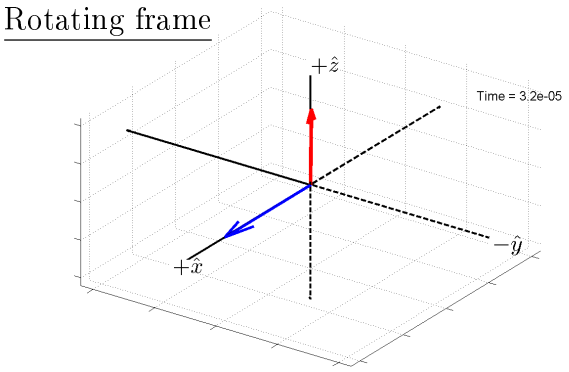

(b) The instant when $\mathbf{B_1}$ is applied (along $+\hat{x}$) and **M** begins to tip towards -$\hat{y}$.

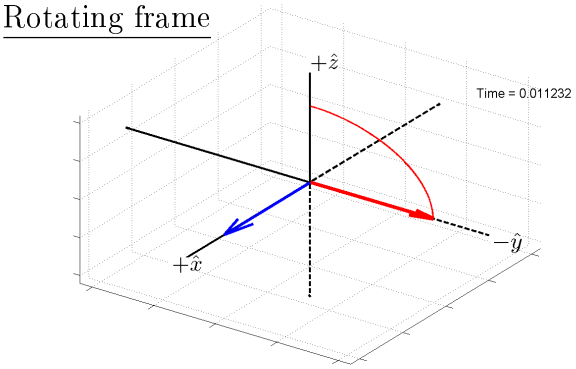

(c) $\mathbf{B_1}$ transmits long enough to allow **M** to move directly from $+\hat{z}$ to -$\hat{y}$.

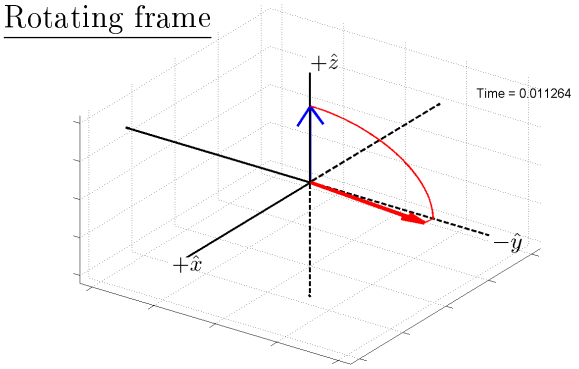

(d) When $\mathbf{B_1}$ is terminated, $\mathbf{B}_{\text{eff}}$ is entirely comprised of $\mathbf{B_0}$. Then, **M** begins precession and decay towards $\mathbf{B_0}$. A very small rotation around the $+\hat{z}$-axis is evident.

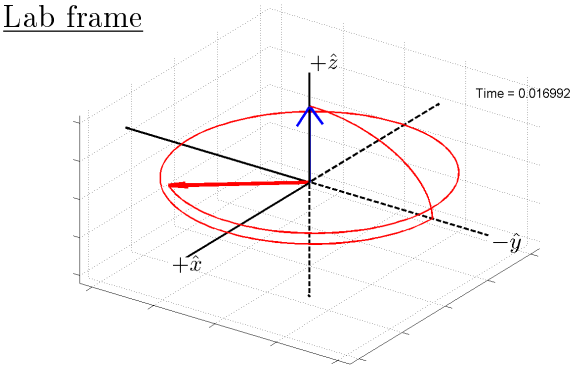

(e) **M** precessing around $\mathbf{B}_{\text{eff}}$, its relaxation process. The red route shows the tip of **M** after it has rotated $1\frac{1}{3}$ times around the $+\hat{z}$-axis.

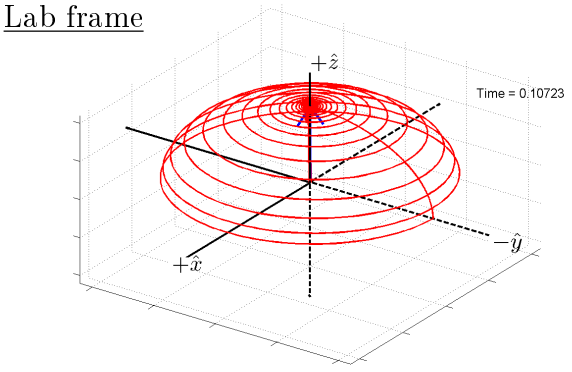

(f) **M** has fully relaxed, now aligned with $\mathbf{B}_{\text{eff}}$.

Figure 9: The evolution of the magnetization vector before (a), during (b)-(c), and after (d)-(f) an on-resonance radio-frequency pulse. The magnetization vector and the path it traces out during excitation and relaxation is given in red. The effective field (Equation 25) is given in blue. The $\hat{x}$-component of **M** throughout this process is shown in Figure 10.

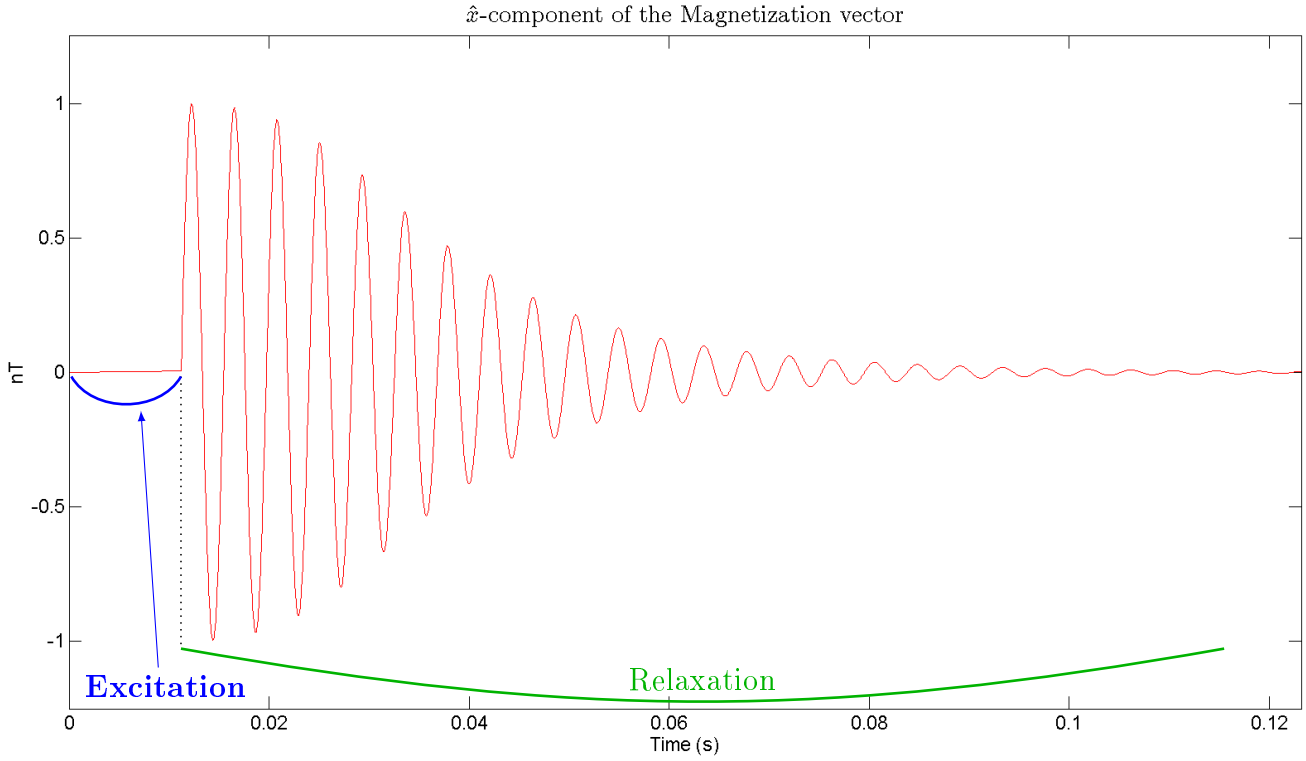

Figure 10: The $\hat{x}$-component of the magnetization vector during excitation and relaxation.

Chapter 3

3 Application of NMR to water exploration

When using NMR for water exploration in the context of geophysics, the net non-zero nuclear spin of the water molecule (Figure 11) is exploited. The water molecule consists of one oxygen atom with a zero-spin nucleus, 8 paired electrons in the valence shell resulting in zero electron spin, and two protons from the hydrogen nuclei. The protons from the hydrogen nuclei are what give the water molecule an overall net spin of 1/2 and thus the same gyromagnetic ratio as the proton (i.e., $\gamma_{water} = \gamma_p$)

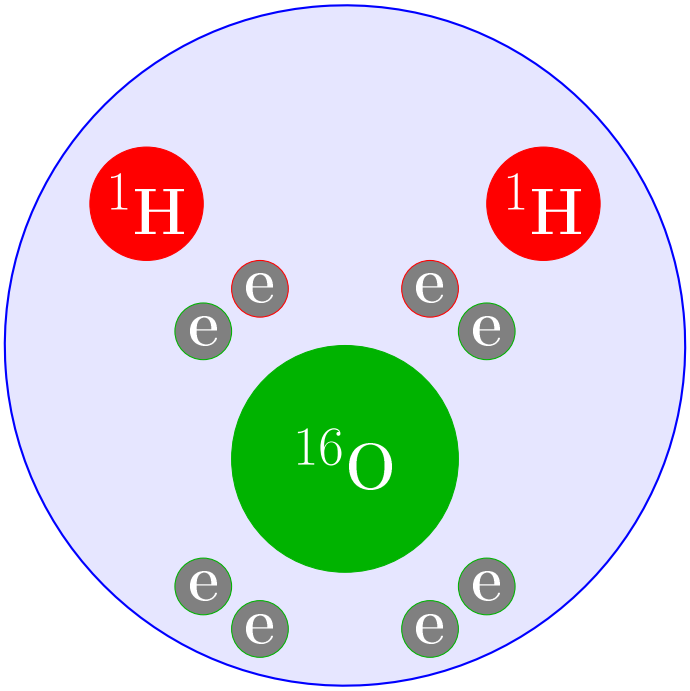

Figure 11: A schematic diagram of a water molecule contains two hydrogen nuclei and one oxygen nucleus. All electrons in the valence shell are paired up, so there is no electron spin contribution. The oxygen nucleus has an even number of protons and an even number of neutrons, so no nuclear spin contribution. The two hydrogen nuclei are comprised of one proton, which both have spin-1/2 which makes the water molecule act as spin-1/2 particle.

Since the NMR technique is measuring the response from the hydrogen protons in liquids, it is possible to get an NMR response from various substances other than freshwater, such as brackish water or hydrocarbons. When exploring for hydrocarbons, borehole logging NMR methods are employed, which is discussed in Brown and Gamson, 1960. Although important, borehole NMR is not pertinent to this study. The distinction between freshwater and brackish water is not apparent in the NMR relaxation signal; there would need to be a secondary resistivity survey conducted (e.g., Behroozmand et al., 2012) or studying the phase of the NMR signal (e.g, Shushakov, 1996). Typically, in geophysical surveys, the Larmor frequency for water (f_L^{water}) is found first by measuring the magnetic field at the survey site

and then using Equation 10 with γ_p,

$$f_L^{water} = 0.042577 \text{ Hz/nT} \times |B_o|. \tag{44}$$

Geophysical surveys conducted using NMR theory are called magnetic resonance sounding (MRS) or surface nuclear magnetic resonance (sNMR). The physical parameters measured in the subsurface are water content and pore size. The water content is determined from the initial amplitude, E_0, of the NMR relaxation signal and the pore size is related to the rate of decay, T_2^* (similar to T_2 in Equations 40-41), of the NMR relaxation signal (Kirsch, 2006) as illustrated in Figure 12. Only in the case of a uniform magnetic field, will $T_2 = T_2^*$. T_2^* is an effective decay constant which is comprised of the relaxation rate of the bulk fluid in a uniform field, the surface relaxation rate, and the inhomogeneous field dephasing rate (Grunewald and Knight, 2011). The range of T_2^* values for water in various geological environments is shown in Table 2.

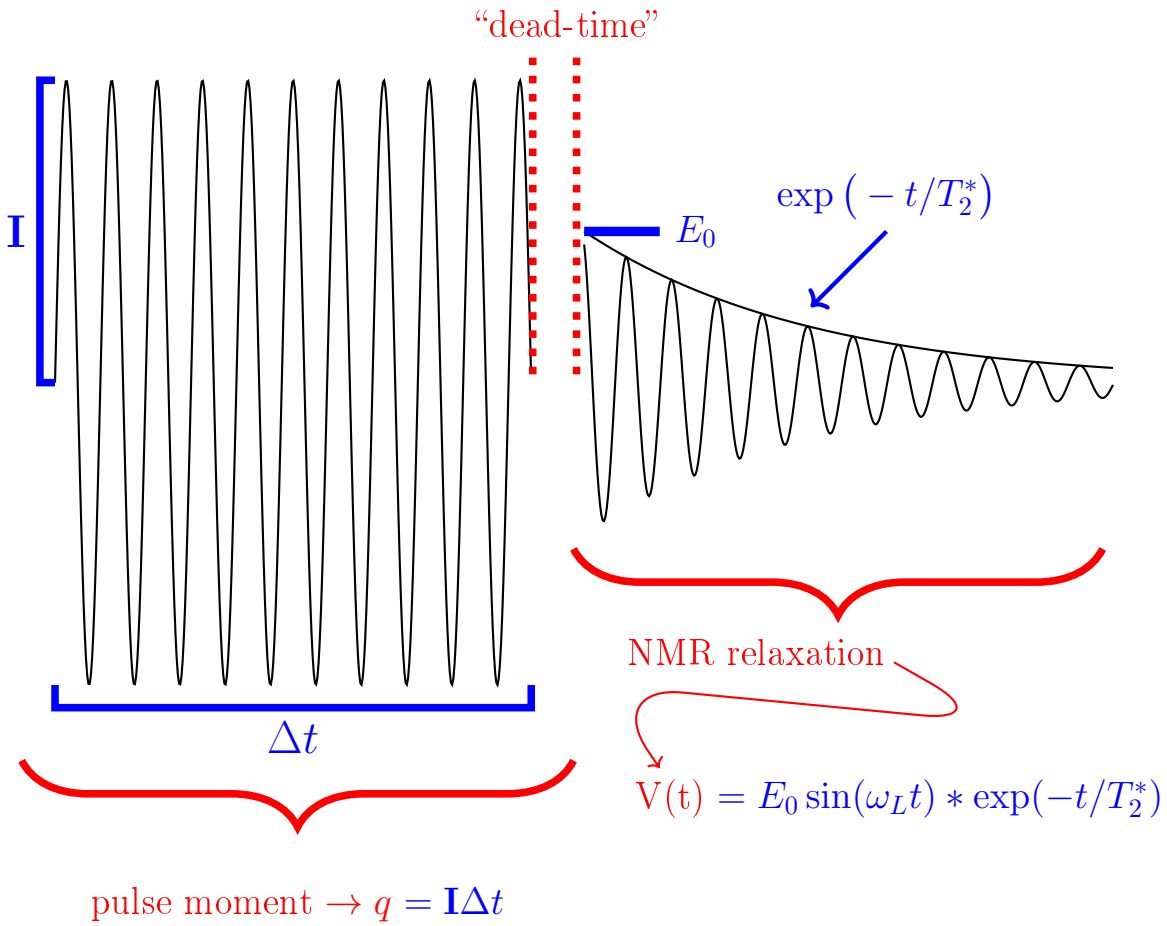

Figure 12: How the pulse technique in sNMR surveys is utilized. The transmitting coil will send an energising pulse, with a current (**I**) for a length a time (Δt) followed by an abrupt turn-off. After the turn-off, there is a "dead-time" which allows for the electronics to change the transmitting loop to a receiving loop. Once switched over, the NMR relaxation is measured.

When there is a large volume of water in the subsurface, the magnetization vector (Equation 18) will have a stronger dipole moment and thus create a larger initial signal (E_0). If the water is located in larger pores, it will lose energy slower to its surroundings and the decay constant (T_2^*) will be larger resulting in a longer relaxation to equilibrium (Levitt, 2008).

Table 2: Approximate decay times (T_2^*) for water in various geological conditions. The more porous media correlate with larger relaxation times. The decay times were summarized from Behroozmand et al., 2014; Bernard and Legchenko, 2003; Legchenko et al., 2002.

Water environment	T_2^* (ms)
lake or river	1000-3000
gravel	500-3000
medium sand	100-1000
fine sand	20-200
silt	5-30
clay	<5

The most popular technique used in sNMR is the pulse method or Free Induction Decay (FID), which involves irradiating the subsurface with an oscillating magnetic field at or near the Larmor frequency and measuring the decay curve after the oscillating field is switched off (Figure 12). Adiabatic passage is another technique which incorporates a frequency sweep that starts below the Larmor frequency and slowly increases continuously to the Larmor frequency and then past to a predetermined frequency.

3.1 Pulse techniques

In typical geophysical surface NMR, they employ a radio-frequency pulse and then measure the relaxation after the pulse. The pulse being a sinusoidal wave oscillating at or very near the Larmor frequency. For geophysical surveys, they usually work with a *pulse moment*, $q = \mathbf{I}\Delta t$, where $\mathbf{I}$ is the current through the transmitting loop and Δt is the length of the time that the current is on for, usually between 35-40 milliseconds (Behroozmand et al., 2014; Hertrich, 2008).

After the pulse, there is a "dead-time" of about 35 ms which is when the transmitting loop turns into a receiver loop (Bernard, 2007). After the electronics have switched over, the

NMR relaxation is measured. The NMR relaxation is a sinusoidal exponentially decaying waveform. The frequency of the pulse and the decay is equal to the Larmor frequency, f_L. The exponential decay has a time constant, T_2^*, which combines various subsurface water-soil parameters and is described in Grunewald and Knight, 2011. The general outline of the pulse technique is displayed in Figure 12.

Generally, in an sNMR survey the subsurface is irradiated with a time-varying magnetic field (or, energising field), $\mathbf{B_1}(t)$, oscillating at or near the Larmor frequency (which is found by first measuring the local magnetic field). $\mathbf{B_1}(t)$ irradiates the subsurface for a predetermined length of time, Δt. Macroscopically speaking, the energising field will perturb the magnetization vector such that it tips away from its equilibrium position. The direction of the magnetization tip and angle depends on the frequency, pulse length, and the energising field's strength and direction.

Firstly, if the frequency of the energising pulse is exactly at the Larmor frequency, it is known as on-resonance excitation, but if it is not equal to the Larmor frequency then it is known as off-resonance excitation. If the excitation is on-resonance then the effective field (Equation 25) will only be $\mathbf{B_1}$ and the magnetization vector will begin to rotate from its equilibrium position ($+z$-axis) through the yz-plane towards the $-y-$axis, using the coordinate system in Figure 7.

Assuming the excitation is on-resonance, then the length of time, Δt, that is needed to tip the magnetization vector by 90 degrees ($\theta = \pi/2$) can be calculated. By tipping the magnetization vector by 90 degrees (i.e., along the $+y$-axis) and then after terminating the energising pulse, the decay signal will be most prominent (Levitt, 2008). In the on-resonance case, the magnetization vector will effectively only have $\mathbf{B_1}$ acting on it, so it will begin to precess around $\mathbf{B}_{\text{eff}} = \mathbf{B_1}$ at angular frequency, $\boldsymbol{\omega_1} = \gamma_p \mathbf{B_1}$ (using Equation 30). Multiplying

$\boldsymbol{\omega_1}$ by Δt, we are able to find an angle given as, $\theta = \gamma_p \mathbf{B_1} \Delta t$. Then setting $\theta = \pi/2$, the pulse time for a 90 degree rotation can be solved for, $t_{90} = \frac{\pi}{2\gamma_p \mathbf{B_1}}$ (Farrar and Becker, 1971; Yaramanci, 2000).

Geophysicists then use the aforementioned knowledge to determine the proper input current ($\mathbf{I} \propto \mathbf{B_1}$) and pulse time length (t_{90}) to give the best possible NMR decay curve. The method of off-resonance excitation is not a primary sNMR survey technique, at this time. The off-resonance excitation method uses an energising pulse that is not equal to the Larmor frequency, which creates a more complex trajectory of the magnetization vector. The off-resonance method will be described briefly in the next section, but a more thorough description can be found in Walbrecker et al., 2011 and Grombacher and Knight, 2015. The evolution of the sNMR technique and the underlying principles are summarized in Hertrich, 2008 and Behroozmand et al., 2014

3.2 Adiabatic passage

The adiabatic passage method in NMR is outlined in many textbooks, such as Becker, 2000. The technique is mostly used in lab experiments and in the field of medicine (e.g., Tannus and Garwood, 1997). The usage in geophysics is not as prominent, but has begun to show in the literature (e.g., Grunewald et al., 2016). Grunewald et al. is the first paper that delves into the consequences of adiabatic pulses and their uses, whereas previous geophysical experiments never dealt with the method. The study found that the adiabatic passage technique was able to show a two to three times increase in signal amplitude when compared to on-resonance pulses, which also improves sensitivity and detection in high noise (or low water content) areas.

The adiabatic method, which is known as *adiabatic passage* in the field, is similar to the pulse method in the sense that a radio-frequency is used, except a time-varying frequency.

The time-varying frequency is usually a linear increase in frequency over a predetermined amount of time and can be thought of as a frequency sweep. Instead of having a fixed frequency in the energising pulse, the frequency varies. In order to be an adiabatic pulse, the condition (following Grunewald et al.'s notation),

$$\gamma_p |\mathbf{B}_{\text{eff}}(t)| >> \frac{d\alpha}{dt}, \tag{45}$$

must be met. In this notation, $\mathbf{B}_{\text{eff}}(t)$ is the effective field (Equation 25) and α represents the angle between the ambient field vector and the effective field direction ($\mathbf{B_0}$ and $\mathbf{B}_{\text{eff}}$ in Figure 8, respectively).

Since the frequency is changing, it is not considered on-resonance excitation, but more off-resonance excitation. The beginning of the frequency sweep has a frequency lower than the Larmor frequency and steadily increases it. The effective field will be a combination of the applied field, $\mathbf{B_1}$, and the ambient magnetic field, $\mathbf{B_0}$, which creates a more complex trajectory for the magnetization vector, shown in Levitt (2008) and Becker (2000).

Although the use of adiabatic passage in geophysics is in its infancy, it has a lot of potential, as described in Grunewald et al. (2016). The surveys conducted for this thesis project were a combination of adiabatic passage and pulse methods. If an NMR signal from the protons in water molecules can be measured with an off-resonance excitation technique, then it would be more practical for an airborne system to be developed, as a frequency that is close to the Larmor, but away from the harmonics of a time-domain frequency system could be used. As the Earth's magnetic field changes along a flight line, the Larmor frequency may move to the same frequency as an odd harmonic of the base frequency of the EM system. In this specific case, recording the NMR signal would be unlikely, due to the dominating contribution of the base frequency harmonic.

Chapter 4

4 Field surveys

The goal of the project was to determine whether it was possible to record an NMR response from freshwater using a traditional ground-based electromagnetic prospecting system. Accordingly, two experimental surveys were conducted near Sudbury, Ontario, Canada. One survey was conducted over an ice-covered lake, which contained a large volume of freshwater, and the other survey was conducted over an equal volume of land, with little to no water present in the subsurface. By performing the survey over an ice-covered lake, we will be in an environment most favourable to locate an NMR signal; similar to the previous studies, Müller-Petke et al., 2011 and Parsekian et al., 2013.

The geometric configuration and instrumentation for both surveys was exactly the same, with the exception of a slightly larger areal extent for the lake survey. The premise of doing the same technique at two separate survey areas with an extreme contrast in water volume, was to allow for direct comparison in the collected data, between areas with and without significant freshwater.

Instead of a pulse of a set frequency, a frequency sweep was used. The transmitter began below the Larmor frequency and then steadily increased linearly to incorporate and then surpass the Larmor frequency, followed by an abrupt termination of the transmitter. The frequency sweep is similar to adiabatic passage and the abrupt termination is similar to the pulse method.

By instigating the frequency sweep, the possibility of off-resonance excitation through adiabatic passage was investigated, whilst the abrupt termination of the transmitter permitted the analysis of an off-resonance pulse response. By collecting off-resonance excitation

data, we can assess the practicality of an airborne NMR system, as will be discussed later.

4.1 Survey design

4.1.1 Method & set-up

The primary field was generated using a 20 metre by 20 metre square loop of 2 millimetre copper wire with a current of 0.8-1.0 Amperes (Figure 13). A 120-second-long oscillating pulse of current was sent through the transmitting loop. The oscillating pulse employed a linear frequency sweep from 2300 to 2400 Hz, which resulted in a change in frequency of approximately 0.833 Hz/s (Figure 14). The Larmor frequency was within the range of the frequency sweep for both survey locations. The sweep was sufficiently slow to ensure that the adiabatic condition (Equation 45) was met.

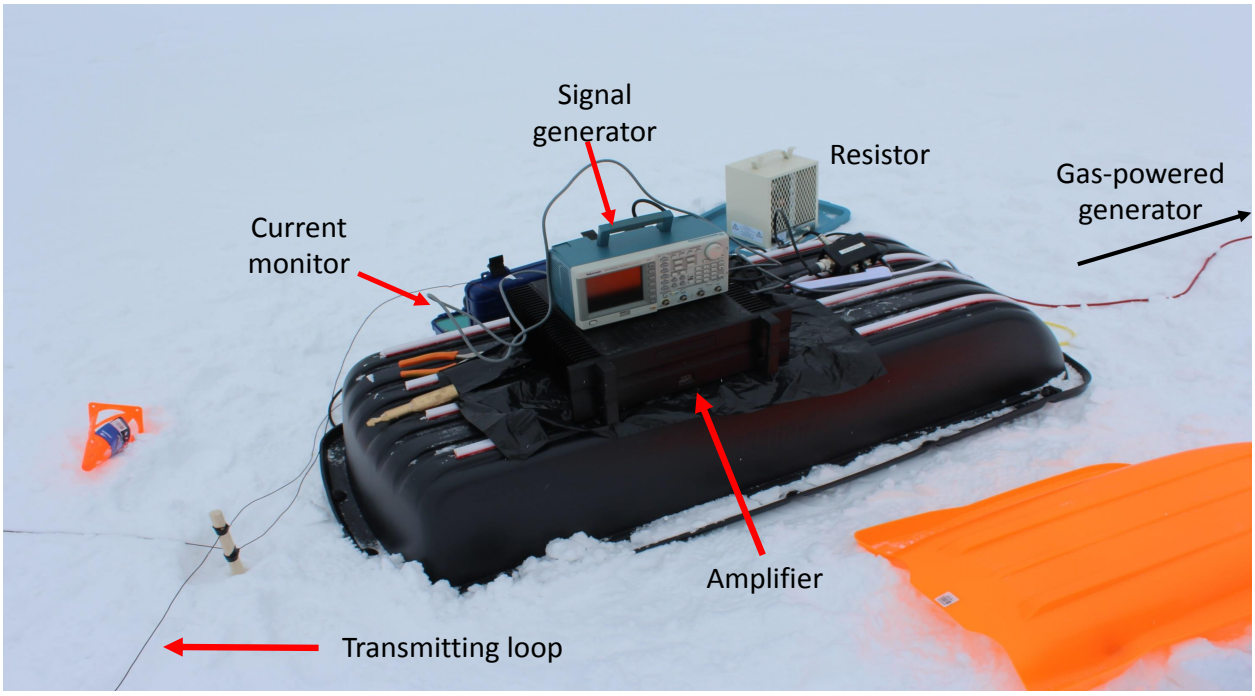

Figure 13: Electronics set-up used for the surveys.

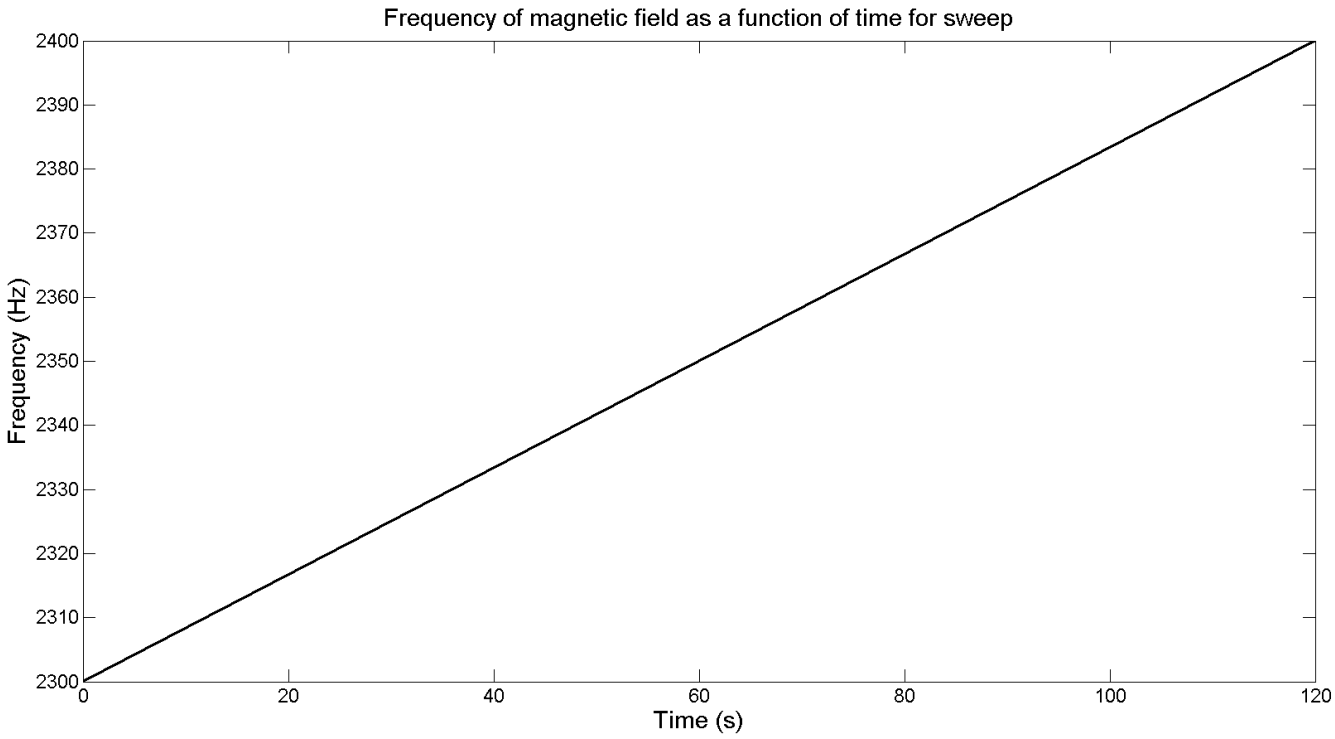

Figure 14: Frequency sweep for the surveys.

Magnetic field measurements were collected using ANT-23 magnetometers (noise and sensitivity levels shown in Appendix B). There were 3 separate magnetometers placed in 3 axial directions, perpendicular to each other, so that the three components of the measured magnetic field could be resolved. The receiver box, which contains the 3 magnetometers, and the data recorder are shown in Figure 15.

In sNMR surveys, the transmitting loop is also used as a receiver loop; contrary to our survey. The magnetometers used for our survey are used for mineral exploration on an AEM system, which relates to the original goal of our project and the reason why these sensors were chosen over a loop receiver. Although using a loop to record the NMR field is traditionally preferred, a magnetometer is also able to measure an NMR signal as shown in Davis et al. (2014).

While the transmitting coil was performing the sweep, data from the receiver box and the current monitor were collected on data recorders at a sampling frequency of 31250 Hz (f_s), meaning that the magnetic field strengths or current was measured every $1/f_s$ seconds. The recorders were all GPS time synchronous, which means that each data point collected is at the same time in all systems allowing for direct comparison. The receiver data recorders collected the magnetic field strengths in each of the 3 directions and the current monitor recorder collected the current going through the transmitting loop. The recorders collected data continuously for the entire survey, meaning they were never turned off between sweeps.

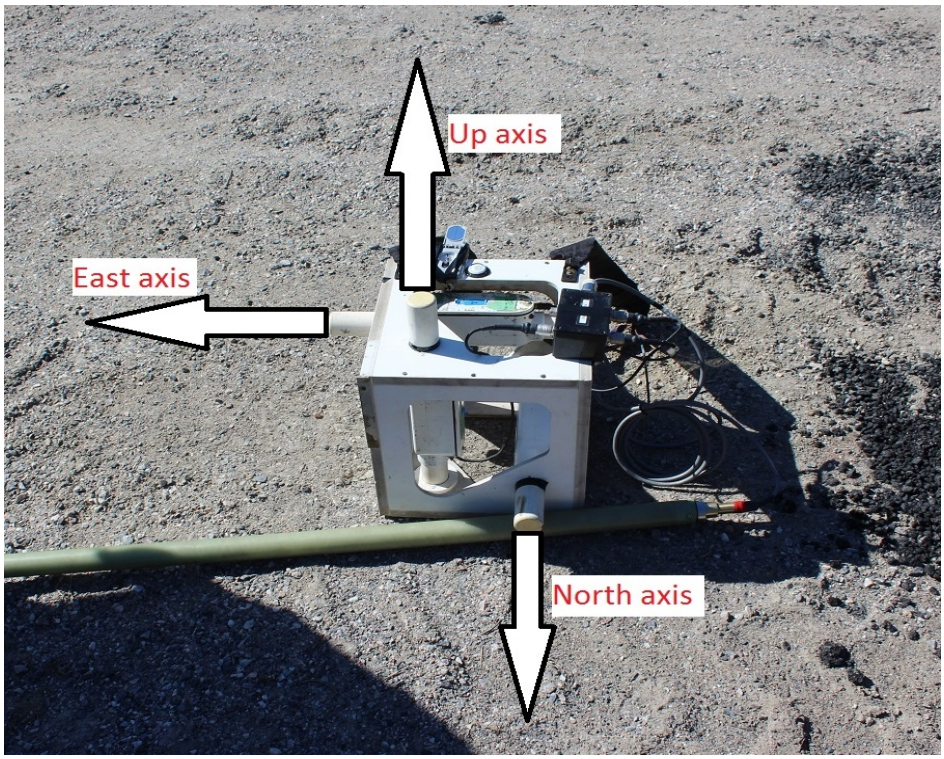

Figure 15: Receiver coils. The north, east, and up coils are highlighted with the data collection recorder lying next to the receiver box (the data recorder was designed to be lowered down a narrow drill hole).

In the lake area survey (Figure 16) the frequency sweep was repeated 42 times and monitored at 42 different receiver positions and in the land area survey (Figure 17) it was measured at 32 receiver positions.

Figure 16: Lake survey area. The view is looking north along line 1 with the electronics set-up to the west (left side in picture). The receiver locations have been cleared of snow and marked with spray paint; several locations are visible in the image.

Figure 17: Land survey area. The first several receiver positions are marked with pylons and paint.

The general orientation and position of the receivers is displayed in Figure 18. The components, if imagined in Cartesian coordinates, are $\hat{x}$, $\hat{y}$, and $\hat{z}$, although, the following nomenclature will be used henceforth: the $\hat{z}$ component is labeled as the **up** coil, the $\hat{x}$ component as the **east** coil, and the $\hat{y}$ as the **north** coil. The axes are represented in Figure 15, where the east, north, and up coils are displayed. The waveform collected from the current monitor (transmitting loop) will be labeled as **CM**. The loop was set such that line 1 (Figure 18) would be aligned with magnetic north, determined using a compass. For every single receiver position (lines 1 & 2), the north axis was always pointed in the direction of magnetic north.

All plot labels will reference an area (lake or land), a line number (1 or 2), and a position number (receiver box position) which can always be referenced to Figure 18. All receiver positions were 2 metres away from each other except for the positions adjacent to the loop and the center loop position. The receivers adjacent to the loop were 4 metres from the loop. The centre position, P11, was located directly in the middle, 10 metres from each side of the wire loop. The placing of the receiver box at various distances from the loop allowed us to simulate the approximate geometric configuration of an AEM system. The in-loop receiver box positions would represent a coincident loop receiver-transmitter pair and the receiver box positions outside of the loop would represent a separated receiver-transmitter pair. Multiple positions were tested to see if one might provide a larger signal.

The lake survey did not record any up-coil data (due to a loose connection), except for a couple of random stations. Also, no data were collected for lake, line 2, PN#'s 8, 9, and 13, which was due to the signal generator operator failing to properly initiate the transmitting sweep (i.e., not fully pressing the START button).

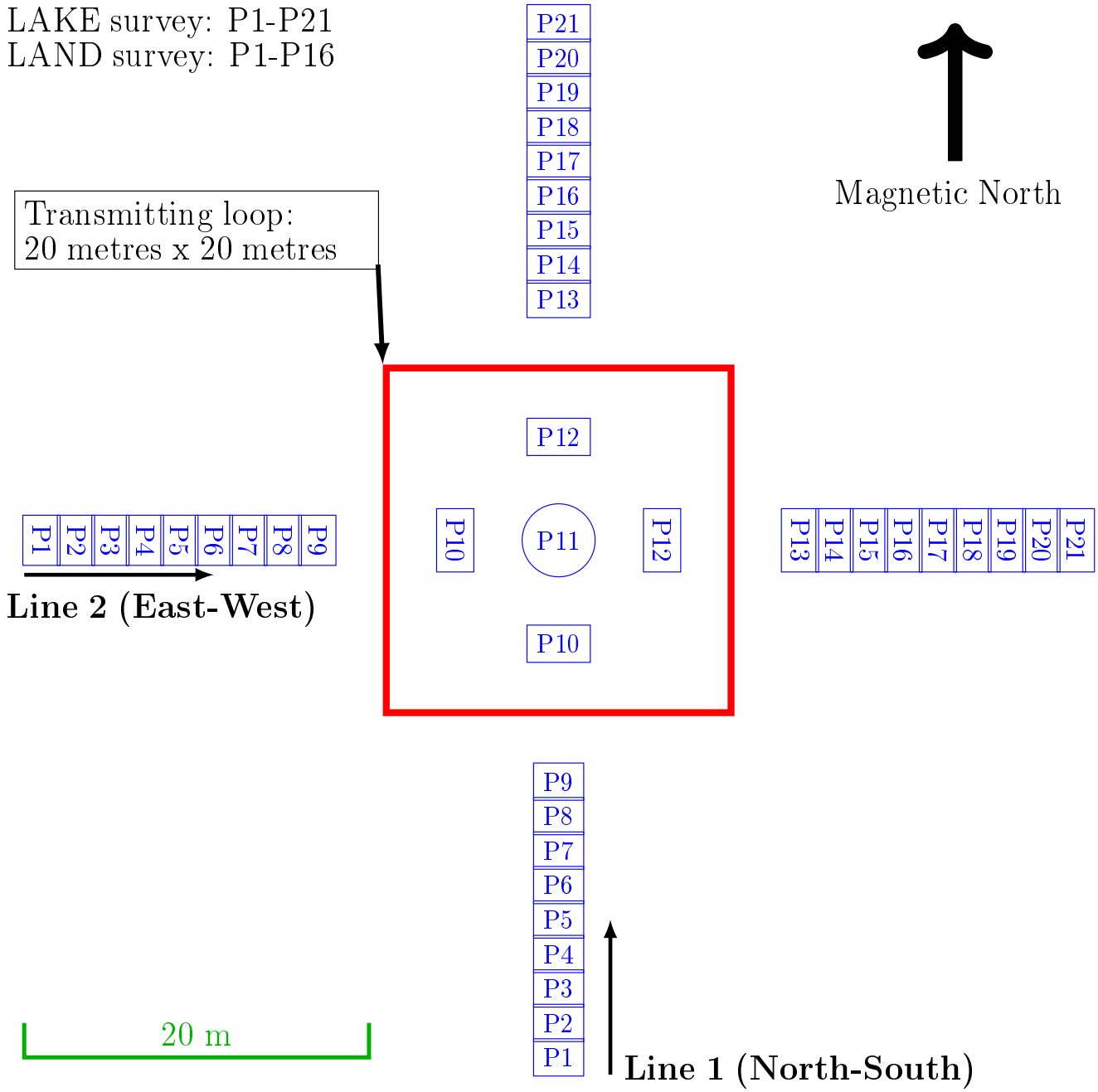

Figure 18: General setup for both the lake and land surveys. Each receiver position is labeled 'P#'. The lake survey had 21 receiver positions per line and the land survey only had 16 receiver positions per line. Both lines shared a common position, P11. All stations are 2 metres away from each other except for the positions that are adjacent to the loop and the centre position, P11. Receiver positions adjacent to the loop are 4 metres away and P11 is in the centre of the loop.

4.2 Survey site locations

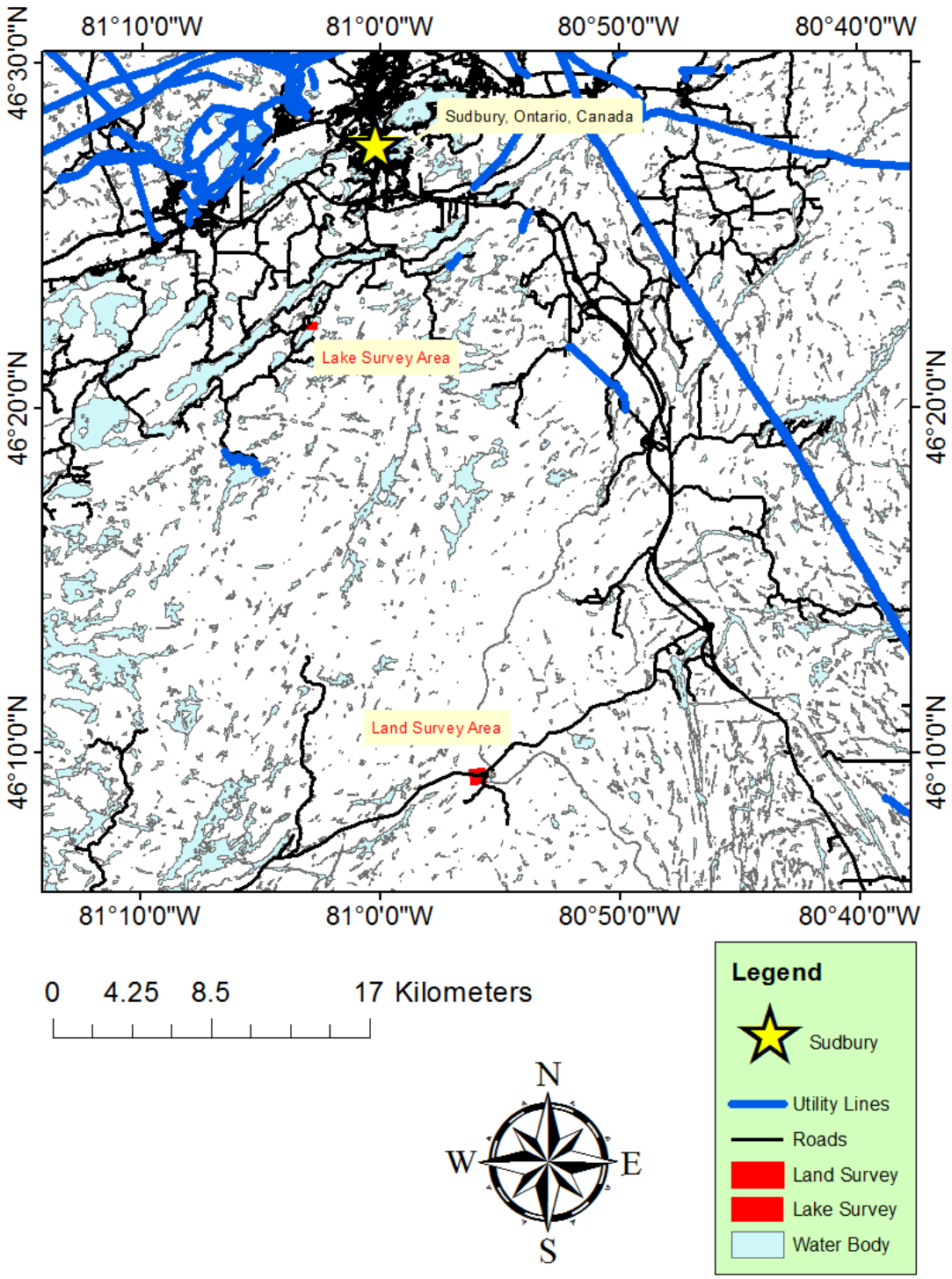

Figure 19: Geographical location of lake and land survey with respect to Sudbury, Ontario. Major power-lines are highlighted in blue along with roads and waterways. Most roads have a minor power-line running along them.

4.2.1 Lake survey

The lake survey was conducted on March 1, 2016 between 11:30 am and 1:30 pm with a temperature of around -20°C. It was located on Clearwater lake, approximately 12 km south of Sudbury, Ontario. The geographical coordinates are: 46°22'22.23"N 81°2'51.39"W. On March 17, 2017, the International Geomagnetic Reference Field (Thébault et al., 2015) indicates that the inclination is ∼71.75° and the declination is ∼10.08° W. The magnetic field strength was measured using a GSM-19T proton magnetometer as being between 55135-55162 nT, which gives a Larmor frequency range of 2347.6-2348.8 Hz. The region of the lake used for the survey had a depth of 15 metres (Appendix C) and an ice thickness of approximately 0.4-0.7 metres, which was determined from drilling holes into the ice at various points (needed for safety). Cultural electromagnetic sources were the gas-powered generator powering the electronics and the many houses and power-lines surrounding Clearwater lake.

4.2.2 Land survey

The land survey was conducted on April 27, 2016 between 12:00 pm and 2:30 pm with a temperature of 14°C. It was located on a gravel pit adjacent to Highway 637, approximately 33 km south of Sudbury, Ontario. The geographical coordinates are: 46°9'21.64"W 80°55'49.08"W. The magnetic inclination is ∼71.75° and the declination is ∼10.06° W. The magnetic field strength was measured as 54999-55114 nT which gives a Larmor frequency range of 2341.3-2346.2 Hz. Due to the low number of houses and power-lines in the area, there were minimal electromagnetic sources evident in the recorded data. The main noise disturbances were from local traffic and the gas-powered generator.

4.3 Preliminary hypotheses

4.3.1 Geometrical interpretation

The motivation to align the loop with magnetic north was to exploit the orientation of magnetization vectors in equilibrium. We can assume that prior to energising the freshwater in the ice-covered lake, it was only exposed to the local ambient magnetic field (i.e., the Earth's field). The orientation of the magnetization vectors, representing ensembles of water molecules, would then be aligned in the direction of the Earth's field. The lake survey area had a magnetic inclination of ∼71.75° and the declination of ∼10.08° W; the geometric interpretation of inclination and declination are outlined in Figure 20. The equilibrium positions of the magnetization vectors would be aligned ∼71.75° below the horizontal.

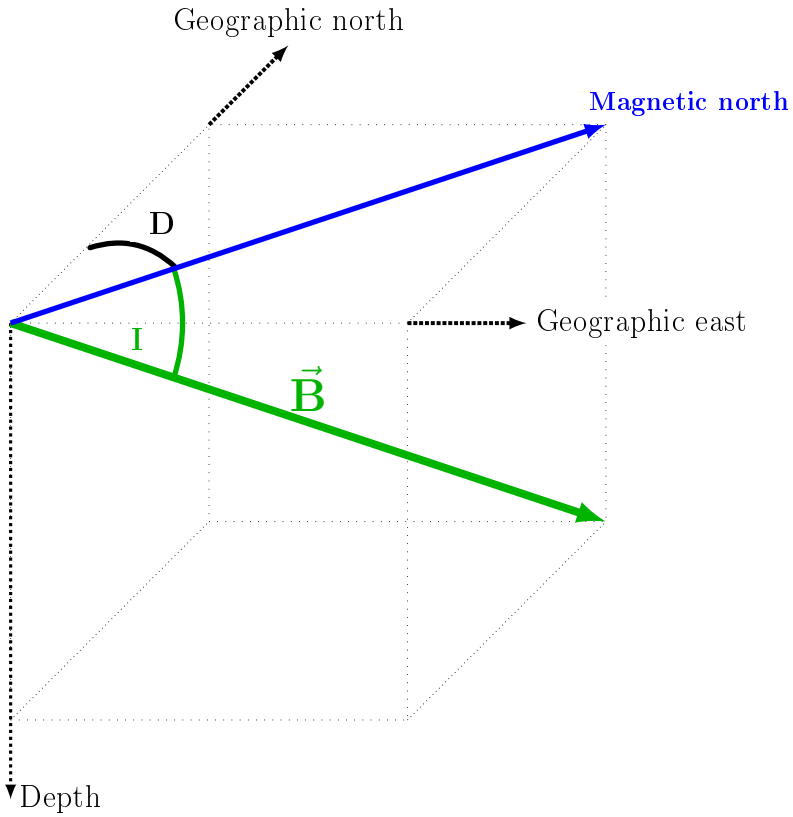

Figure 20: The relationship between the magnetic field vector and the two angles: declination (**D**) and inclination (**I**). The declination is the angle between geographic north and the magnetic north direction, which is the horizontal component of the magnetic field. The inclination is the angle between the horizontal projection of magnetic north and the magnetic field vector.

A representation of the magnetization vectors in equilibrium of the water molecules below the loop for line 1, is shown below in Figure 21. The magnetic field (normalized vectors) produced by the loop (for line 1 and 2) in the survey is shown in Figure 22 and the total magnetic field strength ($B_{\text{tot}} = \sqrt{B_x^2 + B_y^2 + B_z^2}$) is shown in Figure 23.

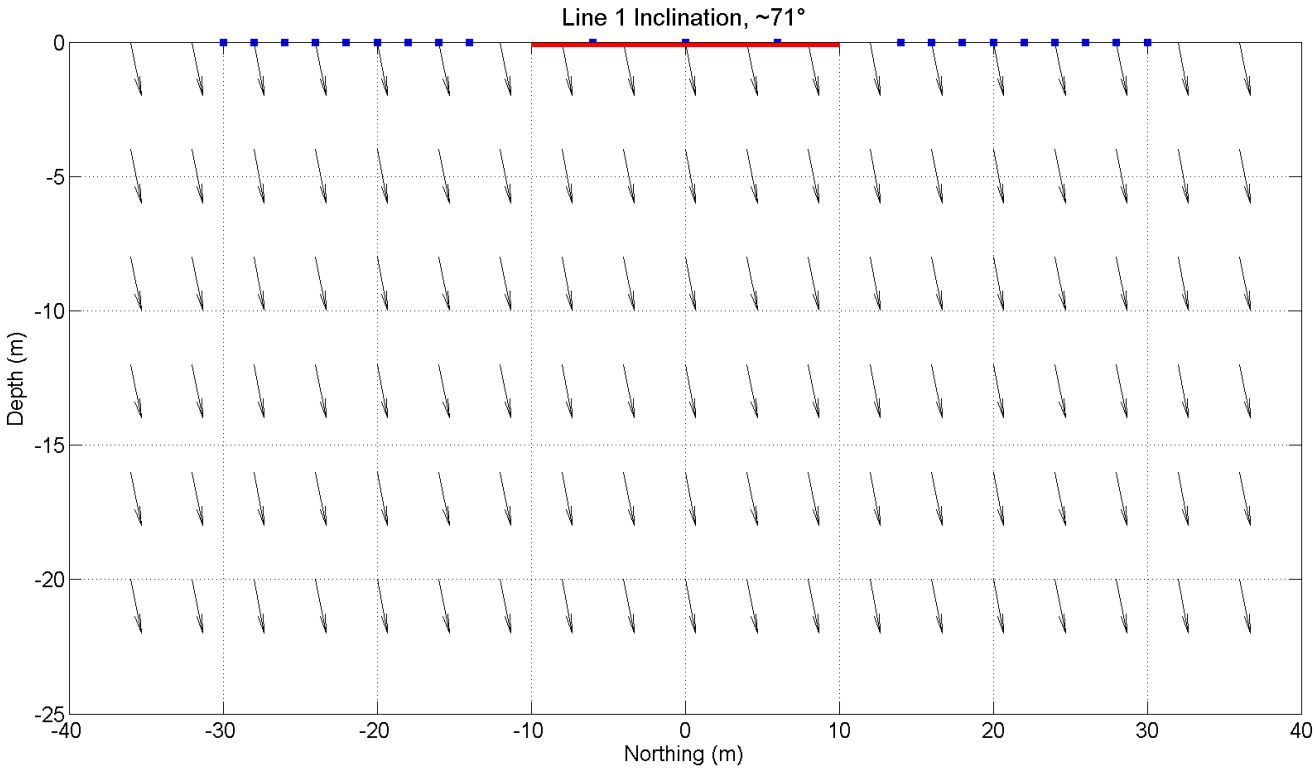

Figure 21: A cross-section view of the location of magnetization vectors in equilibrium in the lake survey for line 1. The magnetization vectors will be aligned with the local ambient magnetic field, which is 71° below the horizontal. The receiver box positions are symbolized with blue squares, with the loop in red.

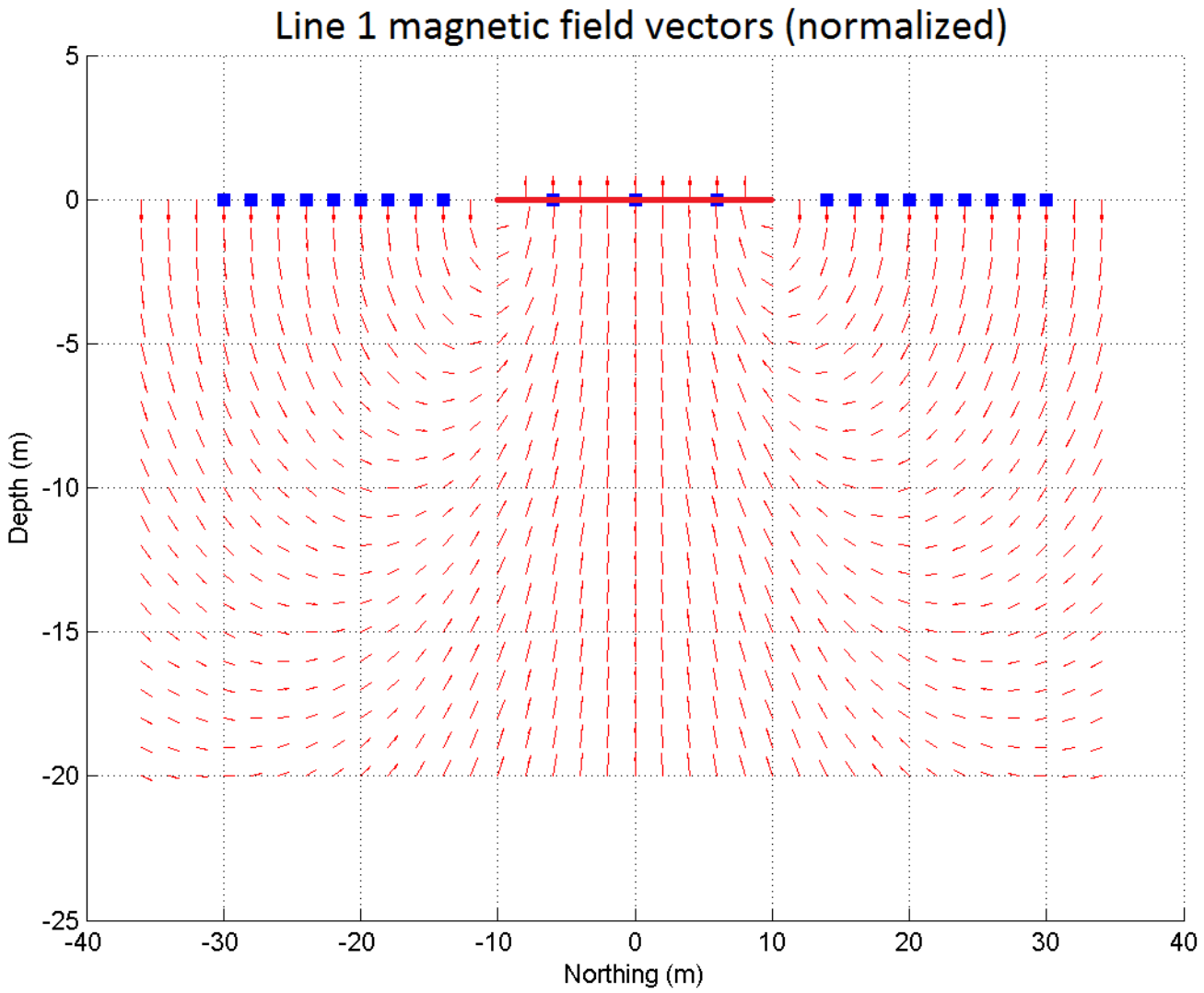

Figure 22: A cross-section view of the magnetic field vectors (normalized) created by the transmitting loop. The magnetic field strength produced by the loop is the same for line 1 and 2 (i.e., the title could say, "Line 2 magnetic field vectors (normalized)", and the plot remain the same). The receiver box positions are symbolized with blue squares, with the loop in red. The magnitude of the field produced by the loop is shown below in Figure 23.

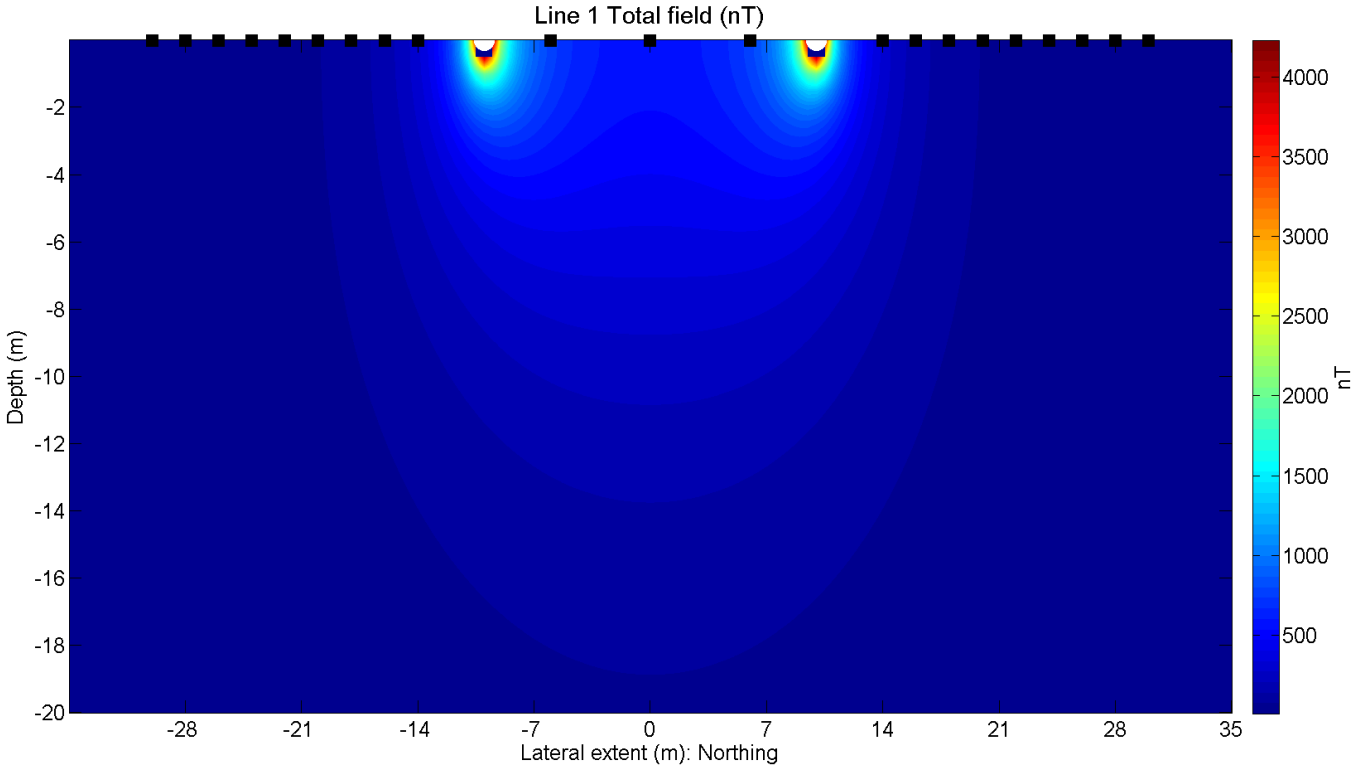

Figure 23: A cross-section view of the magnetic field created by the transmitting loop. The maximum magnetic field strength (dark red) is around 5100 nT and the lowest magnetic field strength (dark blue) is around 10 nT. The receiver boxes are symbolized with black squares and the loop position is symbolized by the two white circles (-10 m and +10 m in lateral extent and depth of 0 m).

The magnetic field produced by the transmitting loop will exert a torque on the magnetization vectors (which are representative of ensembles of water molecules) and cause them to rotate. This physical phenomenon is described by the Bloch equations (Equation 21). A large torque will cause a significant rotation of the magnetization vector (similar to Figure 9).

In order to calculate the torque (Equation 4), we will need to find the angle between the magnetization vectors (at equilibrium) and the magnetic field vectors from the loop (Figures 21 and 22, respectively). Once the angle is found, we can multiply the total field (Figure 23) by the sine of the angle.

We can apply the torque method to both lines in the survey to help get an understanding of where the maximal torque is being applied with respect to our receiver positions. Line 1 torque is shown in Figure 24 and the line 2 torque is shown in Figure 25. Both figures have the same color scheme; the dark blue represents $\sim 10^{-8}$ N·m and the dark red represents $\sim 10^{-5}$ N·m. The units are consistent with the magnetization vector and the total field strength (N·m = Am^2·nT).

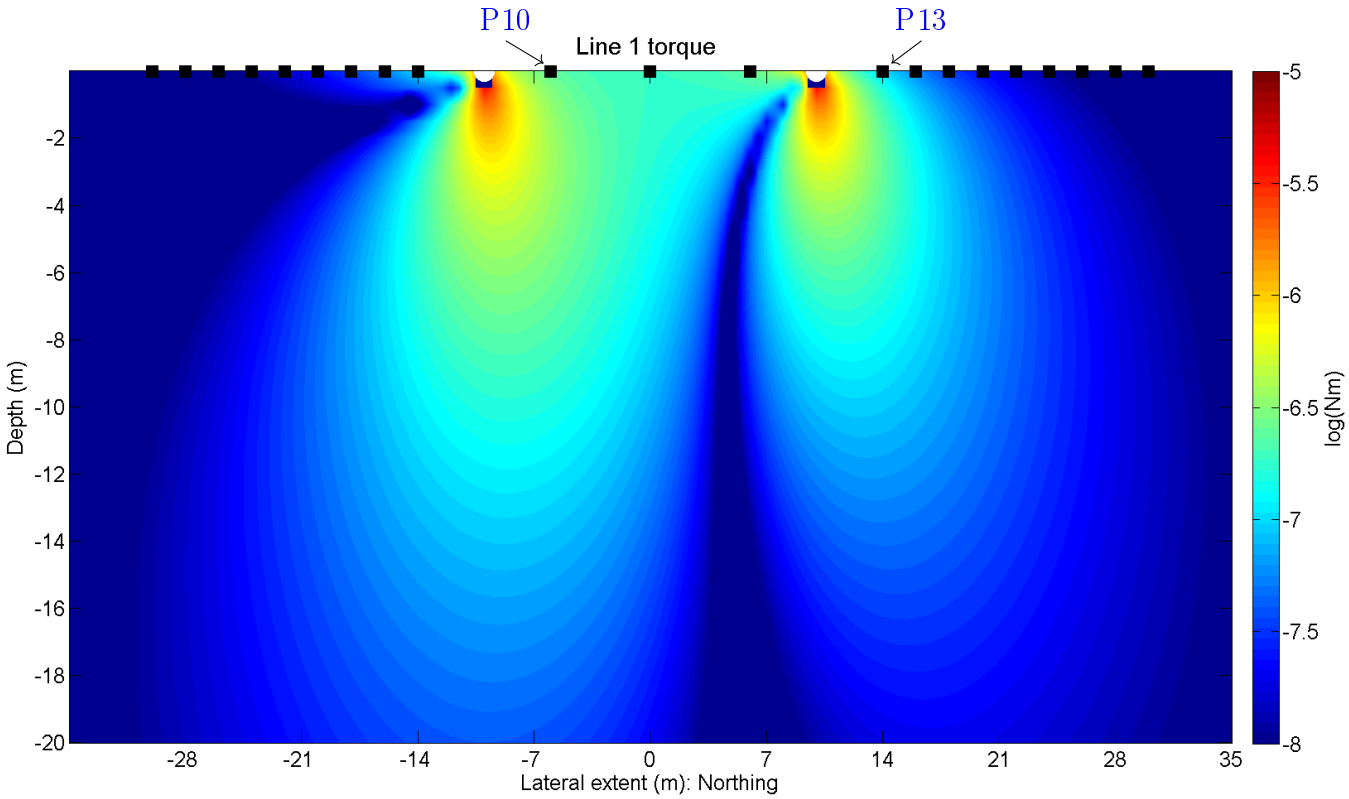

Figure 24: A cross-section view of the torque exerted on the magnetization vectors by the applied field for line 1 of the lake survey. Dark blue represents $\sim 10^{-8}$ N·m and the dark red represents $\sim 10^{-5}$ N·m. Receiver positions 10 and 13 have been explicitly labeled.

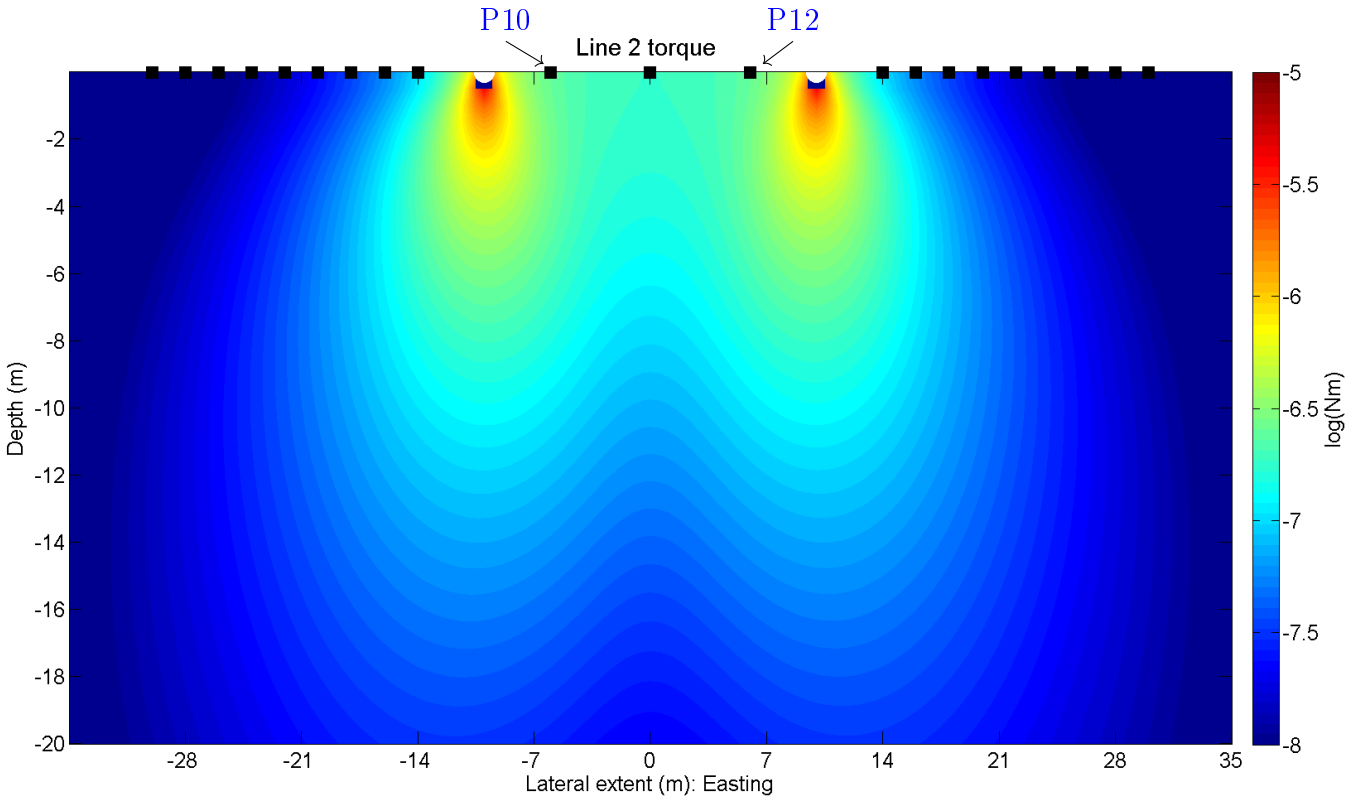

Figure 25: A cross-section view of the torque exerted on the magnetization vectors by the applied field for line 2 of the lake survey. Dark blue represents $\sim 10^{-8}$ N·m and the dark red represents $\sim 10^{-5}$ N·m. Receiver positions 10 and 12 have been explicitly labeled.

The main difference between Figures 24 and 25 is the asymmetry and symmetry (about the centre of the loop), respectively. The magnitudes of the torque are the same (both between 10^{-5} and 10^{-8} N·m). The asymmetry arises from the inclination in the geographic area and orientation of lines. Line 1 was aligned with magnetic north and so the equilibrium positions of the magnetization vectors (pointed 71° down from horizontal) had a variable angle between themselves and the applied field. In line 2 the angle between the magnetization vectors and the applied field were the same at all points (hence the torque distribution for line 2 being very similar to Figure 23).

Assuming that regions of larger torque correlate with larger NMR signals, then from

Figures 24 and 25, it would seem that the largest NMR signal should occur at receiver positions 10 and 13 for line 1 and receiver positions 10 and 12 for line 2.

4.3.2 NMR phenomenon

A cartoon depicting the phenomenon taking place during the frequency sweep is illustrated in Figure 26. The premise of using the frequency sweep was to record an NMR phenomenon from freshwater as the frequency passed the Larmor frequency. In older NMR experiments (undertaken in the 1950's), many experiments would sweep the frequency through the Larmor frequency, looking at the absorption of radio-frequency radiation versus frequency (Abragam, 1983).

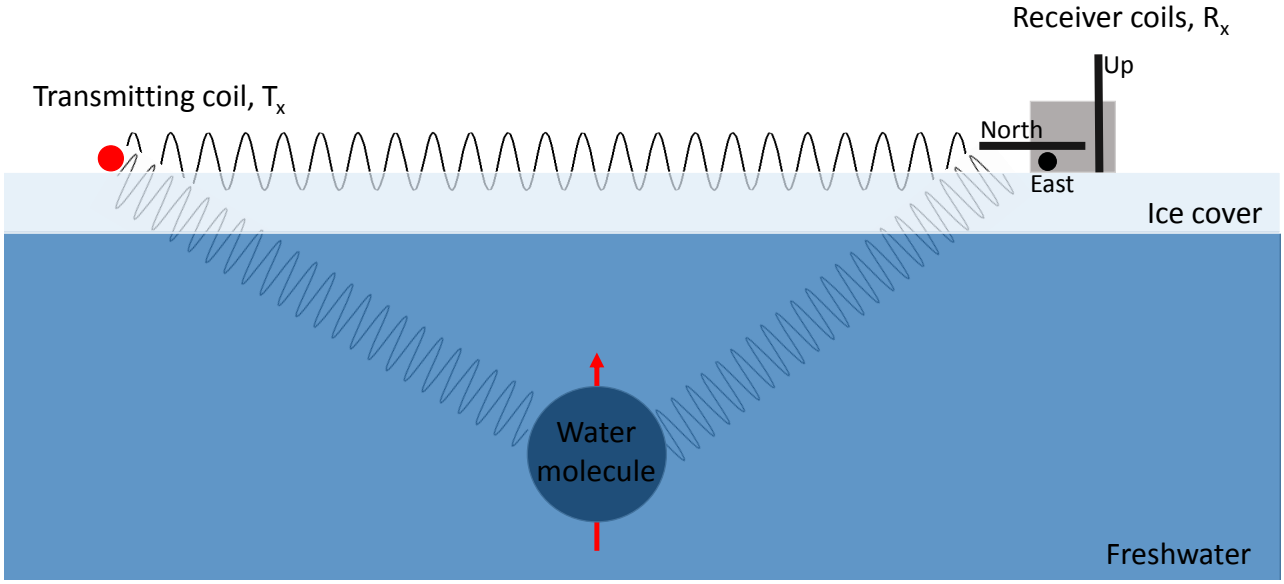

Figure 26: A cartoon of the theorized phenomenon occurring during transmitting. The transmitting loop will excite the water protons which will create a change in the signal measurable in the receiver coils.

The hypothesis is that as the frequency sweep crosses the Larmor frequency there will be a larger absorption of radio-frequency energy by the water molecules, which will then manifest as a phase shift in the receiver coils when compared to the transmitter. The analysis techniques will look at measuring the phase shift between the transmitted signal

(T_x) and the receiver coil signals (R_x).

Chapter 5

5 Results & Analysis

Data analysis is partitioned into two different categories, *on-time* and *off-time*. The *on-time* analysis involved analyzing the receiver coil data while the transmitting field was on and the *off-time* analysis was after the transmitting field had been terminated. The general work flow of the analysis is illustrated in Figure 27.

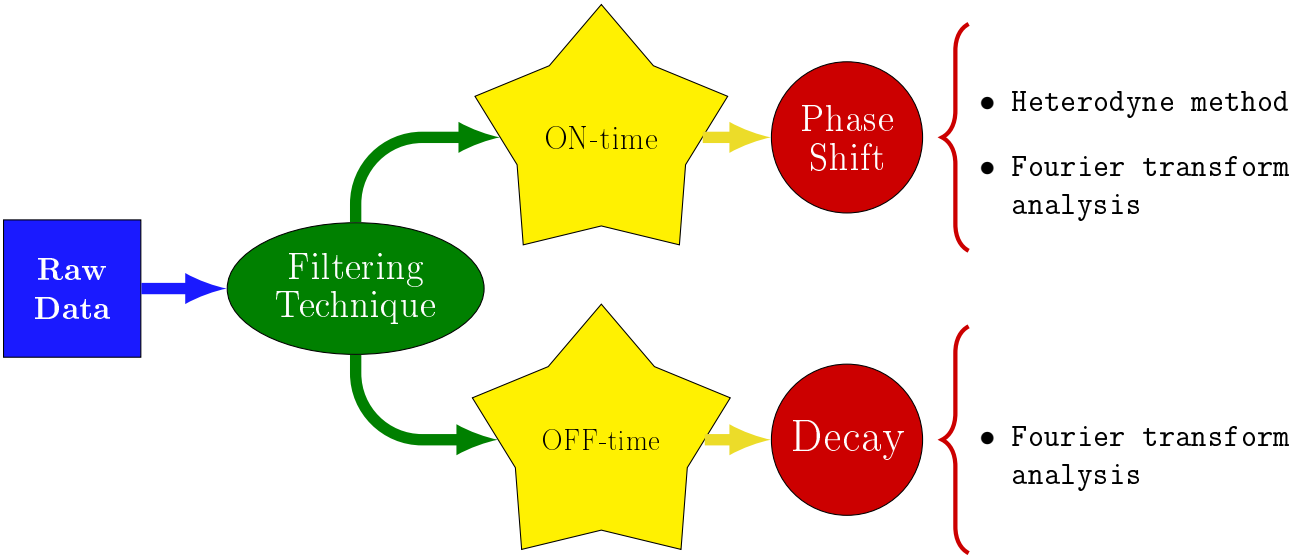

Figure 27: General scheme for data reduction, smoothing, and analysis. A more detailed explanation of "Filtering Technique" is below in Figure 31.

Originally, the analysis was only to be done for the on-time data, as discussed in section 4.3, but after manual inspection of the raw data, information in the off-time was noticed. Specifically in the lake data, a decaying oscillating waveform was noticed immediately after transmitter termination (TT). An example of the oscillatory decay, for the east coil magnetometer at position 12 of line 2 in the lake survey, is shown in Figure 28, where the black

line represents the current in the transmitting coil and the red line represents the magnetic field measured in the receiver coil. The transmitter termination is also highlighted with a vertical dotted blue line. The oscillatory decay does not exist in the land survey (i.e., the decay is exclusive to the lake survey).

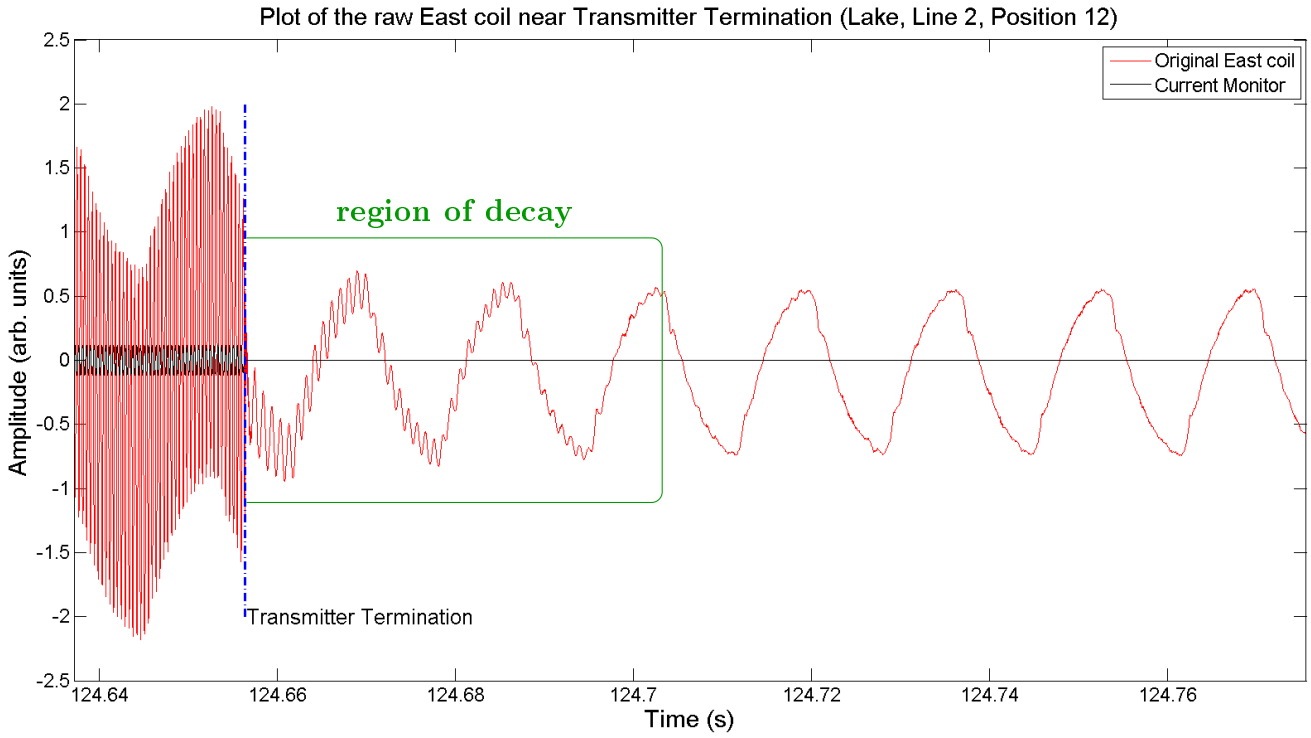

Figure 28: A distinct oscillatory decay is prominent in the raw lake data immediately after terminating the transmitting loop (encapsulated by green box). In this particular example, the length of the sweep is slightly longer than the intended 120 seconds; due to the signal generator operator allowing a few extra seconds. Also apparent is the distorted sinusoid associated with the power-line distribution frequency (60 Hz).

5.1 Data reduction

Before investigating the on-time or off-time data, data reduction was needed to reduce unwanted electromagnetic sources. A small section of the raw data is shown in Figure 29. Within the small section of raw data there are several sferics (high amplitude impulsive spikes) and the transmitted high-frequency signal used for the survey superimposed on top

of a 60 Hz signal. Sferics are essentially a series of noise pulses generated by distant lightning flashes (Grant and West, 1965). The low-frequency signal is approximately 60 Hz, which is attributed to local power-lines.

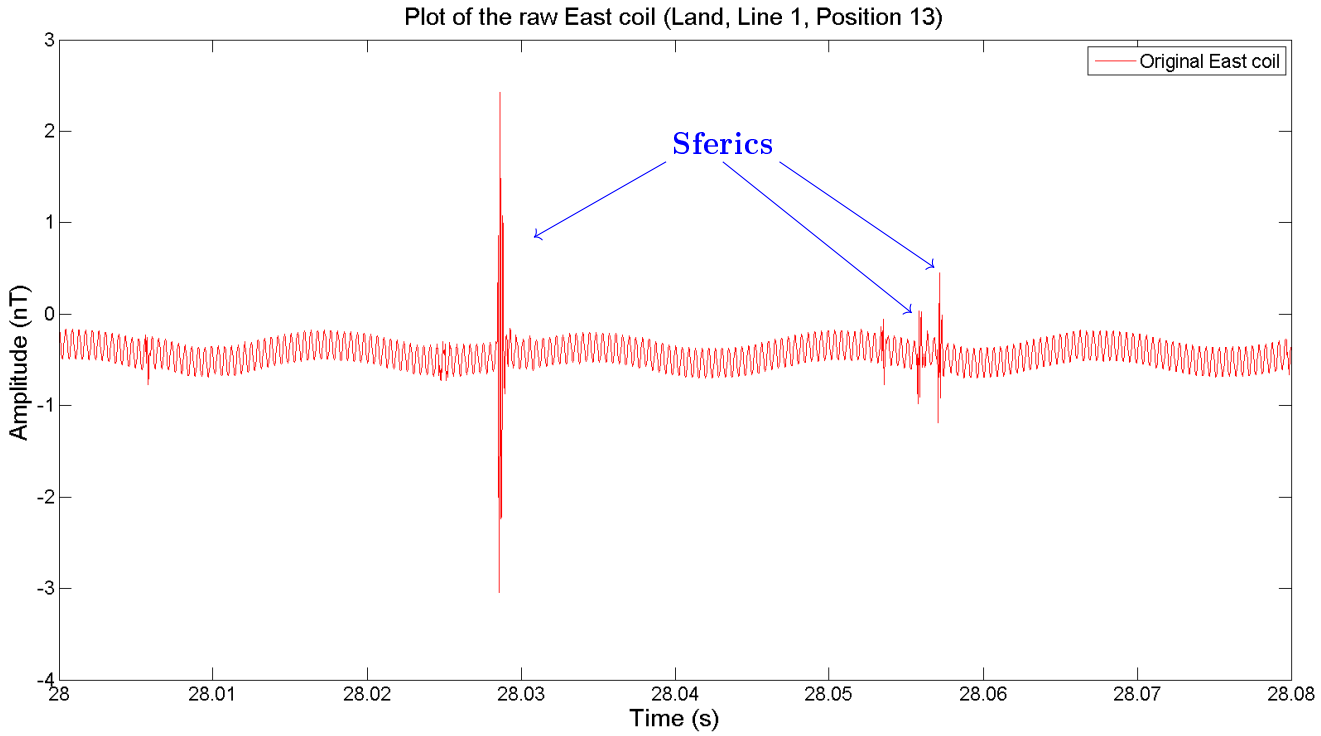

Figure 29: Approximately 0.1 seconds of raw data collected at the receiver position 13 on line 1 of the land survey. There are several high frequency sferics within the section. A high frequency signal (from transmitter) is superimposed on a 60 Hz signal.

The purpose of the data reduction scheme was to suppress the power-line and sferic contribution in the receiver coils. The power spectrum of the raw data collected at position 12 of line 2 in the lake survey is shown in Figure 30. The power-line frequency, its odd harmonics (first few have been pointed out), and the frequency sweep of the survey (2300-2400 Hz) are prominent in the power spectrum. The data reduction scheme attempts to remove the 60 Hz and higher harmonics from the receiver coil data as best as possible.

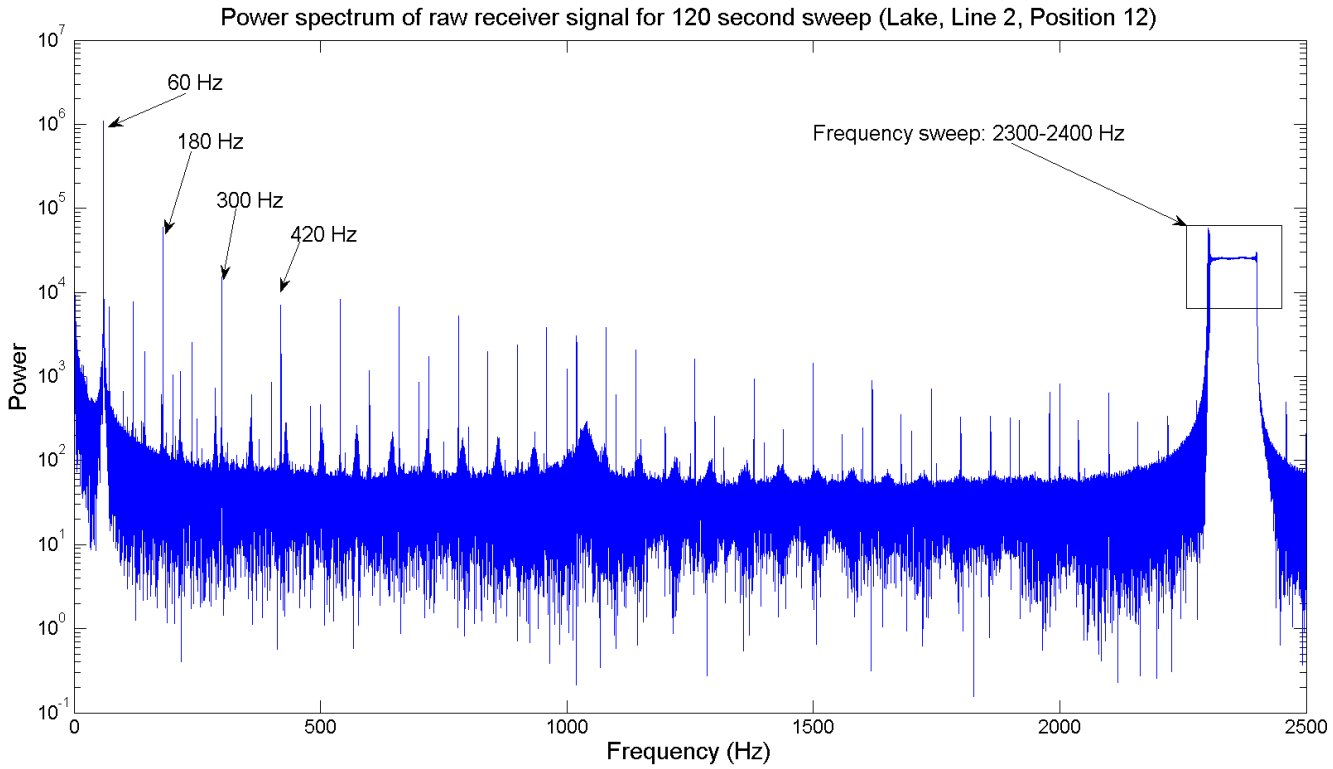

Figure 30: The power spectrum of the raw collected data (120 second sweep) for the east coil for position 12 of line 2 in the lake data. The 60 Hz peak and the first few odd harmonics are pointed out. The frequency sweep is also shown, 2300-2400 Hz.

Several methods were tested to filter out the high frequency sferics as well as the 60 Hz signal from the data which included different low-pass filters (butterworth, chebyshev, elliptical, etc.), band-pass filters, high-pass filters, and envelope techniques, but the most resilient method is outlined below (Section 5.1.1). The early tests using filters worked well, but the frequencies to be rejected (e.g., 60*n, where $n = 1, 2, 3, 4, 5, ...$) potentially contained information relevant to a possible NMR signal in the range 2300 to 2400 Hz. Instead of rejecting all the harmonics individually, the power-line signal (including all its harmonics) was estimated and then subtracted from the original raw waveform.

5.1.1 Filtering technique

The filtering technique used to estimate the power-line signal is outlined in Figure 31. Removing the 60 Hz wave from the raw waveform will be beneficial for analysis since the on-time heterodyne method requires a near-constant amplitude, as will be explained below.

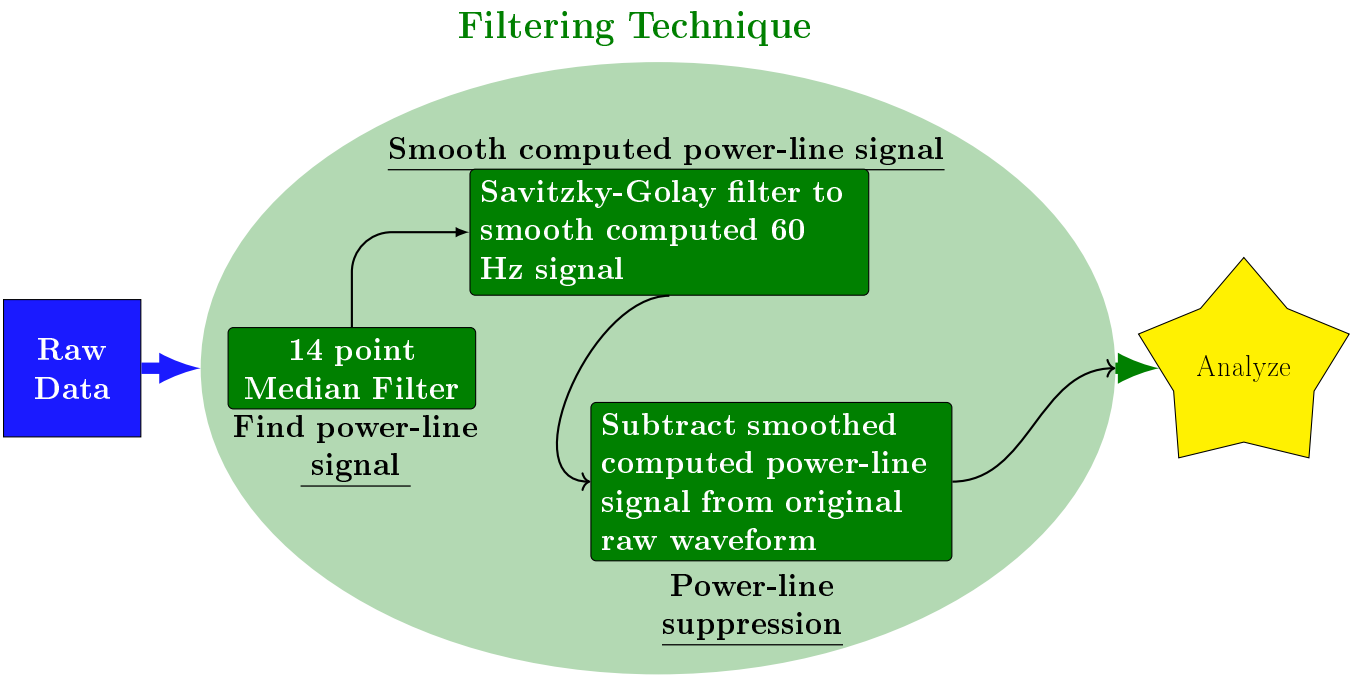

Figure 31: The filtering technique used on the raw data. The process includes three steps which help to remove the power-line signal from the raw data. Once the data were filtered, analysis began.

The following steps (based on Figure 31) will outline, in more detail, how the filtering technique works using the raw waveform from the east receiver coil for position 12 of line 2 in the lake survey as an example:

Step 1. Apply a median filter with block size of 14 points to the raw waveform which is then smoothed with Savitzky-Golay filter to find the power-line signal (black line in Figure 32). The block size of 14 was chosen because one full cycle of a 2300-2400 Hz wave has approximately 14 points when the sampling frequency is 31250 Hz ($31250/2300 \approx 14$).

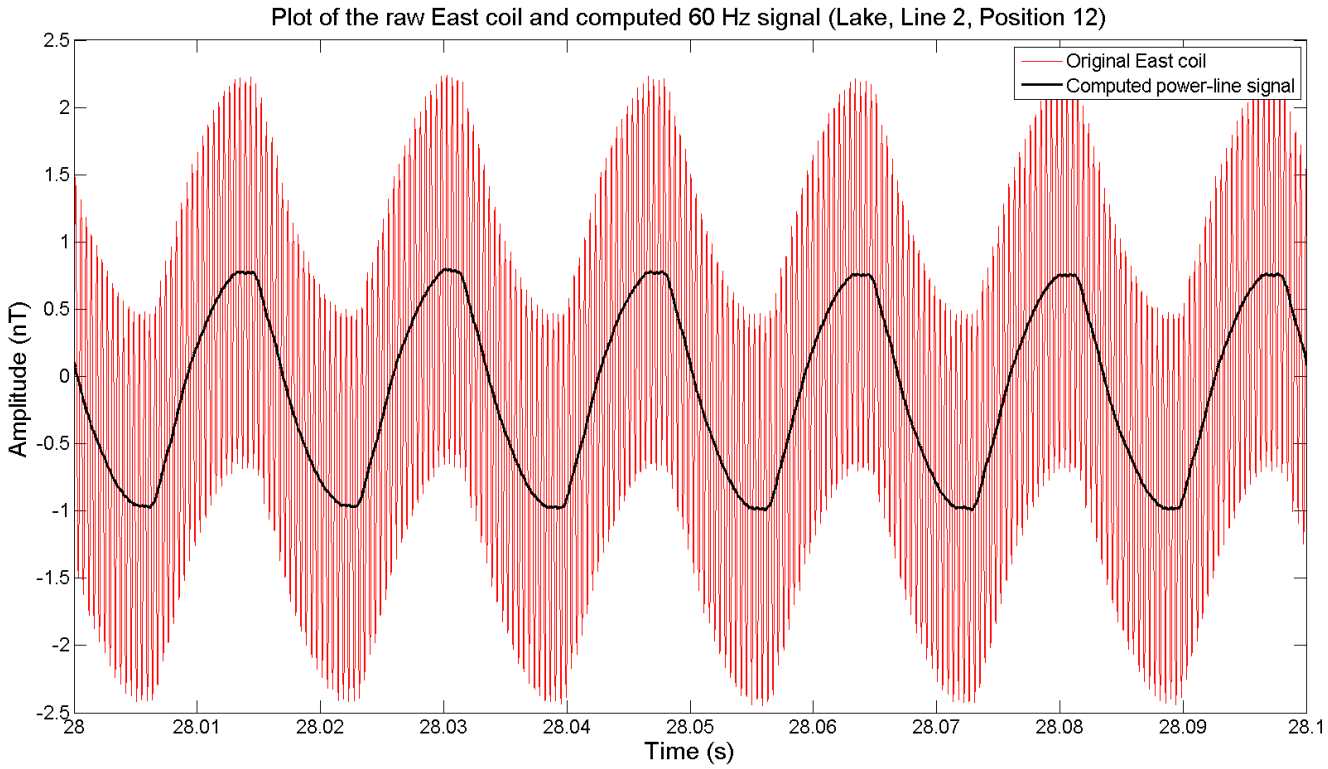

Figure 32: The smoothed computed 60 Hz signal (in black) placed over the original raw waveform (in red).

Step 2. Subtract the newly found power-line signal from the original to get a *reduced* waveform (Figure 33). The subtraction of the computed power-line signal allows us to look at the 2300-2400 Hz wave in the receiver coil.

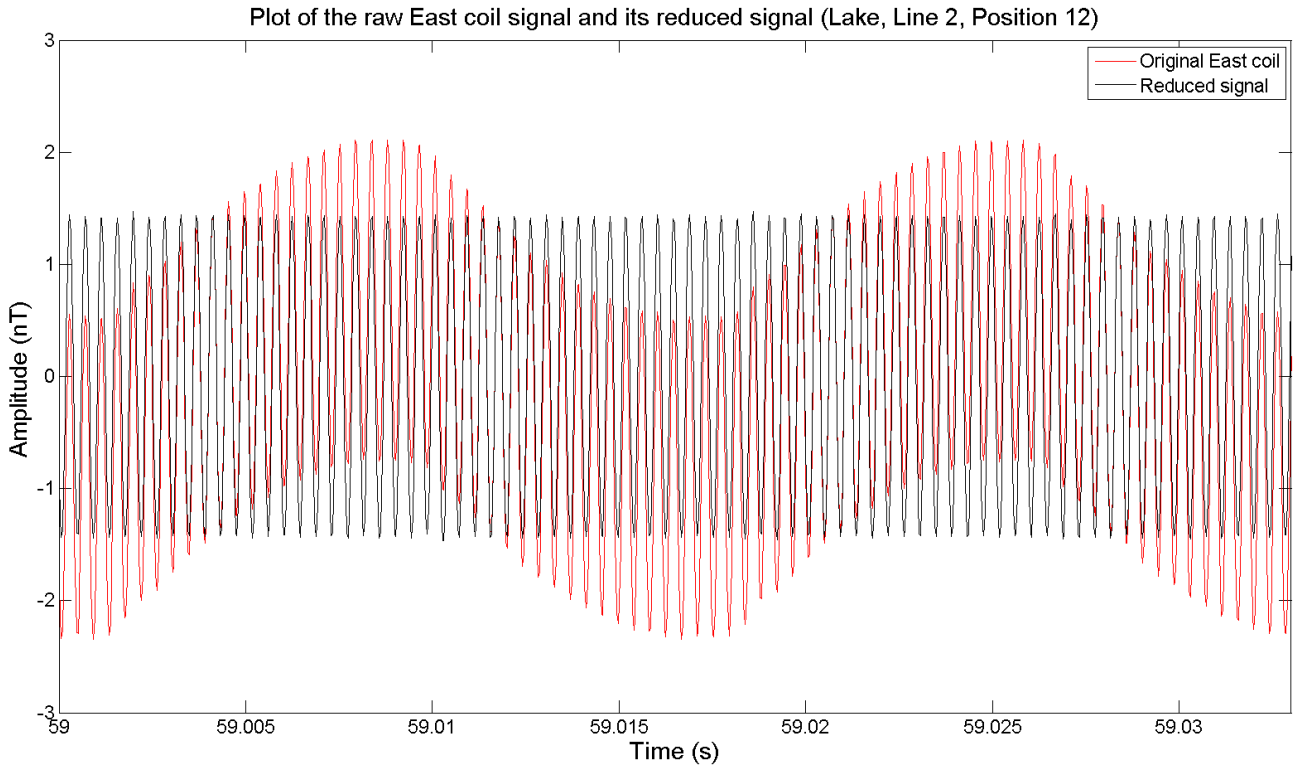

Figure 33: The new reduced waveform (in black) and the original raw waveform (in red).

The power spectrum comparing the raw receiver coil data and the newly reduced waveform is shown in Figure 34. The decrease in magnitude of the 60 Hz peak and its subsequent harmonics is evident. A narrower range of frequencies, specifically near 60 Hz, is shown in Figure 35. Although the 60 Hz component in the power spectrum was not completely reduced to zero, it has been suppressed by a factor of 1000, which is significant enough to allow for on-time analysis.

A trade-off between 60 Hz suppression and 2300-2400 Hz precision had to be made. Every iteration of a filtering operation would erase or add frequency components due to algorithm imperfections. For example, if more 60 Hz reduction schemes were introduced, then the power spectrum would have a reduced 60 Hz component, but it would also skew the 2300-2400 Hz band, which is unacceptable in this instance. The goal of the data reduction

technique was to minimize the power-line harmonics enough so as to produce a relatively flat amplitude in the 2300-2400 Hz band, which has been achieved.

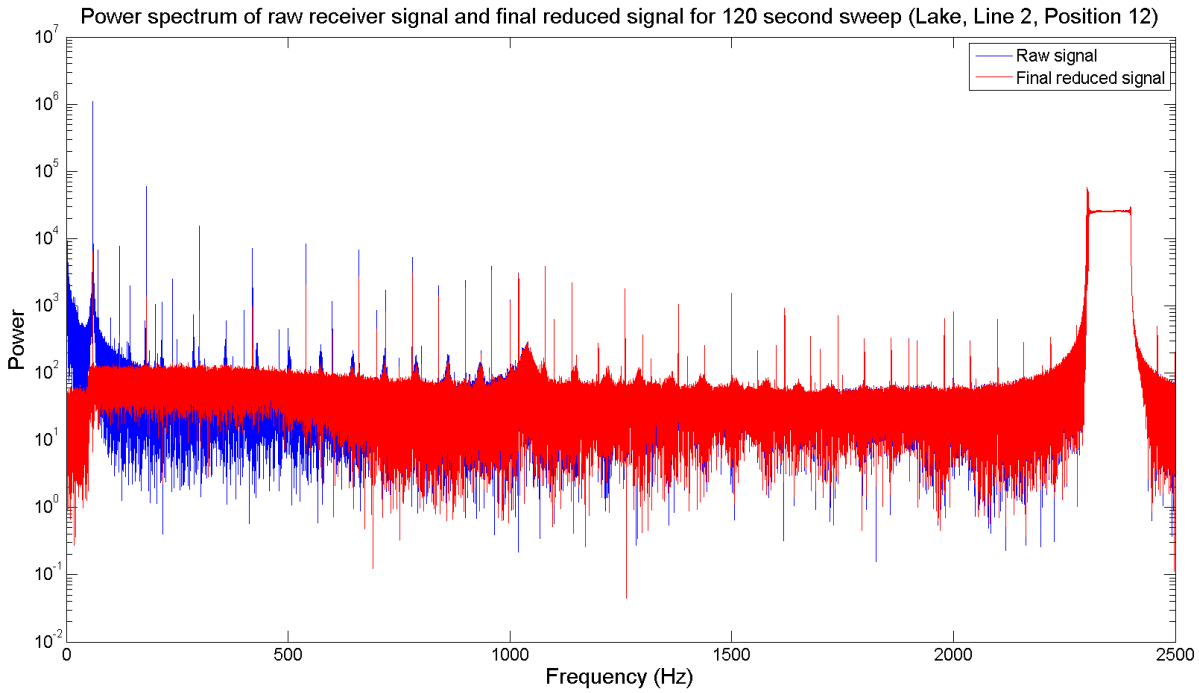

Figure 34: Power spectrum comparison between the raw receiver coil and the reduced wave (0-2500 Hz).

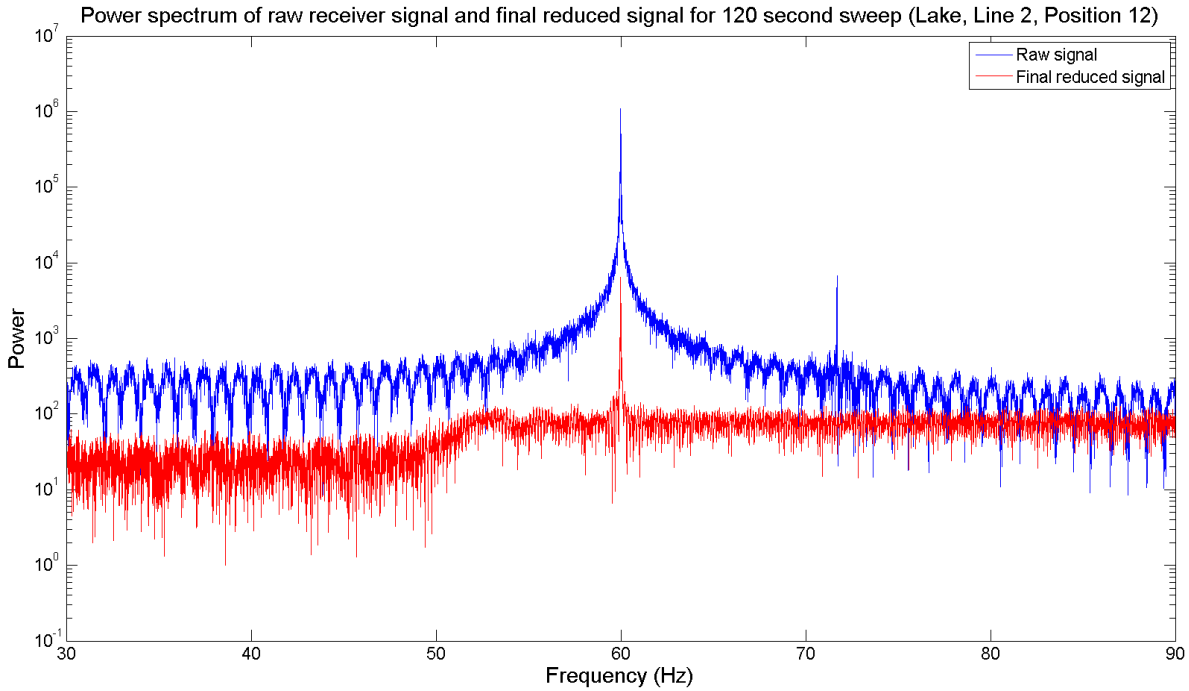

Figure 35: Power spectrum comparison between the raw receiver coil and the reduced wave (30-90 Hz).

5.2 On-time results

The on-time analysis was designed to measure a phase shift between the transmitter and the receiver coils, as explained in Section 4.3. Since the data recorders have synchronous timing through GPS, we are able to directly compare transmitter and receiver measurements. This means that the measurement at t_1 in the transmitter corresponds to the measurement at t_1 in the receiver coils; there is no lag.

5.2.1 Heterodyne method

The heterodyne method incorporates a trigonometric identity, to measure the phase difference between two oscillatory waveforms of the same constant frequency. In the case of the frequency sweep, this method is still valid since the transmitting loop waveform and the

receiver coil waveform will have the same frequency at each instant of time.

5.2.1.1 Theory

The heterodyne method is based on the product-to-sum trigonometric identity,

$$\sin u \sin v = \frac{1}{2}[\cos(u - v) - \cos(u + v)]. \tag{46}$$

With respect to the completed survey, the current monitor waveform and the receiver waveforms will be compared. The lake survey was not able to collect the up-coil data due to a faulty connection, so only north-coil and east-coil data were used in the heterodyne analysis.

Letting y_1 represent the current monitor waveform and y_2 the receiver coil (either east or north) waveform, we assume that both waveforms are sinusoids with frequency, ω, which will correspond to the frequency generated from the transmitting loop (2300-2400 Hz).
The two waveforms are,

$$y_1 = A\sin(\omega t),$$
$$y_2 = B\sin(\omega t + \phi(t)).$$

The $\phi(t)$ in y_2 represents the phase shift with respect to time. The phase shift is time-dependent in this case since the survey involves a sweep and the assumption is that there will be a greater change in the phase shift at a certain frequency (i.e., the Larmor frequency). It could be that both waveforms are in-phase with each other, which means that $\phi = 0$, but for the remainder of the algebra it is assumed that $\phi \neq 0$. For the following algebra, we simplify the notation to, $\phi(t) = \tilde{\phi}$.

Multiplying the two waveforms (y_1 and y_2) results in,

$$y_1 \cdot y_2 = AB\sin(\omega t)\sin(\omega t + \tilde{\phi}). \tag{47}$$

We can use Equation 46 to manipulate Equation 47,

$$\begin{aligned} AB\sin(\omega t)\sin(\omega t+\tilde{\phi}) &= \frac{AB}{2}[\cos(\omega t-\omega t-\tilde{\phi})-\cos(\omega t+\omega t+\tilde{\phi})], \\ &= \frac{AB}{2}[\cos(-\tilde{\phi})-\cos(2\omega t+\tilde{\phi})]. \end{aligned} \tag{48}$$

At this point, a low-pass filter can be applied to separate the constant (non-oscillatory) term from the second term that oscillates at a higher frequency, $\cos(2\omega t+\tilde{\phi})$. After applying a low-pass filter to Equation 48,

$$y_1 \cdot y_2 = \frac{AB}{2}\cos(\tilde{\phi}),$$

which can be rearranged to solve for the phase shift,

$$\begin{aligned} \cos(\tilde{\phi}) &= \frac{2}{AB}(y_1 \cdot y_2), \\ \tilde{\phi} &= \cos^{-1}\left(\frac{2}{AB}(y_1 \cdot y_2)\right). \end{aligned} \tag{49}$$

Equation 49 says that if there is no phase shift (or a constant phase shift) between the two waveforms then, by performing the multiplication and low-pass filter procedure, the result will be a constant value (i.e., a horizontal line). When the phase changes, there will be some non-horizontal feature, such as a step-like function, a peak, or a gradual curve; depending on the nature of the phase shift.

The significance of the data reduction scheme emerges in Equation 49, because the largest error in $\tilde{\phi}$ will come from the amplitude error (ΔA and ΔB) of the two multiplied waves. The original raw signal (red line in Figure 32) is effectively a large 60 Hz sinusoid with a high frequency wave (2300-2400 Hz) superimposed on top. By using the heterodyne method, the percentage error in A and B (ΔA and ΔB, respectively) will be much less since the new reduced waveform no longer has the 60 Hz component. The reduced waveform only contains the high frequency wave allowing for measurement of more subtle changes in the phase shift

between y_1 and y_2.

5.2.1.2 Application to field data

In our case, we will be comparing the phase shift between the current monitor wave (y_{CM}) and both the east and north receiver coil waveforms (y_E and y_N). The current monitor wave, y_{CM}, represents the current passing through the transmitting coil and will have units of Amperes. The receiver coil waveforms, y_E and y_N, represent the magnetic field strength recorded in either the north or east direction and will have units of nanoteslas. Since the heterodyne method is only concerned with the phase shift between the transmitter and the receivers, the units of the waves are not important, only their phase is.

Implementing the heterodyne method numerically follows the steps outlined in Section 5.2.1.1 with some minor alterations. The general process, outlined using y_{CM} and y_E, is summarized in the following steps:

1. Apply the power-line signal removal to the raw receiver coil data, y_E (∼120-second long sweep). The current monitor is not corrupted from secondary electromagnetic sources, so it does not need reduction.

2. Multiply the current monitor waveform by the reduced receiver waveform, $y_{CM} \cdot y_E$. Both y_{CM} and y_E are ∼120-second long time series, which requires $y_{CM} \cdot y_E$ to also be ∼120 seconds long ($\texttt{length}(y_{CM}) = \texttt{length}(y_E) = \texttt{length}(y_{CM} \cdot y_E)$).

3. Apply a first-order low-pass Butterworth filter with a cut-off frequency of 20 Hz. If we set $y_{CME} = y_{CM} \cdot y_E$ then we are left with,

$$y_{CME} = \frac{AB}{2}\cos(\phi). \tag{50}$$

The resulting wave, y_{CME}, contains the phase shift information, $\cos(\phi)$, along with the amplitudes of the original waves, A and B. Even with the suppression of the 60 Hz wave, there is still a slight amplitude variation over the entire 120-second long sweep.

4. In order to find the phase shift, ϕ, we must normalize y_{CME} using the amplitudes from the two waves, y_{CM} and y_E. Instead of finding an average amplitude for both y_{CM} (A) and y_E (B) over the entire 120 second long sweep, it was broken into smaller 0.1 second long sections and then evaluated. By using 0.1 second long sections, the amplitude variance in both segments was smaller.

   For instance, in the 120-second long sweep, there would have been a total of approximately 276000-288000 cycles of the 2300-2400 Hz wave, resulting in a larger variation in the amplitude values (A and B) of those cycles. By decreasing the time section to 0.1 seconds, there is about 230-240 cycles of the 2300-2400 Hz wave, which results in a smaller variance in the amplitude values (A and B) when compared to the 120-second long sweep.

5. After normalizing the 120-second long y_{CME} with the amplitudes estimated from the 0.1 second sections, we are left with the phase shift between the two waveforms, y_{CM} and y_E, as a function of time.

The 5 steps are used to compare the phase shift between y_{CM} and the receiver coils, y_E and y_N, for both lines of both surveys. The comparison between the lake survey and the land survey for line 2, position 12 is shown in Figures 36 and 37. The phase shift over the sweep, for the lake survey, does not seem to give any indication of a distinct contrast at or near the Larmor frequency in Figure 36, which leads to assume that no definitive signal from the freshwater is discernible. Similarly, for the land survey (Figure 37), there is no distinct pattern, other than a general negative linear trend for the east coil and positive linear trend for the north coil.

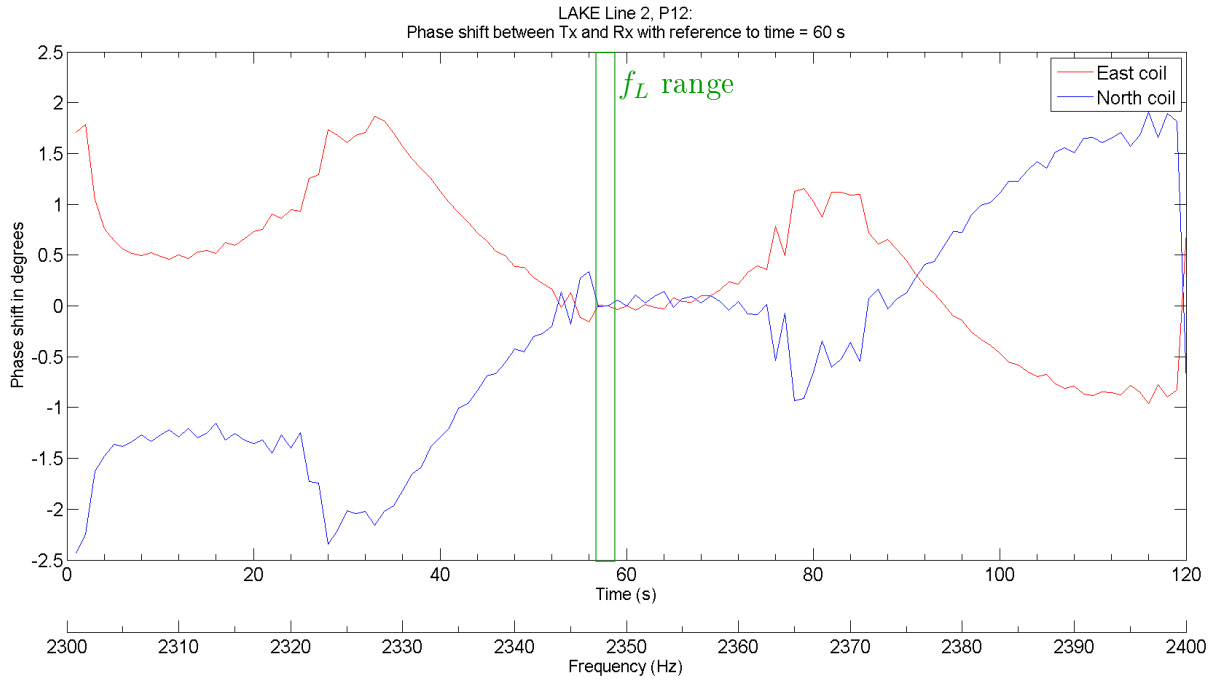

Figure 36: Heterodyne method applied to y_E and y_N for the lake survey, line 2, position 12. The Larmor frequency range is 2347.6-2348.8 Hz (green vertical lines on plot).

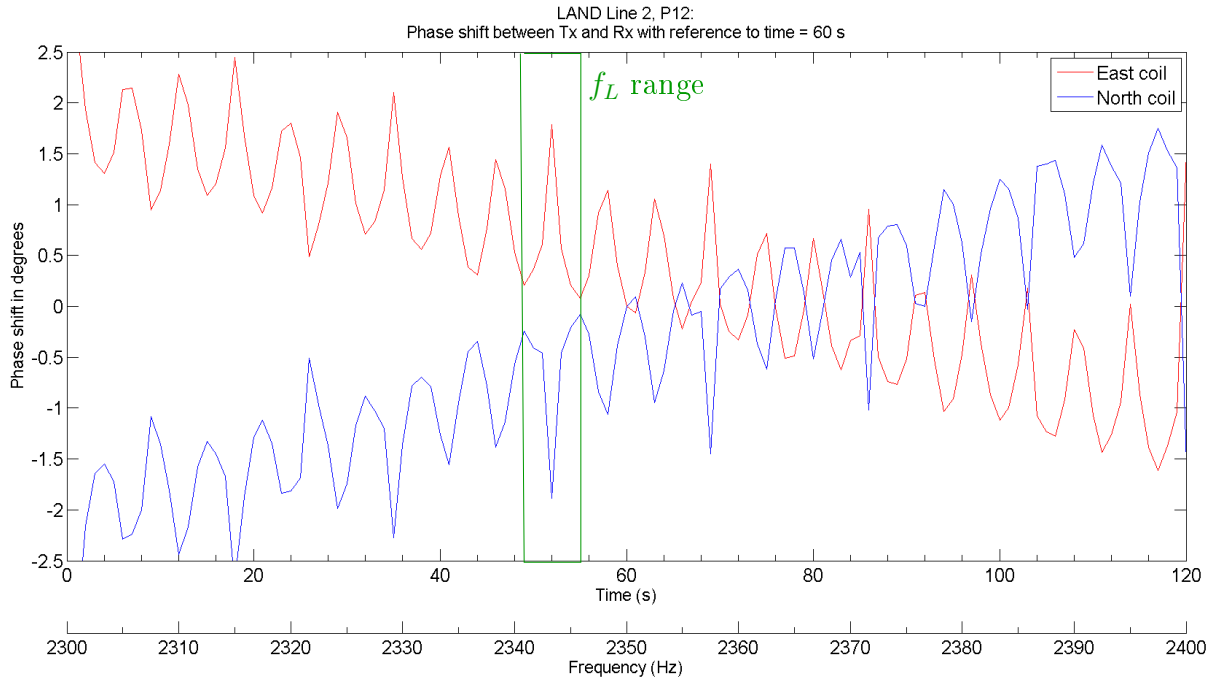

Figure 37: Heterodyne method applied to y_E and y_N for the land survey, line 2, position 12. The Larmor frequency range is 2343.1-2346.2 Hz.

Various combinations of the heterodyne method were incorporated to give an average result over the sweep time (not shown), although they were not successful. Several filtering techniques and methods were applied in an attempt to exploit the phase relationship between the transmitted signal and received signal, but no permutation produced any convincing evidence for a phase shift due to an NMR signal at the Larmor frequency. The example shown in Figures 36 and 37 used receiver positions that had a large on-time amplitude signal, with the purpose being that a large on-time signal would be less noisy and better for the heterodyne method. In essence, the heterodyne method did not show any indication of an absorption at the Larmor frequency that manifested as a phase shift. The modeling shown in the next section describes why this is believed to have occurred.

5.2.2 Fourier transform analysis

Since the NMR signal is an oscillatory decay in the time-domain, a Fourier transform (FT) would calculate the frequency components of the signal, in the frequency-domain. FT methods were the first avenue of analysis attempted, but were not able to locate any components at the Larmor frequency. The lake survey had a Larmor frequency between 2347.6-2348.8 Hz which was 8 Hz away from the power-line harmonic, 2340 Hz. The NMR signal is inherently small, so monitoring small changes in either the phase or the amplitude (not caused by the transmitting loop) in the receiver signal, is exceptionally difficult.

A comparison between the transmitted signal (y_{CM}) and the received signal (y_R) using the Fourier transform method included: deconvolution, in-phase and quadrature response, and phase angle between y_{CM} and y_R. The purpose being to compare and contrast any significant differences between the two, particularly near the Larmor frequency. These Fourier transform methods showed no conclusive evidence of an existing NMR signal, albeit the techniques work in theory; it is entirely possible that the NMR signal that was excited by the adiabatic sweep used was simply not above the ambient noise level and effectively masked,

making it undetectable.

Based on modeling of the magnetization vector, the power spectrum (magnitude of the Fourier transform) was then applied to two sections of the sweep: early-time (t = 0-10 seconds) and late-time, 5 seconds before TT. The early-time section attempted to exploit the initial perturbation of the magnetization vector, but there were no significant differences between the power spectrum of the lake and land signals. During the last several seconds of the sweep, there were some instances where the transmitted frequency would switch from 2400 to 2300 Hz (explained in Section 5.3), so the magnetization vector would undergo complex dynamics, which were modeled. The frequency components of the complex dynamics were unable to be recorded.

A noticeable difference between the lake and land surveys occurs when the power spectrum of the entire sweep ($\sim$120 seconds) is calculated. An example power spectrum using the signal recorded from the east coil receiver at position 14 of line 2 of the lake survey is shown in Figure 38. In Figure 38, the noticeable features are the plateau-like feature between 2300 and 2400 Hz which is from the transmitted field, a bell-shaped feature near 1000 Hz, the 60 Hz harmonics, and several random spikes. The non-harmonic spikes are *random* because they tend to show up randomly in each of the power spectrums; not consistently. The bell-shaped feature is evident in the lake data (for most receiver positions), but not the land data. In Figure 38, the peak value (excluding power-line harmonics) within the bell-shaped function is 1045 Hz. For receiver positions where the bell-shaped feature was obvious, the non-harmonic peaks of the bell-shaped feature are summarized in Table 3. The bell-shaped features were only obvious in line 2 of the lake survey (both east and north coils).

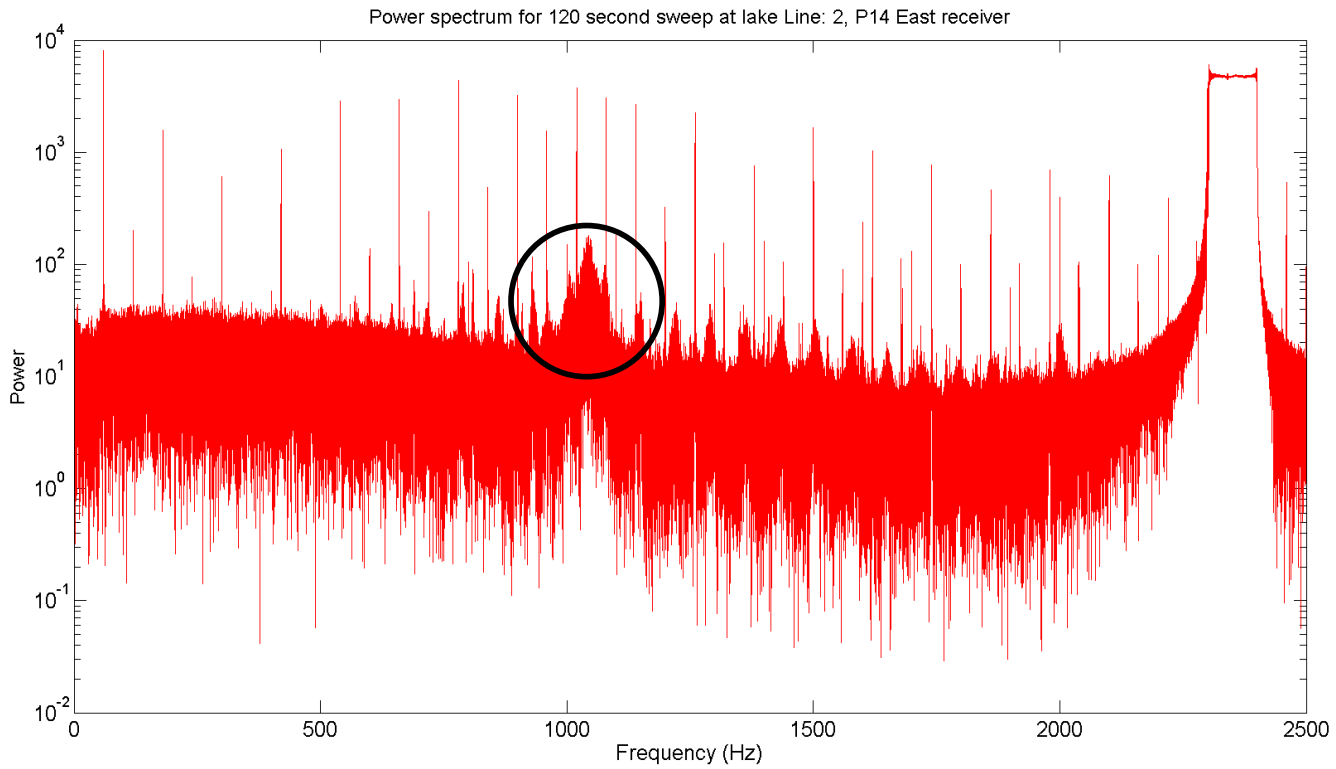

Figure 38: Power spectrum of full 120 sweep of east coil, lake, line 2, P14. Most of the spikes are from 60 Hz harmonics and the plateau feature on the right-hand side is from the transmitted field. A bell-shaped feature is also noticeable, outlined by the circle. The peak (excluding harmonics) within the circle is 1045 Hz.

All features in the power spectrum are explained, except for the bell-shaped feature centred on 1045 Hz. The power spectrum was performed on segments of the recorded signal outside of the sweep, when the loop was not transmitting, but while the gas-powered generator was still on and there was no bell-shaped feature present; only 60 Hz and its harmonics. An attempt to locate the 1045 Hz signal within the sweep, was completed by applying a band-pass filter for frequencies within the bell-shaped function (970-1060 Hz). The power spectrum in Figure 38 is for the entire 120-second long sweep. The resulting power spectrum is shown in Figure 39, where all frequencies except the bell-shaped feature, have been suppressed. The band-pass filtered signal is shown in Figure 40 for the full sweep. The amplitude is fairly constant, except for the last few seconds of the sweep where it is erratic

(exclusive to P12, not evident in others). A 0.1-second long segment of the band-pass filtered signal is shown in Figure 41. The band-pass filtered signal resembles a 1045 Hz wave modulated with a lower frequency waveform. The 1045 Hz was apparent throughout the entire sweep (i.e., no specific times where the 1045 Hz signal was strongest).

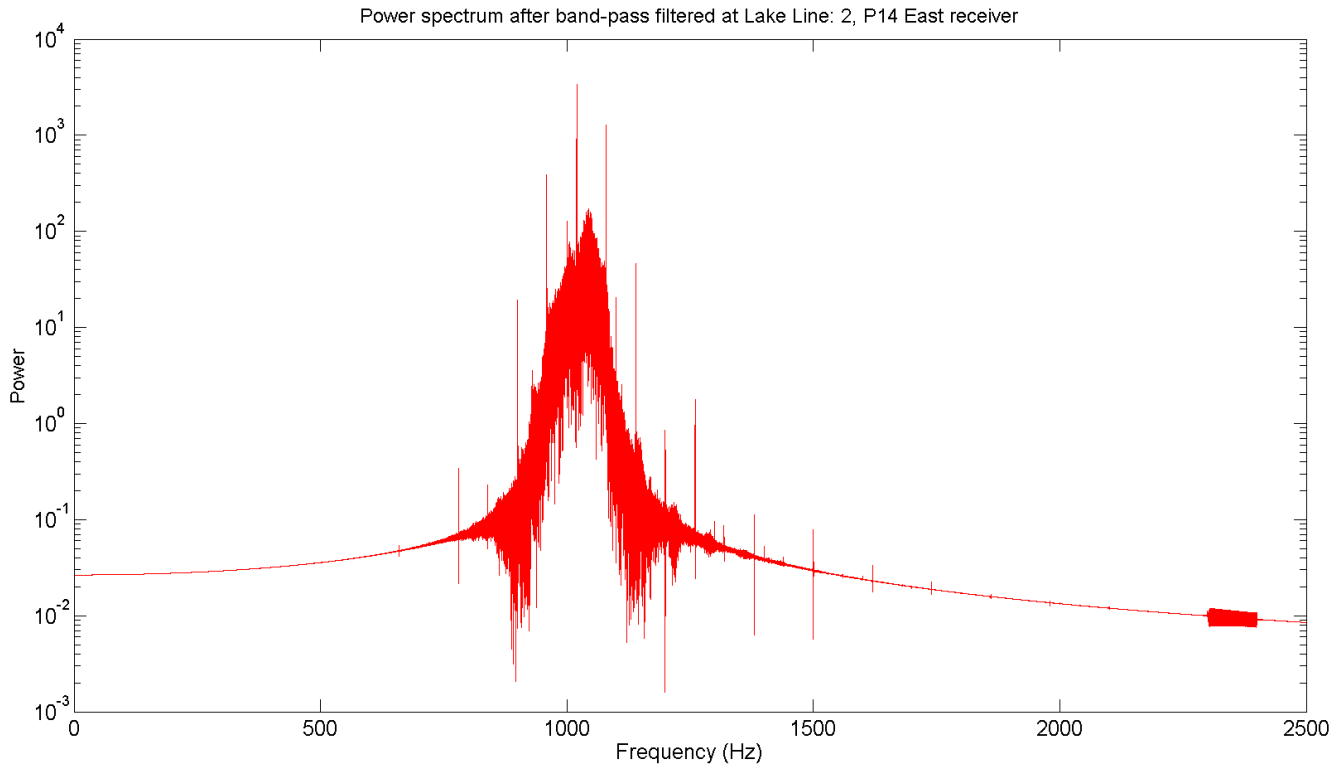

Figure 39: Power spectrum of the full 120 sweep of east coil, lake, line 2, P14 after the band-pass filter has been applied. All frequencies except for the bell-shaped region (970-1060 Hz) have been suppressed.

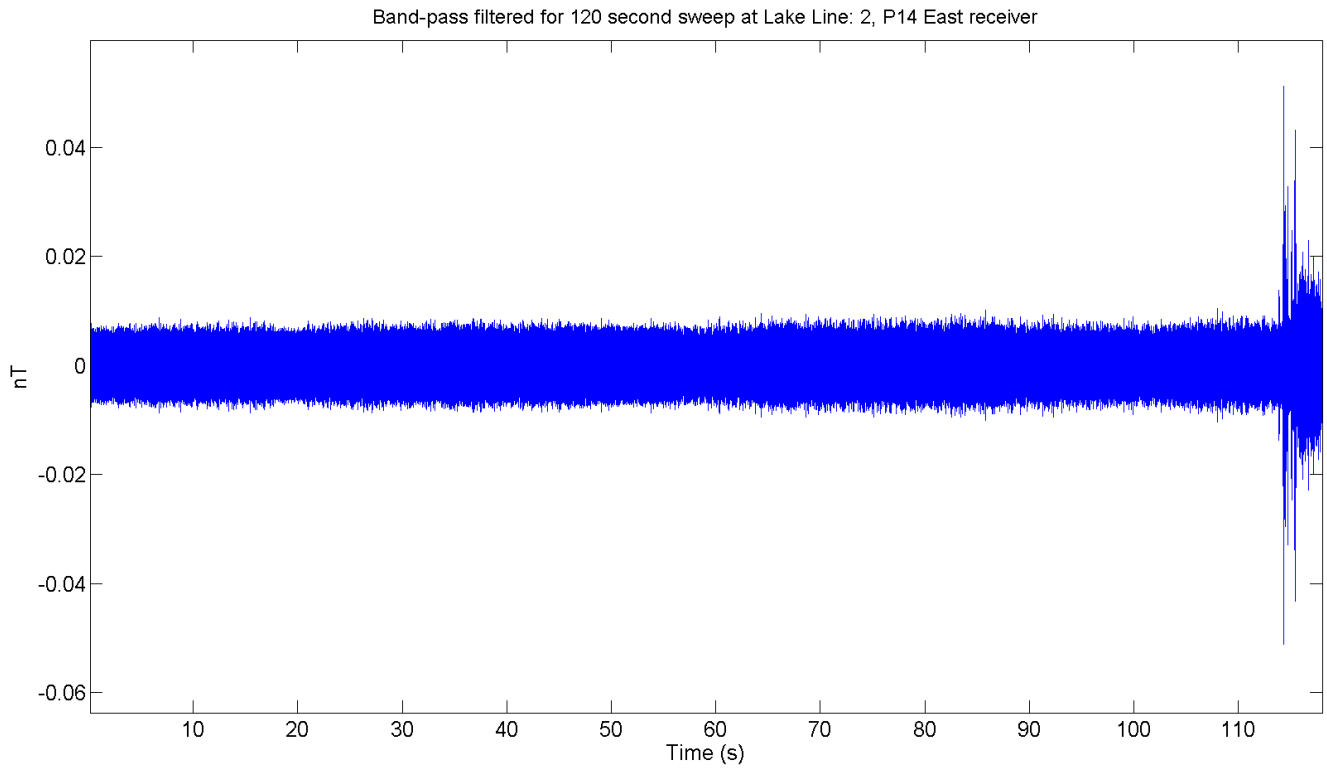

Figure 40: A 118-second window (full sweep) of the signal after the band-pass filter for full sweep of east coil, lake, line 2, P14. The amplitude of the signal is fairly constant, except for the last few seconds, where it becomes more erratic because the frequency is changing from 2400 Hz to 2300 Hz, before the sweep ends at 2302 Hz (see Table 6).

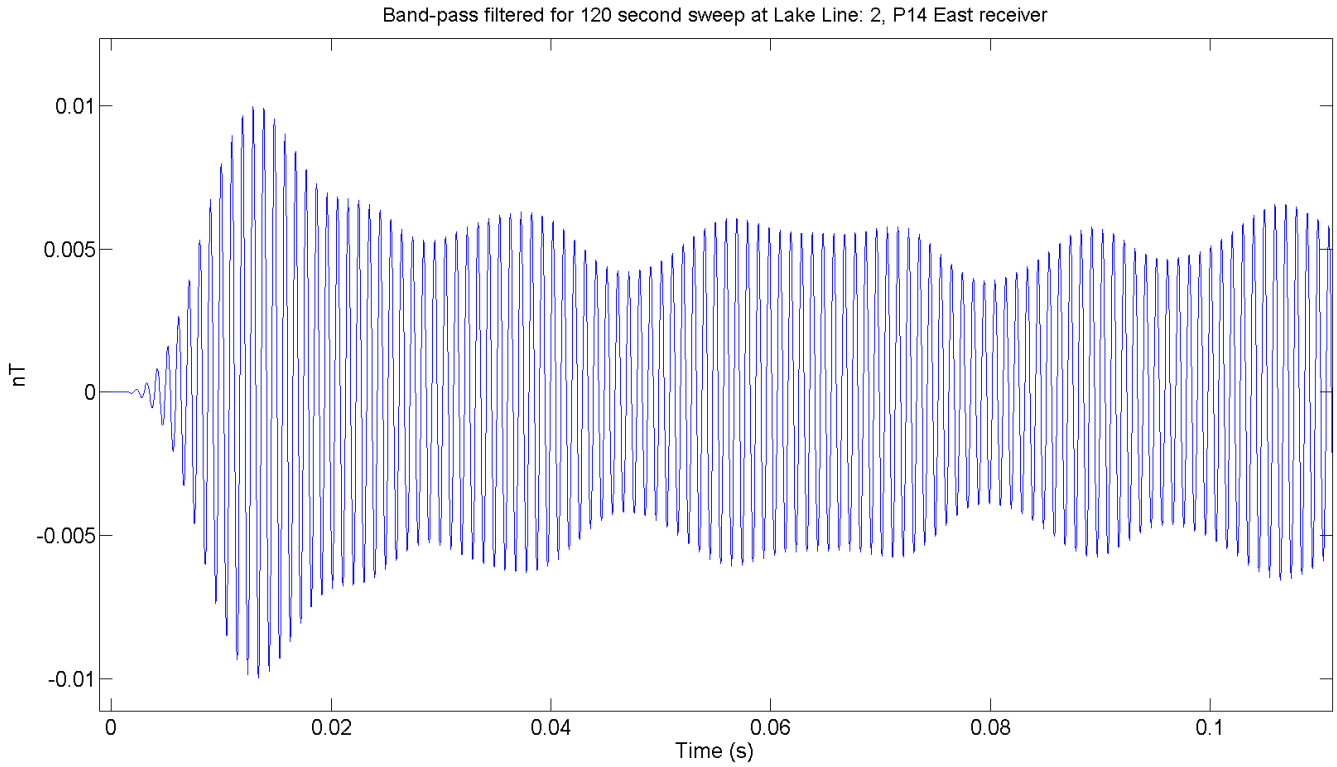

Figure 41: A 0.1-second segment of the band-pass filtered signal for the full sweep of east coil, lake, line 2, P14. The band-pass filtered signal seems to be an amplitude modulated 1045 Hz wave, throughout the entire sweep.

Table 3: The peak frequencies within the bell-shaped features of the power spectrum for both the east and north receivers of the lake survey. Values were taken from power spectrums that gave the obvious bell-shaped feature; not all power spectrums had the bell-shaped feature.

Line	Receiver Position	**East**-coil	**North**-coil
		Frequency peak (Hz)	Frequency peak (Hz)
2	10	1031	1037
	11	1036	1033
	12	1041	1041
	14	1045	1039
	15	1046	1041
	16	1050	1048
	17	1047	1042

5.3 Off-time results

Since the signal generator was manually operated, transmitter termination (TT) occurred when the operator physically turned off the device off. The signal generator would automatically cycle from 2400 Hz back to 2300 Hz at the end of the sweep, meaning that being slightly early in stopping the 120-second transmit time would result in the final frequency being less than 2400 Hz and being slightly late would result in a final frequency being greater than 2300 Hz. Hence this resulted in most of the final transmitting frequencies not equal to 2400 Hz; even though that is when the sweep was supposed to end. The final transmitted frequencies from the signal generator at each receiver position are summarized in Table 6 in Appendix A.

The motivation for completing an off-time analysis came from observing the raw data within a 2-second period following TT. In the raw data, there was an oscillatory decay immediately after TT which did not appear in the CM data, shown previously in Figure 28. The land survey had no oscillatory nature after TT. For example, a comparison between the lake and land survey just after TT is displayed in Figures 42 and 43, for line 2, receiver box position 12, and the east coil receiver. Both figures show 10 milliseconds before TT and 75 milliseconds after TT. The land surveys had no oscillatory decays whereas the lake survey had a prominent exponential oscillatory decay particularly for the receiver positions near the loop (receiver positions 7-15).

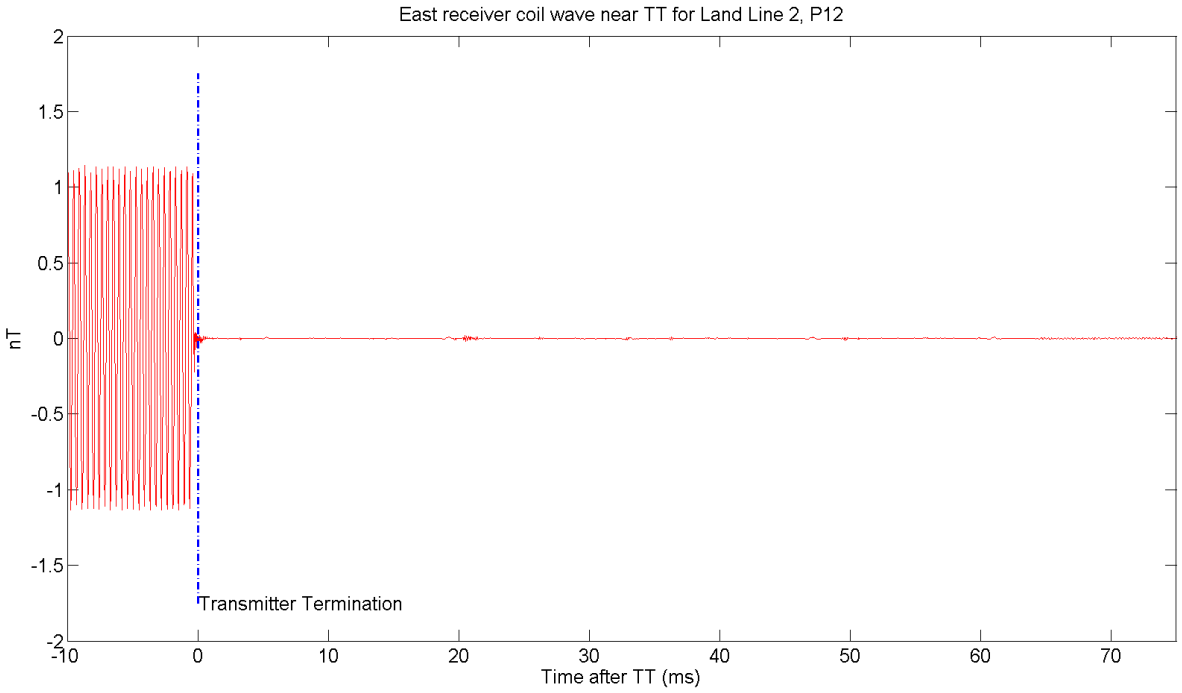

Figure 42: East coil receiver for land, line 2, position 12 immediately near TT, which occurs at t=0. The time range is from 10 milliseconds before TT to 75 milliseconds after TT. The large amplitude wave before TT is the primary field generated by the transmitter. There is no oscillatory decay after TT.

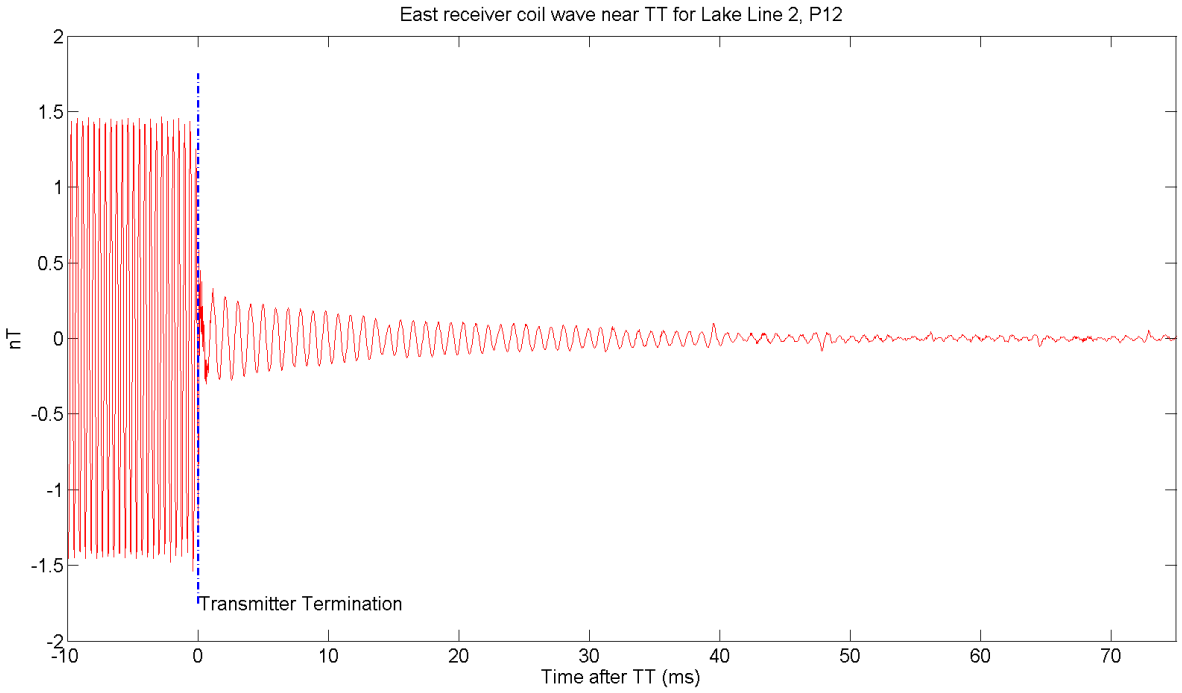

Figure 43: Decay in east coil receiver for lake, line 2, position 12 immediately after TT, which occurs at t=0. The time range is from 10 milliseconds before TT to 75 milliseconds after TT. The large amplitude prior to TT is the recorded signal while transmitting and the oscillatory decay is once the transmitting loop has been shut off.

5.3.1 Decay amplitude

A comparison between the amplitude in the receiver coil prior to TT and immediately after TT were compared. The two amplitudes being compared are shown in Figure 44. The decay is only discernible in receiver waveforms collected at positions 7-15 (recall Figure 18). The land data showed no oscillatory decay after TT; the decay is exclusive to the lake survey.

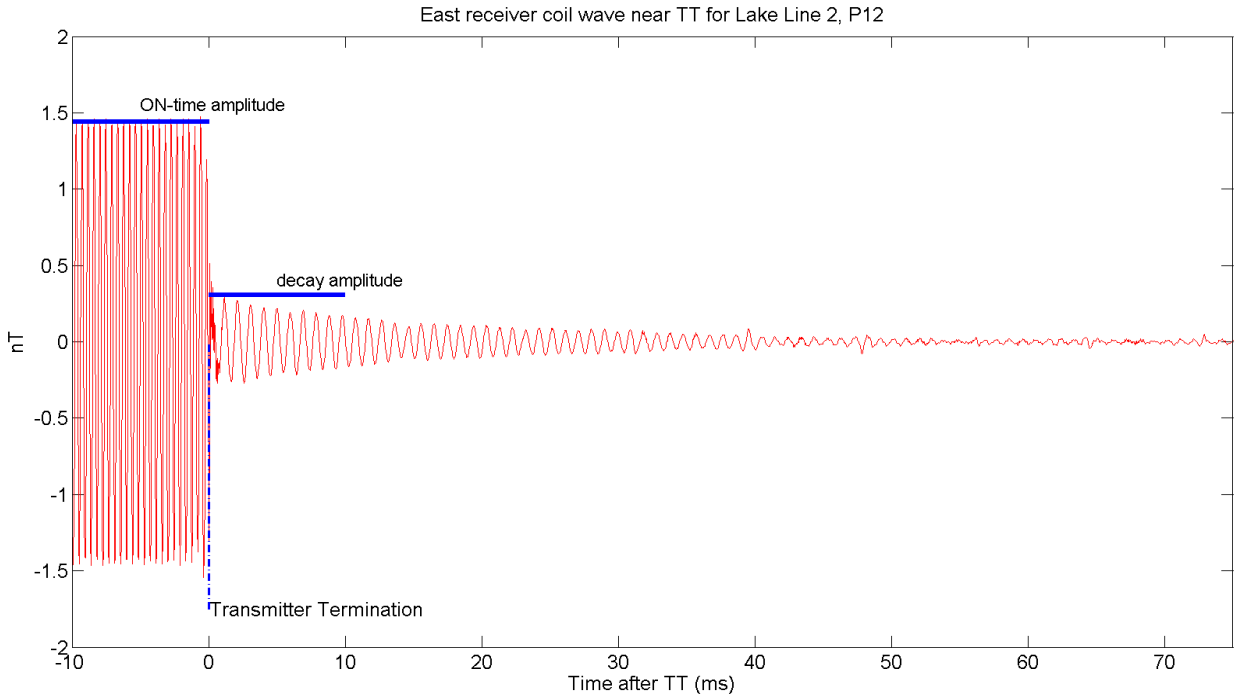

Figure 44: A detail of Figure 43 with amplitudes of the on-time wave and off-time decay near TT, which occurs at t=0. A comparison between the two amplitudes will be addressed.

The on-time and off-time decay amplitudes are summarized in Table 4, with the maximum and minimum values being coloured. A visual comparison of the off-time decays are illustrated in Figures 45-48. The decay plots show receiver positions 7-15 for both lines and for both the east and north coil in the lake survey. The time length of the decays shown is only **50 milliseconds**, which allows for easy comparison of the peak amplitudes between receiver positions.

Table 4: Absolute amplitude values for on-time and off-time decay segments of the waveforms, with their associated ratio. The **maximum** and **minimum** values for each column are coloured.

Line	Receiver Position	**East**-coil (nT)			**North**-coil (nT)		
		ON-time amp. (ρ)	Decay amp. (δ)	δ/ρ	On-time amp. (ρ)	Decay amp. (δ)	δ/ρ
1	7	0.145	0.0564	0.389	0.228	0.0423	0.186
	8	0.392	0.0734	0.187	0.118	0.0663	0.563
	9	0.266	0.0903	0.339	0.359	0.0919	0.256
	10	0.527	0.161	0.305	0.752	0.138	0.183
	11	0.718	0.0951	0.132	0.876	0.0844	0.0963
	12	1.99	0.166	0.0832	0.749	0.158	0.211
	13	1.65	0.156	0.095	1.07	0.117	0.109
	14	0.166	0.0541	0.325	1.01	0.0926	0.092
	15	0.12	0.0564	0.47	0.167	0.0455	0.273
2	7	0.2	0.0479	0.239	0.452	0.0665	0.147
	10	0.829	0.196	0.236	2.78	0.152	0.0545
	11	1.27	0.167	0.132	1.49	0.132	0.0885
	12	1.44	0.291	0.202	4.05	0.225	0.0555
	14	0.259	0.0603	0.233	1.16	0.0661	0.0569
	15	0.116	0.0346	0.298	0.582	0.0482	0.0829

Figures 45-46 show the decays in line 1 (north-south) of the lake survey. Figure 45 shows the east coil off-time decays and Figure 46 shows the north coil off-time decays. The peak decay amplitude occurs at position 12 for both the east coil (0.166 nT) and north coil (0.158 nT). Position 12 corresponds to the receiver box being on the inside of the loop (4 metres from the actual loop).

Similarly, Figures 47-48 show the decays for the east and north coils, respectively, for line 2 (east-west) of the lake survey. At receiver positions 8, 9, and 13, no data were collected due to signal generator operator negligence. The peak amplitudes were measured at receiver position 12, similar to line 1. The east coil decay peak amplitude was 0.291 nT and the north coil decay peak amplitude was 0.225 nT. All off-time peak decay amplitudes are summarized in Table 4.

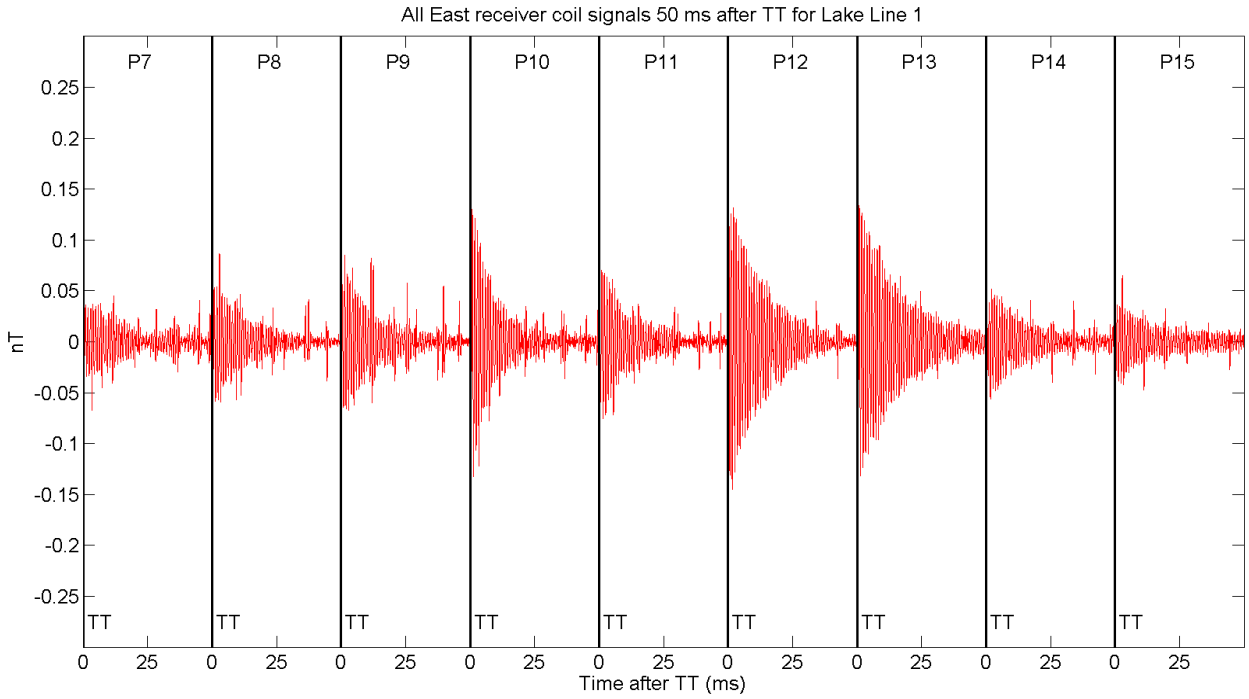

Figure 45: Off-time decays (50 ms) in east receiver coil after TT for lake, line 1, positions 7-15

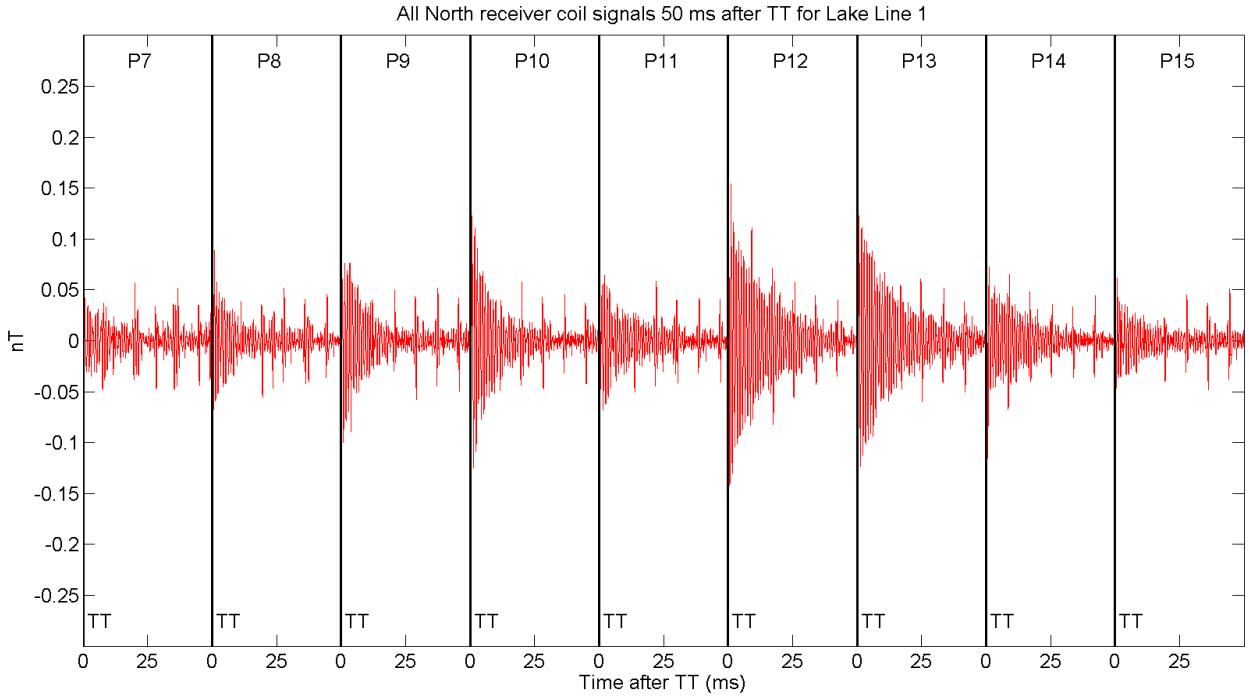

Figure 46: Off-time decays (50 ms) in north receiver coil after TT for lake, line 1, lositions 7-15

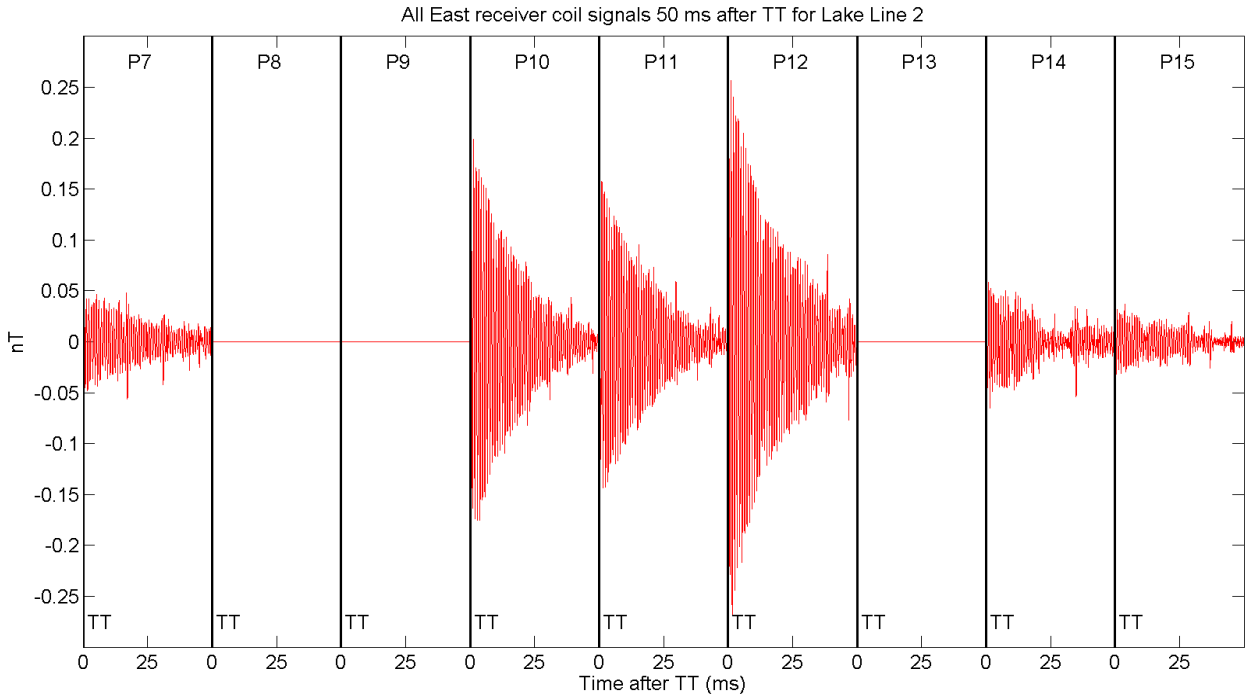

Figure 47: Off-time decays (50 ms) in east receiver coil after TT for lake, line 2, positions 7-15

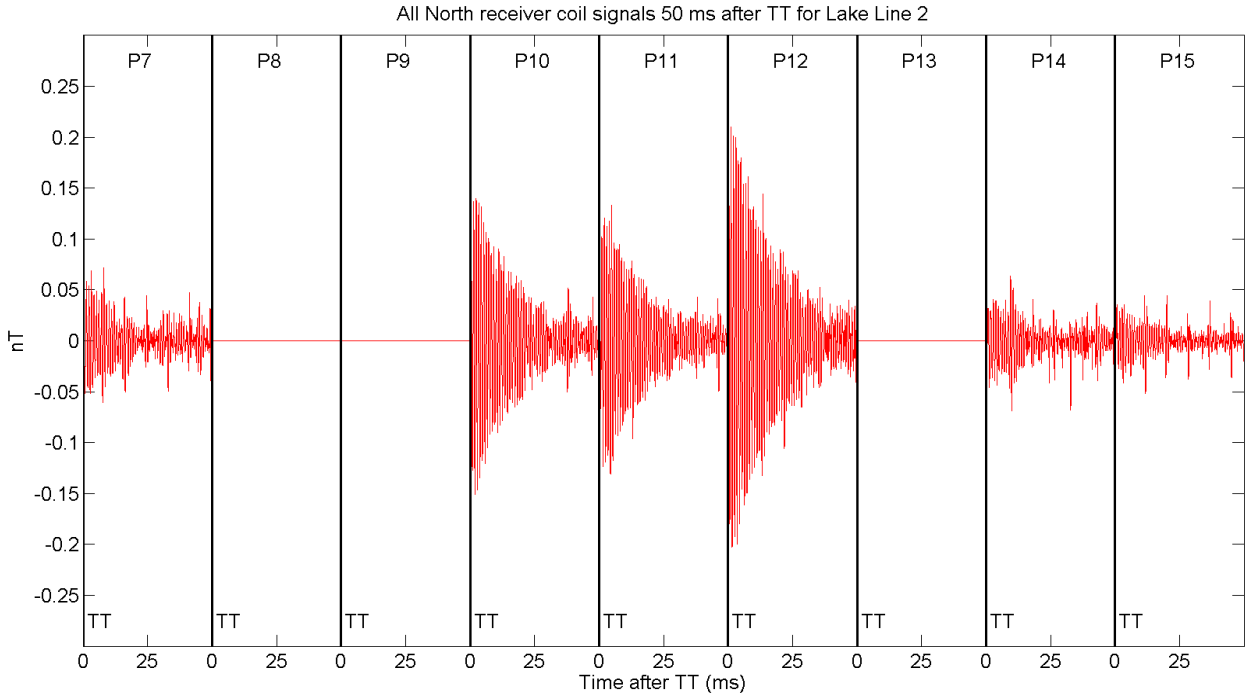

Figure 48: Off-time decays (50 ms) in north receiver coil after TT for lake, line 2, positions 7-15

5.3.2 Fourier transform analysis

The power spectrum was taken of the decays shown in Figures 45-48 for both the east coil and north coil. An example of the power spectrum (PS), calculated for position 12 of line 2 from the lake survey, is shown in Figure 49. The power spectrum was calculated by first taking the fast Fourier transform (FFT) of the decay portion and then taking the magnitude of the real and imaginary components as a function of frequency (i.e., PS $= \sqrt{\Re(\texttt{FFT})^2 + \Im(\texttt{FFT})^2}$). The frequency component of the decays along with the final transmitted frequencies are shown in Table 5.

The decay portion used for the PS calculation was from TT to 75 milliseconds after TT, a time where the decay had significantly diminished. Although, for the actual PS calculation, a 1-second long time series was used to increase resolution in the PS.

First, the 1-second long time series was initialized to be 31250 zeros and then the 2343 samples (0.075 s $\times$ 31250 samples/s) from the decay were input into the real part of the 31250-point time series (i.e., the 1 second long time series contained the actual decay in samples 1-2343 and samples above 2343 were all zeros). In the power spectrum, the resolution was calculated using the equation, $f_{analysis}(m) = \frac{mf_s}{N}$ where m is the sample point, f_s is the sampling frequency, and N is the number of samples in the times series (Lyons, 2004). By using the 1-second long time series ($f_s = N = 31250$), the resolution in the calculated PS is 1 Hz. However, since there are only 2343 points, the true resolution is $f_{analysis}(1) = \frac{31250}{2343} \simeq 13$ Hz and the intermediate points are interpolated between sample points. The error in the peak frequency calculation is then half this resolution, 6.5 Hz.

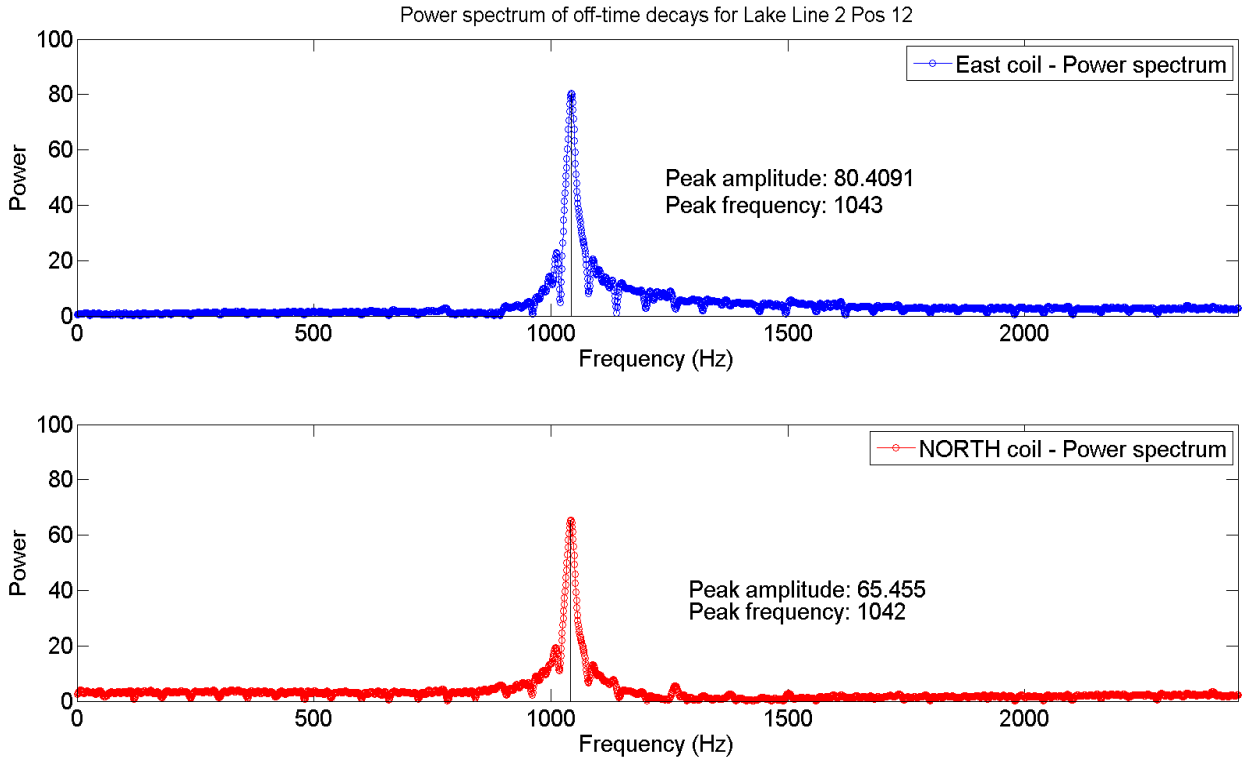

Figure 49: Peak frequency and power for off-time decay (40 ms) of the east and north coils for lake, line 2, position 12

The decay immediately after transmitter termination (TT) has a frequency range of 980-1045 Hz (Table 5). The relationship between the decay frequency and the final transmitted frequency, shown in Figure 50, does not seem to have any obvious correlation. The decay frequency versus profile position in Figure 51 shows a general linear trend as the receiver position increases, for both lines.

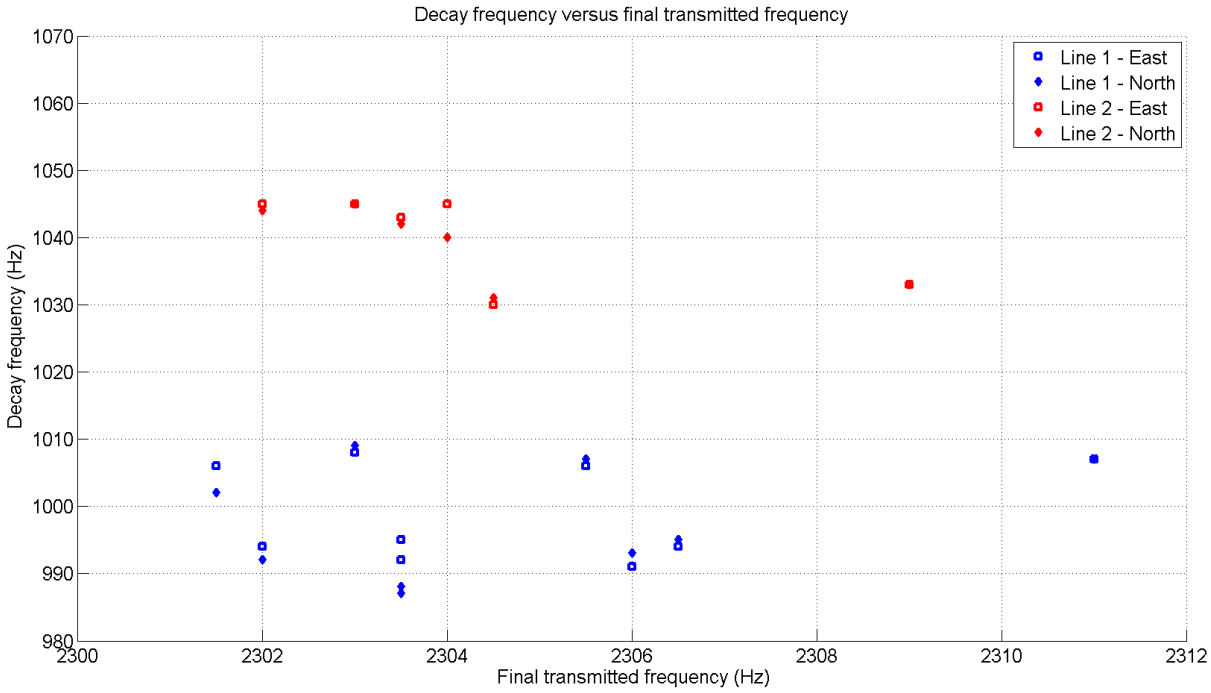

Figure 50: Comparison between decay frequency and final transmitted frequency.

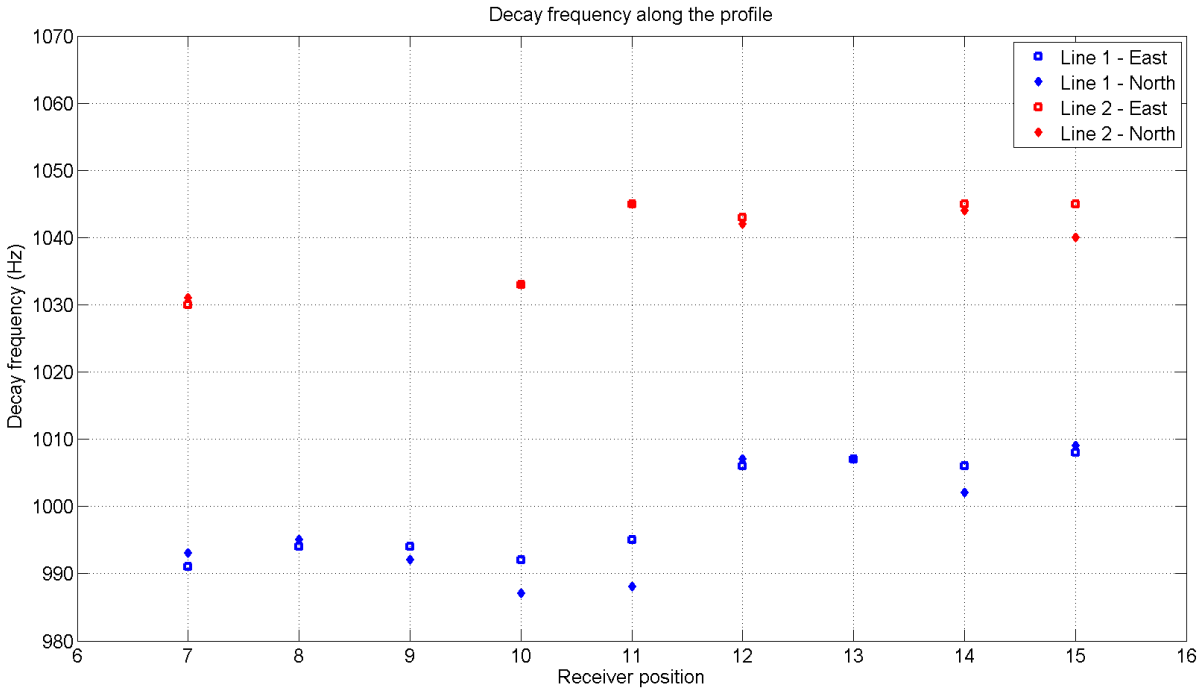

Figure 51: The frequency component of the decay in the east and the north sensor for receiver positions 7-15.

Table 5: The comparison between final transmitted frequencies to the peak frequency and power in the off-time decays of the lake survey.

Line	Receiver Position	Final Transmitted frequency (Hz)	**East**-coil off-time decay		**North**-coil off-time decay	
			Peak frequency (Hz) ± 6.5	Power at Peak frequency (W)	Peak frequency (Hz) ± 6.5	Power at Peak frequency (W)
1	7	2306	991	8.2842	993	7.2026
	8	2306.5	994	13.604	995	11.446
	9	2302	994	19.913	992	14.447
	10	2303.5	992	23.073	987	19.816
	11	2303.5	995	14.548	988	12.378
	12	2305.5	1006	30.285	1007	32.235
	13	2311	1007	36.217	1007	31.453
	14	2301.5	1006	13.029	1002	15.475
	15	2303	1008	12.758	1009	11.27
2	7	2304.5	1030	16.089	1031	14.012
	10	2309	1033	58.533	1033	45.856
	11	2303	1045	48.328	1045	36.533
	12	2303.5	1043	80.409	1042	65.455
	14	2302	1045	19.072	1044	12.891
	15	2304	1045	10.91	1040	7.8406

Chapter 6

6 Discussion

6.1 On-time

The frequency sweep attempted to activate the protons in the water molecules at the Larmor frequency to produce an NMR field that would then manifest itself as a phase shift in the receiver coils. The first method applied to the on-time analysis was the heterodyne method, which calculates the phase difference between two sinusoidal functions. After many attempts to remove sources of noise from the data and find a distinct phase shift at the Larmor frequency, as shown in Figures 36 and 37, the heterodyne method did not provide convincing evidence that a secondary magnetic field created by an oscillation at the Larmor frequency

impacted the phase between the transmitted signal and the received signal during the sweep.

After modeling the magnetization vector, subjected to the field produced during the sweep, using Equations 37-39, it becomes clear as to why the heterodyne method did not detect a phase shift. A diagram showing the magnetization at significant times during the frequency sweep are outlined in Figure 52, using $\mathbf{B_0}$ = 55135 nT as the Earth's field, $\mathbf{B_1}$ = 520 nT for the applied field produced by our transmitting loop, and T_2=2100 ms as the decay constant for unbound freshwater.

The magnetization vector is initially aligned with the Earth's field (Figure 52a). Once the transmitting field at 2300 Hz is applied, an effective field is produced and the magnetization vector begins to rotate around it (Figure 52b). Since the frequency sweep is long ($t_{sweep} >> T_2$), the magnetization vector decays to $\mathbf{B}_{\text{eff}}$ (Figure 52c) and follows $\mathbf{B}_{\text{eff}}$ until the end of the sweep (Figure 52d). Once the transmitted field is terminated (t=TT), the magnetization vector begins its decay towards the ambient field (Figure 52e), until after a few seconds, it is aligned with the ambient field (Figure 52f).

During the early-time and late-time (near TT) portion of the sweep, the magnetization vector, while precessing around the effective field, undergoes complex dynamics. The complex dynamics were attempted to be found using the Fourier transform techniques posed earlier, albeit not successful. The reason the heterodyne method did not produce any conclusive evidence is because when the sweep hits the Larmor frequency, the magnetization vector is already aligned with $\mathbf{B}_{\text{eff}}$ and will not produce an NMR field, as originally hypothesized.

An interesting result from the FT methods, was the peculiar bell-shaped feature around 1000 Hz in the power spectrums for the full sweep. The frequency peaks within the bell-

shaped feature are between 980-1050 Hz and reasonably coincide with the decay frequencies shown in Section 5.3. It seems entirely possible that the oscillation is existent throughout the entire sweep and simply decays once the energising field has been terminated. However, at the time of writing, no physical explanation for the near 1000 Hz feature could be found.

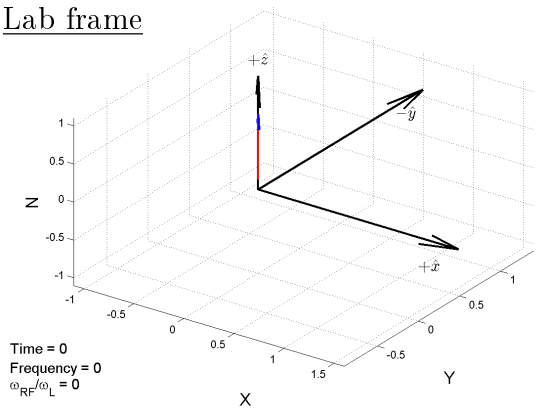

(a) Before excitation, **M** is aligned with the Earth's field (aligned with $\hat{z}$), which is also $\mathbf{B}_{\text{eff}}$.

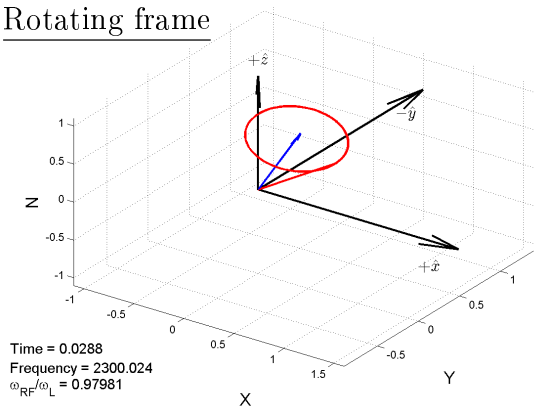

(b) In the rotating frame. When the off-resonance field is applied (in the $\hat{x}$-direction), $\mathbf{B}_{\text{eff}}$ is a combination of $\mathbf{B_1}$ and $\mathbf{B_0}$. **M** precesses around $\mathbf{B}_{\text{eff}}$.

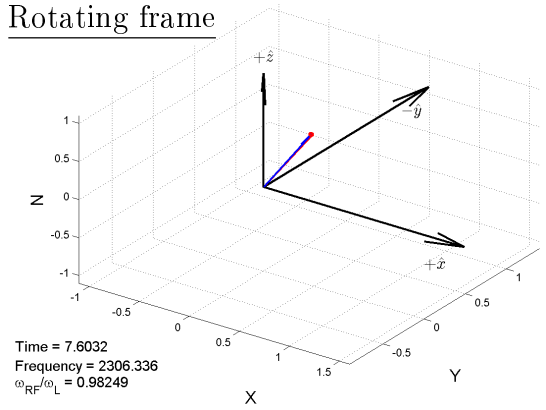

(c) Due to the long duration of the sweep, **M** becomes aligned with $\mathbf{B}_{\text{eff}}$, after a short while.

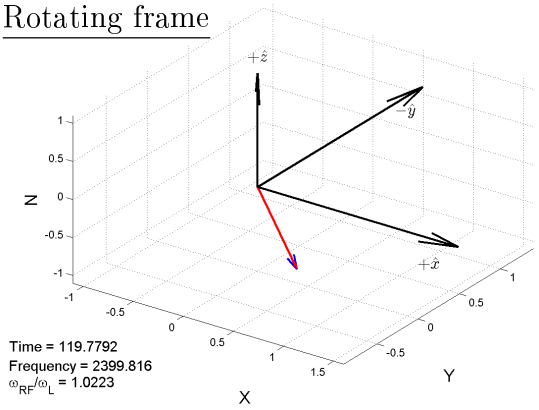

(d) **M** remains aligned with $\mathbf{B}_{\text{eff}}$ through the majority of the sweep.

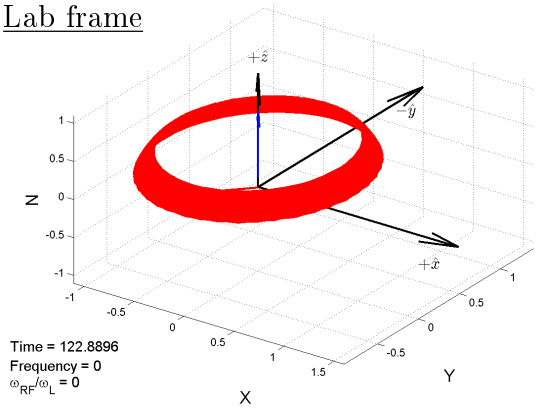

(e) Once the applied field has been terminated, $\mathbf{B}_{\text{eff}} = \mathbf{B_0}$ and **M** precesses towards relaxation, $\hat{z}$, around $\mathbf{B}_0$.

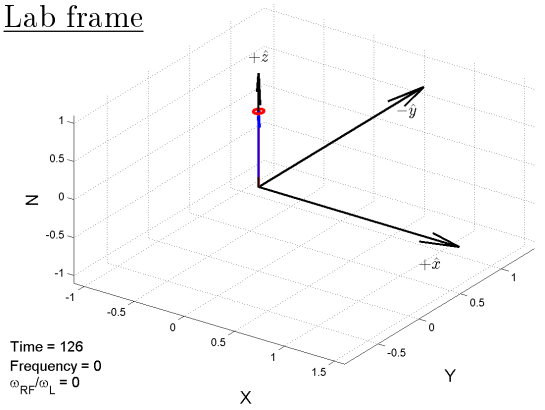

(f) **M** has fully relaxed, now aligned with $\mathbf{B}_{\text{eff}}$.

Figure 52: The dynamics of the magnetization vector during the frequency sweep employed during the lake & land surveys. The red line represents the path taken by the magnetization vector. Each figure displays whether the process is in the lab frame or rotating frame, the time of the simulation, the transmitted frequency at given time, and the ratio between transmitted frequency and Larmor frequency.

6.2 Off-time

The off-time analysis consisted of filtering the received signals, and looking at them immediately after the transmitted field was terminated (TT). The decays have an NMR relaxation shape, but the frequency is not equal to the Larmor frequency (estimated using FT methods). The oscillation is most prominent in the first 50 ms after TT, but in some cases it can be seen past 75 ms, although quite faint (Figure 44). The decay immediately after TT has a frequency range of 980-1045 Hz (Figures 50-51 and Table 5), which is not near the Larmor frequency of our survey, 2348 Hz. In order to get the Larmor frequency shown in the decays, the Earth's field would have to be just over halved, 23485 nT ($f_L = 0.04258 * 23485$), to create the shown decay frequency. Since the frequency component of the decays are not equal to the Larmor frequency (about 40%), they cannot be attributed to an NMR signal.

The decays shown in Figures 45-48 are exclusive to the lake survey and strongest at positions near the loop (P7-P15). The largest decay signal amplitude occurred at P12 for both lines and both coil directions; similar to the original hypothesis shown in Figures 24-25. Although not an NMR signal, it is a property of the lake survey and requires further investigation. By performing the exact same survey with respect to loop layout, input current, frequency sweep, equipment, and receiver positions, over an ice-covered lake and over dry land, we can assume that the field produced from the loop is the same in both survey areas and direct comparison between data sets is valid. The only difference between the survey areas, excluding subsurface composition (snow, ice, and water compared to rock), was the temperature, -20°C for the lake survey and +15°C for the land survey.

If the oscillatory decay measured is not from the NMR decay of the water molecules, then it could be another phenomenon of the water or possibly some residual response from the electronics (including sensors). The ANT-23 sensors have a residual ringing that occurs around 14-15 kHz, which is well above our frequency sweep and Larmor frequency. This

high frequency ringing is visible about 1 ms after TT (not shown), but does not affect the decay. Further testing was done by the makers of the ANT-23 sensors, Zonge International, and they were unable to produce the oscillatory decay that is prevalent in our lake survey. The other two possibilities would be residual discharging, or something similar, in the signal generator or the amplifier. However, the decay was not present in the CM data, so it was not transmitted as part of the of the primary field. At the time of writing, these two devices have not been tested for direct radiation of such a signal. If the off-time decay was caused by the sensors or another electronic device, then it would be apparent in the land survey, which it is not. Also, the frequency of the decay would be the same at each position, not the gradual change that is seen in the lake survey.

The relationship between the decay frequency and profile position shown in Figure 51, has a positive linear trend for each of the profile lines. The survey was conducted by starting at P1 of line 1 and then proceeding to P21, followed by a data dump on a computer, and then P1-P21 of line 2. Position 11 of both profile lines, has the same receiver box orientation, their only difference being the time the data were recorded. The difference in time between the two recordings (P11 of line 1 and P11 of line 2) was about 60 minutes. Since they both represent the same position in space, with respect to our grid, then theoretically they should have a very similar response and decay frequency. Both responses have the decay, but have different amplitudes. The primary, and most significant, difference is the frequency of the decays. In line 1, the decay frequency is between 988-995 Hz whereas in line 2, the decay is 1045 Hz, a difference of 50 Hz at the same position. The two decays would be the same assuming it was an electronics effect. It seems that there is a time-dependent variation in the decay frequency, which could be linked to diurnal variations in the geomagnetic field or the ambient temperature.

The modeling shows that when the sweep is finished and the transmitting field has been

terminated, the magnetization vector is at an angle greater than 90 degrees from the ambient field (Figure 52d). After TT, the magnetization vector relaxes back to equilibrium at the Larmor frequency, not a frequency near 1000 Hz that we see.

Chapter 7

7 Conclusions

The methods proposed to look for a phase shift or any signal at the Larmor frequency work in theory, but in this experiment we were unable to provide conclusive evidence of an NMR signal. The modeling of the magnetization vector suggested that the frequency sweep was so slow that there was not a distinct phase shift at the Larmor frequency. Although, the near 1000 Hz signal that shows in the power spectrums of the on-time sweeps and in the off-time decays are unexplained. More experimental data and or modeling of the system is needed to help describe this phenomenon. If this project were to move forward, then below are several personal recommendations that I would suggest.

Firstly, more testing of the electronics is needed, especially at various temperatures. The only differences in the survey areas were the temperatures and the subsurface compositions. If the electronics could be categorically ruled out (i.e., no temperature-dependent responses) then the only reason for the decay would have to be some interaction between the transmitted sweep and the frozen lake (ice or water).

Assuming that the electronics were to be ruled out, a different transmitting field should be implemented. The survey should have begun with basic ~20 ms pulses at the Larmor frequency to see if our system (transmitter and receiver) is even able to initiate an excitation and then record the relaxation. Perhaps the sensitivity of the sensors was too low and

our NMR signal was below the noise level. Although unlikely, since in most NMR surveys conducted today, they are able to record NMR responses in the low 100 nanovolts, which is definitely above the ANT-23 sensitivity levels. For instance, in Bernard and Legchenko (2003), an MRS survey conducted in India recorded an initial NMR amplitude signal of 35 nanovolts with a 75 metre by 75 metre loop, producing an effective signal level of ~6 pV/m^2. Generally, the NMR initial amplitude signals range from tens to a few hundred nanovolts with single-turn loops ranging from 50 metres to 150 metres in diameter (Bernard and Legchenko, 2003).

Depending on the duration of the experiment, having a base station magnetometer to measure diurnal changes in the geomagnetic field would be useful in explaining the changes in frequency of the signal close to 1000 Hz. Measurement of the signal produced by the gas-powered generator would allow for a more accurate representation of the 60 Hz signal which corrupted many of the data. If the 60 Hz signal could be measured, or even mitigated by increasing the distance between the generator and receiver positions, then the filtering methods would be minimized which would allow for a more accurate representation of the phase difference.

If the system was able to record an NMR decay, then it would be acceptable to implement off-resonance pulses. The success of the off-resonance pulses is crucial for a possible airborne system as the airborne system would always be transmitting slightly off-resonance due to it flying quickly over locations where the Earth's field is different, and the requirement that the NMR excitation frequency be different from the odd harmonics of the airborne electromagnetic system. If the off-resonance pulses were successful, then it would be advisable to begin increasing the distance between the sensors and transmitting loop. It would then be possible to find an empirical relationship between the strength of the primary field, degree of off-resonance, and decay amplitude.

More modeling of the systems would be required to see what the NMR field would look like under certain pulses or sweeps. The minimal modeling displayed in this thesis was due to the assumption that we knew there was a large volume of freshwater and that it could be activated by a radio-frequency field at the Larmor frequency. It did not seem necessary to work on a forward model, since the literature was sufficient. Assuming the off-resonance pulses were successful and they could be accurately modeled numerically, then implementation of an airborne system could then be initiated.

By considering all recommendations mentioned, the possibility of designing an airborne NMR (aNMR) system may become feasible. However, the signal levels in typical sNMR surveys can reach 100 pV/m^2 as shown in Bernard and Legchenko (2003). The largest detrimental factor between the sNMR and would-be aNMR systems is distance between the precessing protons and the receiver loop. The $1/r^3$ reduction in the magnetic field produced by the precessing protons may be too large to record an NMR signal in existing airborne systems.

References

Abragam, A. (1983). *Principles of Nuclear Magnetism.* Oxford University Press.

Anton, H. and Rorres, C. (2005). *Elementary Linear Algebra.* John Wiley & Sons, Inc., 9th edition.

Becker, E. D. (2000). *High Resolution NMR Theory and Chemical Applications.* Academic Press, third edition.

Behroozmand, A. A., Auken, E., Fiandaca, G., and Christiansen, A. V. (2012). Improvement

in MRS parameter estimation by joint and laterally constrained inversion of MRS and TEM data. *Geophysics*, 77(4):WB191–WB200.

Behroozmand, A. A., Keating, K., and Esben, A. (2014). A Review of the Principles and Applications of the NMR Technique for Near-Surface Characterization. *Surveys in Geophysics*, 36:27–85.

Bernard, J. (2007). Instruments and field work to measure a Magnetic Resonance Sounding. *Boletín Geológico y Minero*, 118(3):459–472.

Bernard, J. and Legchenko, A. (2003). Groundwater exploration with the magnetic resonance sounding method. *ASEG 16th Geophysical Conference and Exhibition*.

Bloch, F. (1946). Nuclear induction. *Phys. Rev.*, 70:460–474.

Boyce, W. E. and DiPrima, R. C. (2000). *Elementary Differential Equations and Boundary Value Problems*. John Wiley & Sons, Inc., 7th edition.

Bronson, R. and Costa, G. (2006). *Schaum's Outline of Differential Equations*. Schaum's Outline Series. McGraw-Hill, 3rd edition.

Brown, R. and Gamson, B. (1960). Nuclear magnetism logging. *Society of Petroleum Engineers*.

Costabel, S., Guenther, T., Dlugosch, R., and Mueller-Petke, M. (2016). Torus-nuclear magnetic resonance: Quasi-continuous airborne magnetic resonance profiling by using a helium-filled balloon. *Geophysics*, 81(4):WB119–WB129.

Davis, A. C., Dlugosch, R., Queitsch, M., Macnae, J. C., Stolz, R., and Mueller-Petke, M. (2014). First evidence of detecting surface nuclear magnetic resonance signals using a compact B-field sensor. *Geophysical Research Letters*, 41(12):4222–4229.

Farrar, T. C. and Becker, E. D. (1971). *Pulse and Fourier Transform NMR: Introduction to Theory and Methods*. Academic Press.

Feynman, R., Leighton, R., and Sands, M. (1963). *Mainly Electromagnetism and Matter*, volume 2 of *The Feynman Lectures on Physics*. Addison-Wesley.

Freeze, R. A. and Cherry, J. A. (1979). *Groundwater*. Prentice Hall, Inc., Upper Saddle River, NJ 07458.

Gerlach, W. and Stern, O. (1922). Der experimentelle Nachweis der Richtungsquantelung im Magnetfeld. *Zeitschrift fur Physik*, 9:349–352.

Goldman, M. and Neubauer, F. (1994). Groundwater exploration using integrated geophysical techniques. *Surveys in Geophysics*, 15:331–361.

Grant, F. and West, G. (1965). *Interpretation theory in applied geophysics*. International series in the earth sciences. McGraw-Hill.

Griffiths, D. J. (2005). *Introduction to Quantum Mechanics*. Pearson Prentice Hall, Upper Saddle River, NJ 07458, 2nd edition.

Griffiths, D. J. (2013). *Introduction to Electrodynamics*. Pearson, 4th edition.

Grombacher, D. and Knight, R. (2015). The impact of off-resonance effects on water content estimates in surface nuclear magnetic resonance. *Geophysics*, 80(6):E329–E342.

Grunewald, E., Grombacher, D., and Walsh, D. (2016). Adiabatic pulses enhance surface nuclear magnetic resonance measurement and survey speed for groundwater investigations. *Geophysics*, 81(4):WB85–WB96.

Grunewald, E. and Knight, R. (2011). The effect of pore size and magnetic susceptibility on the surface NMR relaxation parameter T_2^*. *Near Surface Geophysics*, 9(2):169–178.

Harris, R. (2008). *Modern Physics*. Pearson Addison-Wesley, 1301 Sansome St., San Francisco, CA 94111, 4th edition.

Hertrich, M. (2008). Imaging of groundwater with nuclear magnetic resonance. *Progress on Nuclear Magnetic Resonance Spectroscopy*, 35:227–248.

Keeler, J. (2005). *Understanding NMR Spectroscopy*. John Wiley & Sons Ltd.

Kirsch, R. (2006). *Groundwater Geophysics A Tool for Hydrogeology*. Springer.

Legchenko, A., Baltassat, J.-M., Beauce, A., and Bernard, J. (2002). Nuclear magnetic resonance as a geophysical tool for hydrogeologists. *Journal of Applied Geophysics*, 50:21–46.

Levitt, M. H. (2008). *Spin Dynamics: Basics of Nuclear Magnetic Resonance*. Wiley.

Lyons, R. G. (2004). *Understanding digital signal processing*. Prentice Hall PTR, 2nd edition.

Müller-Petke, M., Dlugosch, R., and Yaramanci, U. (2011). Evaluation of surface nuclear magnetic resonance-estimated subsurface water content. *New Journal of Physics*, 13(9):095002.

Palacky, G. J. and West, G. F. (1991). Airborne electromagnetic methods. In Nabighian, M. N., editor, *Electromagnetic Methods in Applied Geophysics*, volume 2 of *Investigations in Geophysics*, chapter 10, pages 811–880. Society of Exploration Geophysics.

Parsekian, A. D., Grosse, G., Walbrecker, J. O., Mueller-Petke, M., Keating, K., Liu, L., Jones, B. M., and Knight, R. (2013). Detecting unfrozen sediments below thermokarst lakes with surface nuclear magnetic resonance. *Geophysical Research Letters*, 40(3):535–540.

Phipps, T. E. and Taylor, J. B. (1927). The Magnetic Moment of the Hydrogen Atom. *Physical Review*, 29:309–320.

Shushakov, O. A. (1996). Groundwater nmr in conductive water. *Geophysics*, 61(4):998–1006.

Slichter, C. P. (1990). *Principles of Magnetic Resonance*. Springer-Verlag, third edition.

Smith, R. S., O'Connell, M. D., and Poulsen, L. H. (2004). Using airborne electromagnetics surveys to investigate the hydrogeology of an area near Nyborg, Denmark. *Near Surface Geophysics*, 3:123–130.

Tannus, A. and Garwood, M. (1997). Adiabatic Pulses. *NMR in BIOMEDICINE*, 10:423–434.

Taylor, J. R. (2005). *Classical Mechanics*. University Science Books.

Thébault, E., Finlay, C. C., Beggan, C. D., Alken, P., Aubert, J., Barrois, O., Bertrand, F., Bondar, T., Boness, A., Brocco, L., Canet, E., Chambodut, A., Chulliat, A., Coïsson, P., Civet, F., Du, A., Fournier, A., Fratter, I., Gillet, N., Hamilton, B., Hamoudi, M., Hulot, G., Jager, T., Korte, M., Kuang, W., Lalanne, X., Langlais, B., Léger, J.-M., Lesur, V., Lowes, F. J., Macmillan, S., Mandea, M., Manoj, C., Maus, S., Olsen, N., Petrov, V., Ridley, V., Rother, M., Sabaka, T. J., Saturnino, D., Schachtschneider, R., Sirol, O., Tangborn, A., Thomson, A., Tøffner-Clausen, L., Vigneron, P., Wardinski, I., and Zvereva, T. (2015). International geomagnetic reference field: the 12th generation. *Earth, Planets and Space*, 67(1):79.

Varian, R. H. (1962). *Ground Liquid Prospecting Method and Apparatus*. U.S. Patent 3019383.

Walbrecker, J. O., Hertrich, M., and Green, A. G. (2011). Off-resonance effects in surface nuclear magnetic resonance. *Geophysics*, 76:1–12.

West, G. F. and Macnae, J. C. (1991). Physics of the electromagnetic induction exploration method. In Nabighian, M. N., editor, *Electromagnetic Methods in Applied Geophysics*, volume 2 of *Investigations in Geophysics*, chapter 1, pages 5–46. Society of Exploration Geophysics.

WWAP (United Nations World Water Assessment Programme). (2015). *The United Nations World Water Development Report 2015: Water for a Sustainable World. Paris, UNESCO.*

Yaramanci, U. (2000). Surface Nuclear Magnetic Resonance (SNMR) - A new method for exploration of ground water and aquifer properties. *Annali di Geofisica*, 43(6):1159–1175.

Appendices

A Final transmitted frequencies

Table 6: Final transmitting frequencies for all receiver positions in both surveys

Line	Receiver position	Final transmitted frequency (Hz)	
		Lake	Land
1	1	2308	2352
	2	2394	2301
	3	2306	2301
	4	2301	2300
	5	2303	2301
	6	2302	2301
	7	2305	2300
	8	2307	2301
	9	2301	2399
	10	2303	2301
	11	2304	2300
	12	2305	2302
	13	2310	2300
	14	2302	2300
	15	2301	2301
	16	2301	2303
	17	2301	
	18	2301	
	19	2303	
	20	2304	
	21	2304	
2	1	2310	2315
	2	2400	2302
	3	2302	2301
	4	2301	2302
	5	2400	2302
	6	2304	2302
	7	2303	2400
	8		2300
	9		2301
	10	2309	2301
	11	2303	2400
	12	2304	2302
	13		2301
	14	2301	2301
	15	2303	2301
	16	2304	2301
	17	2399	
	18	2300	
	19	2303	
	20	2302	
	21	2400	

B Sensor noise levels

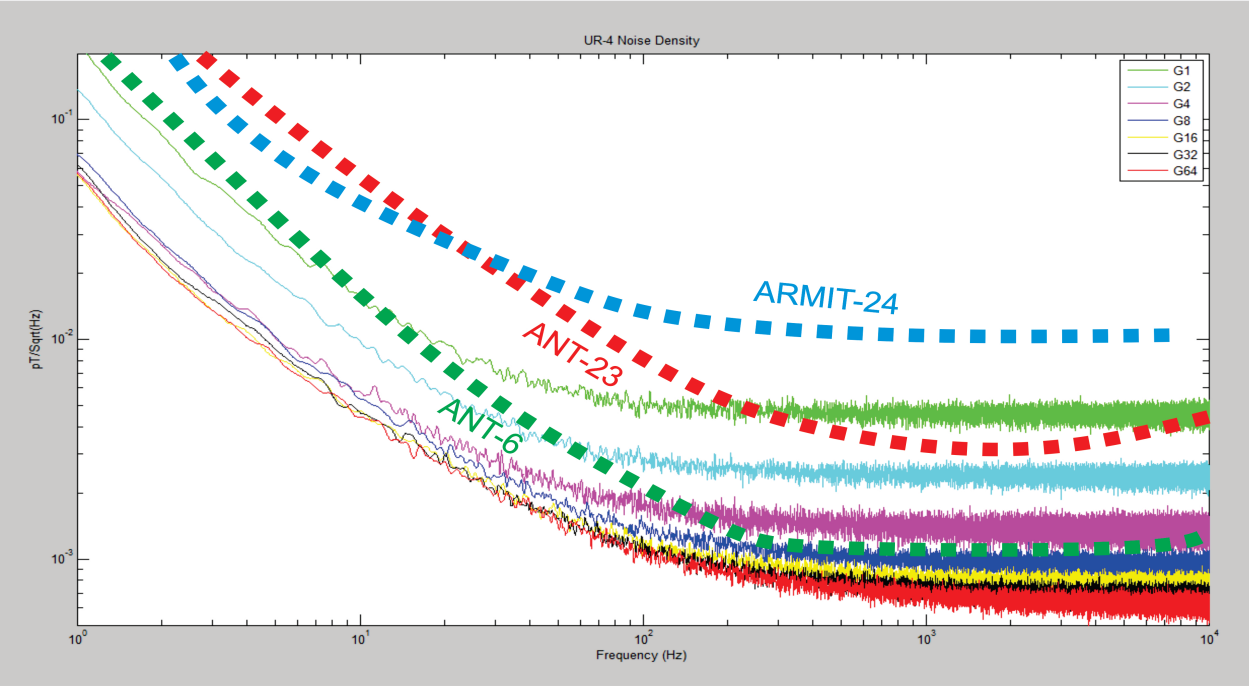

Figure 53: Sensor noise in ANT-23 magnetometer receivers. Image courtesy of Ben Polzer.

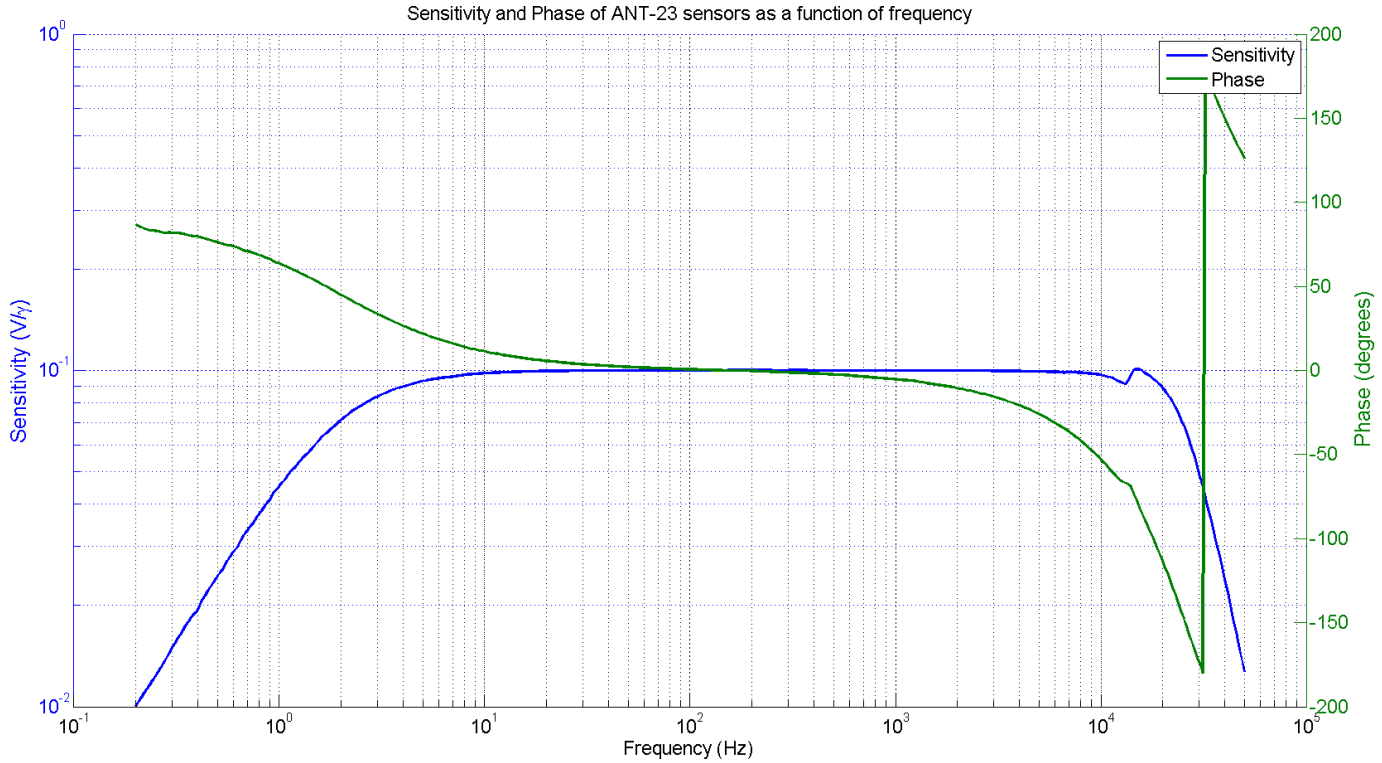

Figure 54: Sensor sensor sensitivities in ANT-23 magnetometer receivers, 1 $\gamma = 1$ nT. Data courtesy of Zonge International.

C Clearwater Lake depth contours

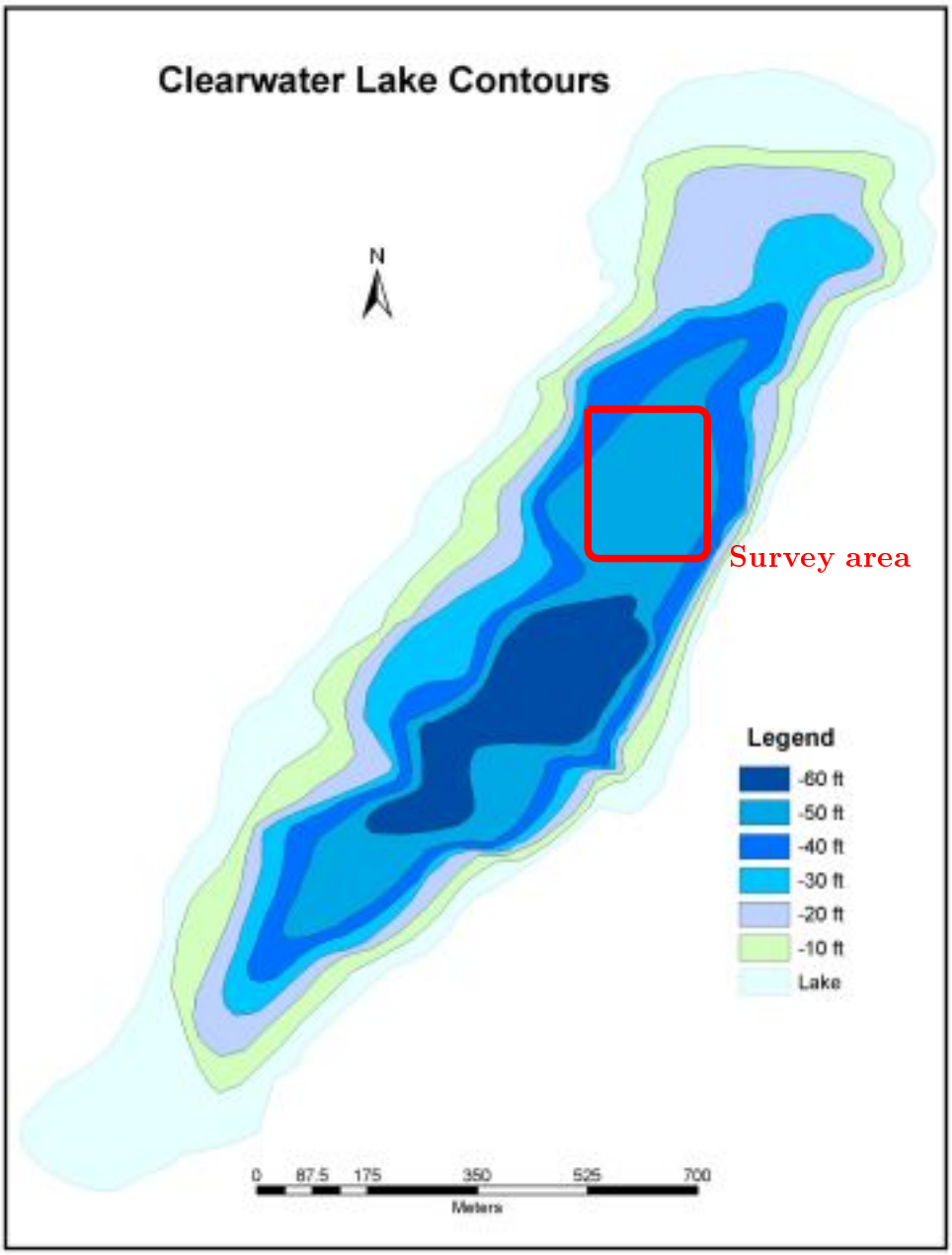

Figure 55: Lake depth contours of Clearwater Lake. The approximate location of the survey is highlighted. Source: http://www.greatersudbury.ca/living/lakes-facts/local-lake-descriptions/clearwater-lake/maps-of-clearwater-lake/